University of New Mexico
UNM Digital Repository

Chemical and Biological Engineering ETDs | Engineering ETDs

6-24-2010

Bioadhesion to model thermally responsive surfaces

Brett Andrzejewski

Follow this and additional works at: https://digitalrepository.unm.edu/cbe_etds

Recommended Citation
Andrzejewski, Brett. "Bioadhesion to model thermally responsive surfaces." (2010). https://digitalrepository.unm.edu/cbe_etds/32

This Dissertation is brought to you for free and open access by the Engineering ETDs at UNM Digital Repository. It has been accepted for inclusion in Chemical and Biological Engineering ETDs by an authorized administrator of UNM Digital Repository. For more information, please contact disc@unm.edu.

Brett Paul Andrzejewski
Candidate

Chemical and Nuclear Engineering
Department

This dissertation is approved, and it is acceptable in quality and form for publication:

Approved by the Dissertation Committee:

, Chairperson

Bioadhesion to Model Thermally Responsive Surfaces

by

Brett Paul Andrzejewski

B.S. Chemical Engineering, University of New Mexico
Albuquerque, New Mexico 2002

DISSERTATION

Submitted in Partial Fulfillment of the
Requirements for the Degree of

Doctor of Philosophy
Chemical Engineering

The University of New Mexico

Albuquerque, New Mexico

November, 2009

©2010, Brett Paul Andrzejewski

Dedication

To all my friends, family, and loved ones who supported me through my degree process. Without your support I never would have finished.
To all the unnamed tax payers, both in the United States and in Germany, whose funding enabled me to do my research. May the knowledge within help you.

Acknowledgments

I would like to thank my adviser, Dr. Gabriel Lopez, for all the support he has given me. Dr. Axel Roshenhahn for his guidance, and friendship, during my internship at the University of Heidelberg. Dr. Michael Grunze for the opportunity to perform research in his laboratories. Dr. Heather Canavan, Dr. Elizabeth Dirk, Linnea Ista, Dr. David Keller, Dr. John McCoy, and Dr. David Whitten for all their help in my research. Thank you to my committee members for their review and support of my work.

I give special thanks to Tom Corbitt, Lance Edens, Tom Gamble, Tony Garcia, Kyle Fenton, Sergio Mendez, Shailendra Rathod, Robin Simons, Sebastian Wieße, Martina Shürman, Xinyu Cao, and Fanny Liu who 'fought in the trenches of research with me'. Our conversations, successes, hopes, and dreams will not be forgotten.

I give the greatest gratitude to Koo Im Tong, my love, who has helped me and kept me optimistic in rough times. To my brother, Brad Andrzejewski, who is my best friend. My mom and dad, and my mother and father in-law, for their never ending support.

Bioadhesion to Model Thermally Responsive Surfaces

by

Brett Paul Andrzejewski

ABSTRACT OF DISSERTATION

Submitted in Partial Fulfillment of the
Requirements for the Degree of

Doctor of Philosophy
Chemical Engineering

The University of New Mexico

Albuquerque, New Mexico

November, 2009

Bioadhesion to Model Thermally Responsive Surfaces

by

Brett Paul Andrzejewski

B.S. Chemical Engineering, University of New Mexico
Albuquerque, New Mexico 2002

Ph.D., Chemical Engineering, University of New Mexico, 2010

Abstract

This dissertation focuses on the characterization of two surfaces: mixed self-assembled monolayers (SAMs) of hexa(ethylene glycol) and alkyl thiolates (mixed SAM) and poly(*N*-isopropylacrylamide) (PNIPAAm). The synthesis of hexa(ethylene gylcol) alkyl thiol ($C_{11}EG_6OH$) is presented along with the mass spectrometry and nuclear magnetic resonance results. The gold substrates were imaged prior to SAM formation with atomic force micrscopy (AFM). Average surface roughness of the gold substrate was 0.44 nm, 0.67 nm, 1.65 nm for 15, 25 and 60 nm gold thickness, respectively. The height of the mixed SAM was measured by ellipsometry and varied from 13 to 28 $\AA$ depending on surface mole fraction of $C_{11}EG_6OH$. The surface mole fraction of $C_{11}EG_6OH$ for the mixed SAM was determined by X-ray photoelectron spectroscopy (XPS) with optimal thermal responsive behavior in the range of 0.4 to 0.6. The mixed SAM surface was confirmed to be thermally responsive by contact angle goniometry, 35° at 28 °C and ∼55° at 40 °C. In addition, the mixed SAM

surfaces were confirmed to be thermally responsive for various aqueous mediums by tensiometry. Factors such as oxygen, age, and surface mole fraction and how they affect the thermal responsive of the mixed SAM are discussed. Lastly, rat fibroblasts were grown on the mixed SAM and imaged by phase contrast microscopy to show inhibition of attachment at temperatures below the molecular transition. Qualitative and quantitative measurements of the fibroblast adhesion data are provided that support the hypothesis of the mixed SAM exhibits a dominantly non-fouling molecular conformation at 25 °C whereas it exhibits a dominantly fouling molecular conformation at 40 °C.

The adhesion of six model proteins: bovine serum albumin, collagen, pyruvate kinase, cholera toxin subunit B, ribonuclease, and lysozyme to the model thermally responsive mixed SAM were examined using AFM. All six proteins possessed adhesion to the pure component alkyl thiol, in contrast possessed no adhesion to the pure component $C_{11}EG_6OH$ SAM at both temperatures examined, 25 and 40 °C. The protein adhesion data to the mixed SAM also supports the hypothesis that the mixed SAM displays a non-fouling molecular conformation at 25 °C whereas it displays a dominantly fouling molecular conformation at 40 °C.

Advancing contact angles obtained through tensiometry were used to find the surface free energy of the mixed SAM before and after the thermal response using the van Oss-Good-Chaudhury method. The surface tension values obtained, 42 and 38 mN/m for 22 and 40 °C, respectively, are not dissimilar enough with regard to error to make conclusions. In a similar manner, the surface free energy of another mixed SAM composed of alkyl and trimethylamine thiolates was also calculated.

PNIPAAm brushes grown on a silicon substrate by atom-transfer radical polymerization (ATRP) were imaged by AFM and characterized by XPS. The height of the resulting brushes could be controlled from ∼5 to 55 nm by reaction time. A thermal response was observed for polymer brushes with a length greater than 20

nm. For polymer brush lengths greater than 20 nm, the static contact angle at 22 °C was 35° and varied from 60 to 80° at 40 °C. The thermal response was also observed using the captive bubble method.

Force-distance curves of the PNIPAAm brushes were taken with an unmodified silicon nitride AFM cantilever at incremental temperature steps. At room temperature the force-distance data was fit to the Alexander-de Gennes model resulting in a hydrated polymer length of 235 nm. The Young's modulus was calculated using the Hertz model and changed from ∼80 MPa at 26 °C to ∼350 MPa at 40 °C. The solvent condition of the Alexander-de Gennes model was set to the case of good solvent and showed close match to the force-distance data at 26 °C. The match was not as close when the solvent condition was set to theta solvent condition and compared to the force-distance data at 40 °C.

Finally, the effective diffusion coefficients of a dye were obtained for the uptake, encapsulation, and release from a lipid bilayer coated mesoporous particle using a mathematical solution to the experimental system. The resulting effective diffusion coefficients are: $1*10^{-12}$ m^2/s, $0.4*10^{-12}$ m^2/s, and $0.7*10^{-12}$ m^2/s for uptake, encapsulation, and release, respectively. The particles are characterized by scanning electron microscopy and nitrogen adsorption measurements. In contrast to our hypothesis, the lipid bilayer did not completely inhibit diffusion of the rhodamine dye from the particles when encapsulated.

Contents

List of Figures **xiii**

List of Tables **xxiii**

1 Introduction **1**

2 Mixed SAMs as Thermally Responsive Bioadhesive Surfaces **5**

2.1 Introduction 5

2.2 Materials and Methods 10

2.3 Results and Discussion 16

2.3.1 Mixed $C_{11}EG_6OH/C_{11}CH_3$ SAM characterization 16

2.3.2 Thermal response of the mixed $C_{11}EG_6OH/C_{11}CH_3$ SAM . . . 22

2.3.3 Rat fibroblast growth on mixed $C_{11}EG_6OH/C_{11}CH_3$ SAMs . . 26

2.3.4 Degradation of the mixed $C_{11}EG_6OH/C_{11}CH_3$ SAM 37

2.4 Conclusion 43

3 Bioadhesion to Thermally Responsive Surfaces 45

3.1 Introduction 45

3.2 Materials and Methods 50

3.3 Results and Discussion 52

3.4 Conclusion 73

4 Lewis Acid-Base Surface Energies of Mixed Self-Assembled Monolayers 75

4.1 Introduction 75

4.2 Materials and Methods 79

4.3 Results and Discussion 80

4.3.1 Lewis acid-base surface tensions of mixed $C_{11}EG_6OH/C_{11}CH_3$ SAMs 87

4.4 Conclusion 90

5 Synthesis and Characterization of PNIPAAm Thin Films 91

5.1 Introduction 91

5.2 Materials and Methods 96

5.3 Results and Discussion 98

5.4 Conclusion 108

6 Force Interactions with Poly(*N*-isopropylacrylamide) Thin Films 109

6.1 Introduction 109

6.2 Material and Methods 117

6.3 Results and Discussion 118

6.3.1 Soft press 118

6.3.2 Hard press 123

6.4 Conclusion 136

7 Creation and Utilization of Lipid Bilayer Coated Mesoporous Silica Particles 138

7.1 Introduction 138

7.2 Materials and Methods 142

7.3 Results and Discussion 144

7.4 Conclusions 154

8 Conclusions and Outlook 155

Glossary 158

.1 Additional information 159

References 164

List of Figures

2.1 Molecular conformation states of the $C_{11}EG_6OH$ molecule in a single component SAM, taken from Harder, et al. [1] 7

2.2 Thickness of pyruvate kinase adsorption at various temperatures and surface mole fractions of $C_{11}EG_6OH$ in a mixed SAM measured by ellipsometry, taken from Prime et al. [2] 9

2.3 Reversible adsorption of the protein lysozyme on the mixed $C_{11}EG_6OH$, $C_{11}CH_3$ SAM surface measured by ellipsometry, taken from Balamurugan, et al. [3] 10

2.4 $C_{11}EG_6OH$ thiol synthesis 12

2.5 AFM micrographs of three gold deposition thickness on glass coverslips. 17

2.6 XPS spectra of the various volume fractions of commercial obtained $C_{11}EG_6OH$ mixed with $C_{11}CH_3$. 19

2.7 Calculation of the thickness of the SAM layer by linear interpolation of the area of the Au 4f peak, graphic made by Xinyu Cao. 22

2.8 Thermal responsiveness observed by contact angle for commercially obtained $C_{11}EG_6OH$ mixed with $C_{11}CH_3$. One sample was used with three sessile drop measurements, error no greater than 5°. 23

2.9 Cyclic thermal responsiveness observed by contact angle for commercially obtained $C_{11}EG_6OH$ mixed with $C_{11}CH_3$. One sample was used with three sessile drop measurements, error no greater than 5°. 24

2.10 Characterization of thermal drift of the captive bubble contact angle on a native silicon wafer in nanopure water. One sample was used with three captive bubble measurements, error report is deviation between measurements. 25

2.11 Effects of various buffer solutions on advancing contact angle measured by tensiometry for the mixed $C_{11}EG_6OH/C_{11}CH_3$ SAM. The media tested were phosphate buffered saline (PBS), water 18.3 MΩ/cm, tris(hydroxymethyl)aminomethane (TRIS) buffer, and artificial sea water (ASW). One sample was used with three advancing conctact angle measurements, error report is deviation between measurements. 26

2.12 Fibroblast growth on the various surfaces at 37 °C after incubation for 3 days. A is the untreated glass control, B the pure component $C_{11}CH_3$ SAM, C the pure component $C_{11}EG_6OH$, D is the mixed $C_{11}CH_3/C_{11}EG_6OH$ SAM. One concatentated image is shown of the three images sets taken randomly from entire surfaces. 28

2.13 Fibroblast growth on the various surfaces at 29 °C after incubation for 3 days. A is the untreated glass control, B the pure component $C_{11}CH_3$ SAM, C the pure component $C_{11}EG_6OH$, D1 is one image the mixed $C_{11}CH_3/C_{11}EG_6OH$ SAM showing no fibroblast attachment, while D2 is another area imaged showing fibroblast attachment. One image of the three randomly examined areas is shown, two images are shown of the mixed $C_{11}CH_3/C_{11}EG_6OH$ SAM to show the patchy attachment of the fibroblasts. 29

2.14 Patchy fibroblast attachment on the mixed $C_{11}CH_3/C_{11}EG_6OH$ SAMs at 37 °C after incubation for 3 days. 30

2.15 Quantification of adhered fibroblasts grown at a temperature above, 37 °C, and below, 29 °C the change in molecular conformation to the various SAM surfaces, $C_{11}EG_6OH$ is abbrev. as OEG, $C_{11}CH_3$ abbrev. as CH3, and mixed $C_{11}CH_3/C_{11}EG_6OH$ SAM abbrev. as MIXED. 31

2.16 Fibroblast growth after 3 days at 37 °C in a incubator on mixed $C_{11}CH_3/C_{11}EG_6OH$ SAM prior to wash step. 33

2.17 Concatentation of nine images taken from a movie examining the entire mixed $C_{11}CH_3/C_{11}EG_6OH$ SAM after three gentle rinses with 4 °C DMEM solution. Figure 2.16 is the the surface prior to the rinsing. 33

2.18 High resolution XPS scans of the carbon 1s mixed SAM surface after immersion in DMEM for 1,2, and 3 days at 37 °C. 36

2.19 High resolution XPS scans of the oxygen 1s mixed SAM surface after immersion in DMEM for 1, 2, and 3 days at 37 °C. 37

2.20 Thermal responsiveness observed by contact angle for synthesized $C_{11}EG_6OH$ mixed with $C_{11}CH_3$. 39

2.21 Images of rat fibroblasts on various SAM surfaces. The rat fibroblasts growing outside the initial non-SAM circles on each surface show how the passivated areas degrade with time, tri(ethylene gylcol) is the right most image set. Image taken from Luk et al. [4] 40

3.1 The adhesive force of a BSA coated AFM tip measured during the LCST of PNIPAAm measured by AFM, taken from Cho et al. [5] . 50

3.2 AFM micrograph of a mixed SAM surface on the gold coated circular coverslip, taken in air. 53

3.3 3D reconstruction of a mixed $C_{11}EG_6OH/C_{11}CH_3$ SAM surface on a gold coated circular coverslip. 54

3.4 Force-distance curve of a bare AFM tip into a hard glass surface at 22 °C, standard deviation is 5 pN. 55

3.5 A typical force curve at 22 °C on the mixed $C_{11}EG_6OH/C_{11}CH_3$ SAM with BSA coating on the AFM cantilever. 56

3.6 A force curve at 22 °C exhibiting a "compression" of the layer underneath the AFM cantilever ($C_{11}EG_6OH/C_{11}CH_3$ SAM with BSA on the AFM cantilever). 57

3.7 Schematic of the AFM cantilever and SAM to scale. 58

3.8 An atypical adhesion force curve at 22 °C of BSA on the mixed $C_{11}EG_6OH/C_{11}CH_3$ SAM with BSA coating on the AFM cantilever. 59

3.9 A typical force distance curve showing the adhesion of BSA to the mixed $C_{11}EG_6OH/C_{11}CH_3$ SAM at 39 °C 60

3.10 Force-distance curves between fibrinogen and the $C_{11}EG_3Me$ SAM on gold (a) and silver (b). The $C_{11}EG_3Me$ molecule displays the helical conformation on the gold surface, while displaying the all trans conformation on the silver surface. Force-distance curves were performed in the temperature range of 27 to 30 °C. Image taken from [6]. 61

3.11 Plot of the double adhesion, or denaturing, of collagen to the mixed $C_{11}EG_6OH/C_{11}CH_3$ SAM at 39 °C 62

3.12 BSA adhesion to the pure component SAMs at high and low temperature, where a) is the $C_{11}EG_6OH$ at 22 °C, b) is the $C_{11}EG_6OH$ at 39 °C c) is the $C_{11}CH_3$ at 22 °C, and d) is $C_{11}CH_3$ at 39 °C. . . . 64

3.13 Adhesion force histograms of the various proteins to the mixed $C_{11}EG_6OH/C_{11}CH_3$ SAM at 22 °C, where a) is bovine serum albumin, b) is collagen, c) is pyruvate kinase, d) is cholera toxin subunit B, e) is ribonuclease A, and f) is lysozyme. 65

3.14 Adhesion force histograms of the various proteins to the mixed $C_{11}EG_6OH/C_{11}CH_3$ SAM at 39 °C, where a) is bovine serum albumin, b) is collagen, c) is pyruvate kinase, d) is cholera toxin subunit B, e) is ribonuclease A, and f) is lysozyme. 66

3.15 Sequential adhesion force measurements as a function of run number for the various proteins to the mixed SAM surface at 39 °C. a) is bovine serum albumin, b) is collagen, c) is pyruvate kinase, d) is cholera toxin subunit B, e) is ribonuclease A, f) is lysozyme. Measurements were terminated in each case after five consecutive measurements of no adhesion. 70

4.1 Example of the Lewis acid-base interacts 77

4.2 High resolution XPS spectrum of pure $C_{11}CH_3$ and NMe_3 surfaces . 81

4.3 High resolution XPS spectrum of a pure NMe_3 SAM with compositional fit. 83

4.4 Surface volume fraction compared to the volume fraction used to create the mixed $NMe_3/C_{11}CH_3$ SAM surfaces. 84

4.5 Contact angles for various liquid on the mixed $NMe_3/C_{11}CH_3$ SAM surfaces. Error is less than 5°. 84

4.6 The Lifshitz-van der Waals surface tension for the various fractions of mixed SAMs 85

4.7 The acid and base surface tensions for the various fractions of mixed $NMe_3/C_{11}CH_3$ SAMs, error is not shown and is no greater than 2 mJm^{-2} 86

4.8 Mixed $C_{11}EG_6OH/C_{11}CH_3$ SAM surface tension 88

4.9 Mixed $C_{11}EG_6OH/C_{11}CH_3$ SAM acidic component of surface tension 89

4.10 Mixed $C_{11}EG_6OH/C_{11}CH_3$ SAM basic component of surface tension 89

5.1 Chemical structure of PNIPAAm 92

5.2 Schematic of the ATRP reaction 94

5.3 Pre-attachment of initiator to the surface of silicon (left) 95

5.4 ATRP reactants 95

5.5 PNIPAAm grafted silicon thin film product 95

5.6 AFM micrograph in air of the ATRP grown PNIPAAm surface on a silicon wafer. 99

5.7 PNIPAAm thickness measured by ellipsometry as a function of polymerization time, fit is a ATRP kinetics model taken from literature [7] 100

5.8 Survey XPS spectrum of the initiator self-assembled monolayer on the silicon wafer 102

5.9 High resolution C 1s XPS spectrum of the initiator self-assembled monolayer, upper most curve. Lower curves are carbon bonding fits produced by CasaXPS analysis software. 103

5.10 Survey XPS spectrum of PNIPAAm on the silicon wafer 104

5.11 High resolution XPS spectrum of the carbon 1s peak of the ATRP grown PNIPAAm. Lower curves are carbon bonding fits produced by CasaXPS analysis software. 105

5.12 Contact angles for PNIPAAm at 22 and 40 °C measured by captive bubble goniometry. 107

5.13 Difference in contact angle between 40 °C and 22 °C measured by captive bubble goniometry. 107

6.1 Force-distance plot of polymer surfaces of various lengths taken with SFA, taken from [8]. 113

6.2 Force-distance plot of the various polymer lengths shown with the model of Alexander-de Gennes, taken from [8]. 114

6.3 Illustration of the variables and conditions in the force-distance experiment 115

6.4 AFM data showing the compression of the PNIPAAm film after modification of the x-axis to show Z 119

6.5 Force-distance curves at room temperature for AFM, x, SFA, triangle, and de Gennes theory, solid line [9, 10]. 120

6.6 Force-distance curves at room temperature for AFM, square, SFA, triangle, and density function theory, solid line [9, 10]. 121

6.7 Force-distance curves on the PNIPAAm brushes at various temperatures. Force-distance curves at 26, 32, and 36 °C have been omitted for clarity. 122

6.8 Slope of the force distance curve at 150 pN as a function of temperature measured by AFM soft cantilever 123

6.9 Schematic showing the notation of the force distance experiments on PNIPAAm 124

6.10 Force distance curves showing indentation into the PNIPAAm surface 125

6.11 a) Fit of the Hertz model to the force-distance data to evaluate the Young's Modulus of the PNIPAAm brush. For easier comparison the data in Figure 6.11a) plotted log-log in b). 126

6.12 PNIPAAm Young's modulus calculated from the Hertz model as a function of temperature. Error bars are the sumation of error in all the data processing steps. 127

6.13 Schematic and modulus of polystyrene brushes in a good solvent taken by oscillating AFM force measurements taken from Overney et al. [11]. 129

6.14 PNIPAAm force-distance curves for temperatures below the LCST. . 130

6.15 PNIPAAm force-distance curves for temperatures above the LCST. . 131

6.16 PNIPAAm force-distance curve at 26 °C shown with the Alexander-de Gennes model with good solvent condition. 132

6.17 PNIPAAm force-distance curve at 40 °C shown with the Alexander-de Gennes model with theta solvent condition. 133

6.18 Alexander-de Gennes model for Helmholtz free energy with good solvent condition with integrated force-distance data at 26 °C 134

6.19 Alexander-de Gennes model for Helmholtz free energy with theta solvent condition with integrated force-distance data at 39 °C 135

7.1 Chemical structure of egg phosphatidylcholine 139

7.2 Schematic of the various lipid vesicle types, A shows a multilamellar vesicle, B a large unilamellar vesicle, C a small unilamellar vesicle, D a multivesicular vesicle, image taken from Walde and Ichikawa [12]. 140

7.3 Diagram of the lipid bilayer on a particles, taken from Linseisen, et al. [13] 141

7.4 Chemical structure of sulforhodamine 101 acid chloride (Texas Red). Diameter of the molecule is approximately 1.8 nm and has no net charge at pH 7.0. 142

7.5 SEM micrograph of the nucleosil particle after base/peroxide wash . 145

7.6 SEM micrograph of the nucleosil particle showing surface roughness 146

7.7 SEM micrograph of the nucleosil particle showing the pores perpendicular to the particle surface. 146

7.8 Plot of amount of dye in solution with the particle against time during uptake and theoretical solution for diffusion into a sphere. D_{eff} value is = $1*10^{-12}$ m^2/s. 149

7.9 Plot of the amount of dye in solution with the particle against time during encapsulation and theoretical solution for diffusion out of a sphere. D_{eff} value is = $0.4*10^{-12}$ m^2/s. 152

7.10 Plot of the amount of dye in solution with the particle against time during release and theoretical solution for diffusion out of a sphere. D_{eff} value is = $0.7*10^{-12}$ m^2/s. 153

List of Tables

2.1 Surface loading of $C_{11}EG_6OH$ thiol calculated from XPS in Figure 2.6 20

2.2 Elemental composition from XPS survey spectra of the various SAMs, n=3, standard deviations are less than 2% 20

2.3 High Resolution C1s composition from XPS spectra of the various SAMs, n=3, standard deviations are less than 2% 21

2.4 Chemical composition ,%, of the mixed SAMs after immersion in DMEM for 1, 2 and 3 days. 35

2.5 High Resolution C1s composition from XPS spectra removal from DMEM for various times, n=3, standard deviations are less than 2% 35

3.1 List of proteins and properties used the adhesion to mixed SAM experiment. 52

3.2 Table of protein adhesion forces to SAM surfaces at 22 °C with experimental parameters taken from literature. 72

3.3 Table of protein adhesion forces to the SAM surfaces at 39 °C. . . . 73

4.1 Elemental composition from XPS survey spectra of the SAMs, one sample scanned in three areas, standard deviation is less than 2%. . 82

4.2 High Resolution C1s composition from XPS spectra of the SAMs, one sample scanned in three areas, standard deviation is less than 2%. 82

4.3 Surface tension values used in the calculation of surface free energy of the mixed SAMs. Values taken from [14] or documentation provided by Kruss for tensiometry. 86

4.4 Surface tension values of the mixed $C_{11}EG_6OH/C_{11}CH_3$ SAMs . . . 87

5.1 Elemental composition from XPS survey spectra of initiator surface, one sample scanned in three areas, standard deviation is less than 2%.102

5.2 High Resolution C1s composition from XPS spectra of the initiator, one sample scanned in three areas, standard deviation is less than 2%.103

5.3 Elemental composition from XPS survey spectra of initiator surface, one sample scanned in three areas, standard deviation is less than 2%.104

5.4 High Resolution C1s composition from XPS spectra of the PNIPAAm polymer, one sample scanned in three areas, standard deviation is less than 2%. 106

6.1 Values of Young's Modulus relevant to PNIPAAm thin films 128

.1 Ribbon scructures of the proteins used in mixed $C_{11}EG_6OH/C_{11}CH_3$ SAM experiment. 161

.2 List of protein sizes used the adhesion to mixed $C_{11}EG_6OH/C_{11}CH_3$ SAM experiment. 162

.3 Amino acid composition of the protiens used in the mixed $C_{11}EG_6OH/C_{11}CH_3$ SAM experiments 162

.4 Surface tension values used in the calculation of surface free energy of the mixed $C_{11}EG_6OH/C_{11}CH_3$ SAMs 163

.5 2nd Root solutions to the Lewis acid base equation 163

Chapter 1

Introduction

Mankind realized the need to control bioadhesion as early as 2000 years ago, when the Phoenicians and Carthaginians applied pitch, or distilled wood tar, to the bottom of ships to prevent biofouling by algae and other marine organisms [15]. Since that time, ship builders have attempted to prevent bioadhesion by using materials such as lead sheathed wood, copper paneling and nails, arsenic and sulfur mixed with oil, and tributyl-tin [15]. Today the need to control bioadhesion on ship hulls is even greater. In fact, the United States Navy spends millions of dollars a year to clean Navy ship hulls in order to maintain streamline efficiency, which saves fuel, allows for faster travel, and minimizes the production of greenhouse gases [15, 16]. However, many of the methods currently used to control this type of bioadhesion are toxic to the environment and regulatory action will soon end their usage [15, 17]. As a result, scientists are actively seeking solutions to replace the toxic compounds currently used to prevent the biofouling of marine vessels.

Bioadhesion also plays a critical role in the medical field, where for example, the bioadhesion of bacteria on transplant devices can lead to biofouling [18], one million infections per year (2004) [19], and in some cases, death [20]. When a foreign

material is implanted into a patient, an adsorbed protein layer develops around the device [21, 22]. Once this occurs, the biofouled device may fail or be rejected by the body. This type of biofouling may also cause transplant devices to have a shorter operational period in the body than their designed functional life.

Not all bioadhesion is detrimental to human life; indeed, without bioadhesion multicellular life would not be possible [23, 24, 25]. Cell-to-cell adhesion is necessary to give rise to the ordered structure of tissue, from which organs are composed. Because of the integral role bioadhesion plays in nature, scientists now realize the potential uses for bioadhesion if it can be controlled and manipulated. In more recent years bioadhesion has been used to grow human tissue into organs, which have been successfully transplanted in human patients [26].

Currently, medical scientists are working to develop a surface from which skin cells can adhere, grow, and be released when needed for skin grafts [27, 28, 29]. The development of such a surface has many obvious benefits and could be used to treat a variety of different conditions, including: burns, melanoma, tattoo removal, psoriasis, and skin infections. The same surface could be used to selectively adsorb and release proteins on demand, which may then be used in biometric identification, proteomics, protein separation, and biosensing. A stimuli responsive surface capable of controlling bioadhesion could also be used to prevent the biofouling of ship hulls and transplanted devices. Indeed, the potential uses for a stimuli responsive material capable of controlling bioadhesion are nearly limitless.

In order to create a stimuli responsive surface capable of controlling bioadhesion, it is desirable to first study the chemical and physical changes of the surface before and after the stimuli response. These changes are important because they may indicate what factors influence bioadhesion. In turn, these factors may be used not only to predict and control the stimuli response regulating bioadhesion, but also to develop new materials with similar stimuli responsive properties.

To better understand the chemical and physical changes of a surface before and after the stimuli response, we qualified and quantified the characteristics of two model thermally responsive materials before and after the stimuli response. The two model thermally responsive materials used for this study are, a mixed self-assembled monolayer (SAM) of hexa(ethylene glycol) thiolate ($C_{11}EG_6OH$) and dodecane thiolate ($C_{11}CH_3$), and atom-transfer radical polymerized (ATRP) poly-(N-isopropylacrylamide) (PNIPAAm). We selected these two model surfaces because both surfaces are easy to characterize and reproduce.

Chapter 2 presents the characterization of the mixed $C_{11}EG_6OH/C_{11}CH_3$ SAM. To understand the thermal response of the mixed $C_{11}EG_6OH/C_{11}CH_3$ SAM, the thin film was characterized using both physical and chemical methods. In addition, the thin film was characterized by the growth of rat fibroblasts using several controls. We confirmed that the mixed SAM is thermally responsive by using two different methods: a change in contact angle goniometry and tensiometry using various buffer solutions. Chapter 2 also reports on our observations on the stability of the thiols, composing the mixed SAM.

Chapter 3 examines the bioadhesion of several proteins to the thermally responsive mixed $C_{11}EG_6OH/C_{11}CH_3$ SAM using atomic force microscopy (AFM). Chapter 3 presents the data collected from the force of bioadhesion of several model proteins to the model stimuli responsive surface at temperatures above and below the molecular transition of the thermally responsive mixed SAM. Chapter 3 concludes with a discussion on the many forces that influence protein bioadhesion to a thermally responsive surface.

Chapter 4 calculates the surface free energy of two mixed SAMs using the Lewis acid-base (LAB) method. The surface free energy was calculated for the thermally responsive mixed $C_{11}EG_6OH/C_{11}CH_3$ SAM above and below the temperature at which it is thermally responsive. The surface free energy was also calculated for

an alkyl and trimethylamine thiolates mixed SAM surface at a single temperature because the alkyl and trimethylamine thiolates mixed SAM surface is not thermally responsive.

Chapter 5 reports on the physical and chemical characterization of the thermally responsive material, PNIPAAm. Chapter 5 describes the growth of the PNIPAAm polymer from a silicon surface using ATRP. Surface characterization of the PNIPAAm polymer confirms the polymer growth, its thermal response, and chemical identity.

Chapter 6 presents the characterization of PNIPAAm by AFM. The AFM was used to study the polymeric properties of the polymer thin film, and confirm the thermal response of PNIPAAm. The Alexander-de Gennes model was used to examine the solvent condition, steric force profiles, and surface free energy of PNIPAAm.

In Chapter 7 a mathematical solution to the diffusion process was used to quantify the diffusion from a lipid encapsulated mesoporous particle. A mesoporous particle covered with a lipid vesicle, that models a biosensor or living cell, was used to study mass transport before, during, and after lipid bilyer encapsulation. The mesoporous particles used in the experiment were characterized by scanning electron microscopy (SEM).

There are several means to study bioadhesion to model stimuli responsive surfaces. The work contained within this dissertation only scratches the surface of a vast field of study. This work examines some of the factors that influence bioadhesion. It is our hope that this work may be useful to scientists and researchers working to control bioadhesion.

Chapter 2

Mixed Self-Assembled Monolayers as Model Thermally Responsive Bioadhesive Surfaces

2.1 Introduction

Generally speaking, bioadhesion is the attachment of biological objects, such as proteins, carbohydrates, lipids, bacteria, and other cells to a surface. To understand how bioadhesion is affected by the surface to which an object adheres, this study used stimulus responsive surfaces that are easy to reproduce and characterize. A stimuli responsive surface is important because it may be used to control bioadhesion. For example, it was first observed that by mildly heating a mixed self-assembled monolayer (mixed SAM) of hexa(ethylene glycol) alkyl thiolate ($C_{11}EG_6OH$) and dodecane thiolate ($C_{11}CH_3$), proteins will adsorb, whereas the adsorption of proteins to a mixed SAM of $C_{11}EG_6OH/C_{11}CH_3$ will be inhibited when cooled [2].

This chapter begins by reviewing the most current and relevant literature on the

$C_{11}EG_6OH$ SAM. It then describes the synthesis of the $C_{11}EG_6OH$ thiol molecule that was used in the creation of the mixed SAM. Next, it details the formation of thermally responsive mixed SAM. This explanation is followed by a discussion of the factors that influence the thermal responsive behavior of mixed SAM. Finally, this chapter examines how the mixed SAM influences fibroblast adhesion. This study does not characterize the mechanism for the thermal responsive behavior of the mixed SAM. This chapter will provide a researcher with all the information necessary to reproduce and further scientific studies on the thermally responsive mixed SAM.

It is a well established fact that poly(ethylene glycol) modified surfaces resist adsorption of proteins [30]. However, the molecular mechanism for protein resistance to poly(ethylene glycol) surfaces is not well understood. Whitesides et al. speculated that a shorter chain length of ethylene glycol would aid in understanding the protein resistant properties of poly(ethylene glycol) [31]. $C_{11}EG_6OH$ was synthesized and used to form SAMs; the resulting SAMs were characterized with X-ray photoelectron spectroscopy, water contact angle goniometry, and ellipsometry [31]. It was later confirmed that pure $C_{11}EG_6OH$ SAM also resists protein adsorption [32]. In another study, the length of the ethylene glycol section of the thiol was changed from one segment to six, to examine how it affected protein adsorption [2]. The shorter ethylene glycol molecule is now known to resist the adsorption of proteins like poly(ethylene glycol), but the mechanism for protein resistance to $C_{11}EG_6OH$ is still not well understood.

Spectroscopic examination of the SAM provides molecular information about the protein resistant properties of $C_{11}EG_6OH$ SAM. Using sum frequency generation spectroscopy (SFG), X-ray photoelectron spectrosopy (XPS), and Fourier transformed infrared spectroscopy (FTIR), it was found that pure $C_{11}EG_6OH$ SAMs can have two types of molecular conformation [1]. The two types of molecular conformation observed in $C_{11}EG_6OH$ are illustrated in Figure 2.1. One conformation is helical,

with the molecule rotating around a central axis with *guache* bonds [2]. The other is an all *trans* conformation, where the ethylene glycol section of the $C_{11}EG_6OH$ molecule is elongated [2].

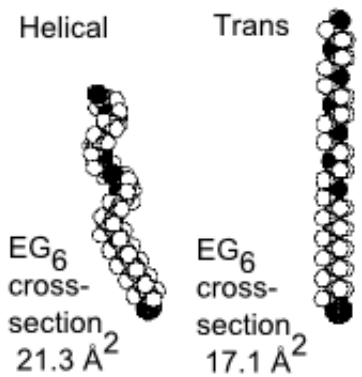


Figure 2.1: Molecular conformation states of the $C_{11}EG_6OH$ molecule in a single component SAM, taken from Harder, et al. [1]

In a later study it was found that the molecular conformation of the ethylene glycol section of the molecule is dependent on the lateral packing density of the SAM [33]. In that study, the *trans* conformation was found to occur only on SAMs on a silver substrate; while the *guache* conformation was found predominently on SAMs formed on a gold substrate. Surfaces that exhibit an all *trans* molecular conformation allow protein adsorption, while surfaces that hold the helical conformation resist protein adsorption [1]. The cross-sectional area of the helical conformation of the $C_{11}EG_6OH$ molecule is 21.3 $\mathring{A}$ whereas the *trans* conformation is 17.1 $\mathring{A}$, the change in height of the two conformations has not been observed [1]. These results were confirmed with atomic force microscopy (AFM) on methoxytri(ethylene gylcol) (EG_3Me) SAM. The EG_3Me SAM on silver containing the *trans* molecular conformation exhibited adhesion to a fibrinogen coated AFM cantilever [6]. In contrast, EG_3Me SAM containing the *guache* conformation on gold exhibited no adhesion to a fibrinogen coated AFM cantilever [6].

In 2001, an examination of temperature dependent protein adsorption was studied using gold and silver $C_{11}EG_6OH$ SAMs [34]. In that study, it was shown that the SAMs of $C_{11}EG_6OH$ resisted protein adsorption from 0 °C to 80 °C. This study is significant because it demonstrates that a component of the mixed SAM is resistant to protein adhesion at many different temperatures. By contrast, the thermally responsive mixed SAM described above shows protein resistance only at temperatures below 32 °C [3].

Molecular simulation is another method by which to study resistance to protein adsorption by the $C_{11}EG_6OH$ molecule. In one study that used Monte Carlo simulations, it was shown that water molecules penetrate into the $C_{11}EG_6OH$ SAM only in the helical conformation; while the all *trans* conformation was shown to resist water molecule penetration [35]. The amount of hydrogen bonding between the water medium and surface, and the resulting hydrophilicity, is important to protein resistance [36]. Pertsin et al. believe that this phenomenon is the reason why $C_{11}EG_6OH$ in the helical conformation resisted protein adsorption. Pertsin et al. posit that tightly bound water molecules hydrating the $C_{11}EG_6OH$ molecule may act as a barrier against the adsorption of proteins [35]. As a result, proteins may interact with the hydrating water layer while never coming into contact with the $C_{11}EG_6OH$ molecule. The interface between water and $C_{11}EG_6OH$ was also studied using a computer model, resulting in the same conclusions [37].

While a single component SAM can resist bioadhesion, mixed component SAMs can be manipulated to control bioadhesion. In one study, SAMs similar to $C_{11}EG_6OH$ were synthesized from a SAM of carboxyl terminated thiolates. The partial reaction created a mixed SAM of carboxyl terminated and ethylene gylcol terminated thiolates. The resulting mixed SAM showed resistance to protein adsorption. This resistance is attributed to the shielding of the shorter carboxyl groups by the longer ethylene glycol molecule in the mixed SAM [38]. Prime et al. created a mixed SAM

of $C_{11}EG_6OH$ and $C_{11}CH_3$ to examine the effect of protein adhesion on surface mole fraction. This study resulted in two very important findings. First, it was discovered that there is a specific mole fraction of $C_{11}EG_6OH$ above which the surface resisted protein adhesion. Second, it was shown that the protein adsorption of pyruvate kinase is temperature dependent. Figure 2.2 shows the results of the protein adhesion to the mixed SAM of $C_{11}EG_6OH$ and $C_{11}CH_3$. These results led our research group to hypothesize that the mixed SAM surface might be thermally responsive. A collaborative effort between our research group and Michael Grunze's showed by SFG spectroscopy and contact angle that the mixed $C_{11}EG_6OH/C_{11}CH_3$ SAM was thermally dependent [3]. The reversible protein adsorption to the mixed SAM surface can be seen in Figure 2.3. Ellipsometric measurements show protein adsorbing at 37 °C, and after a rinse step shows no adsorption at 25 °C.

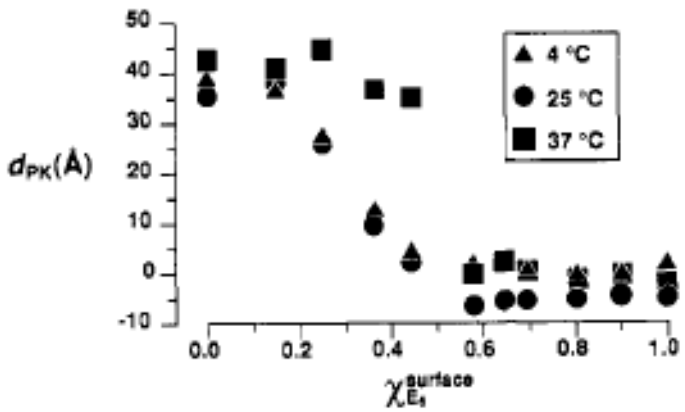


Figure 2.2: Thickness of pyruvate kinase adsorption at various temperatures and surface mole fractions of $C_{11}EG_6OH$ in a mixed SAM measured by ellipsometry, taken from Prime et al. [2]

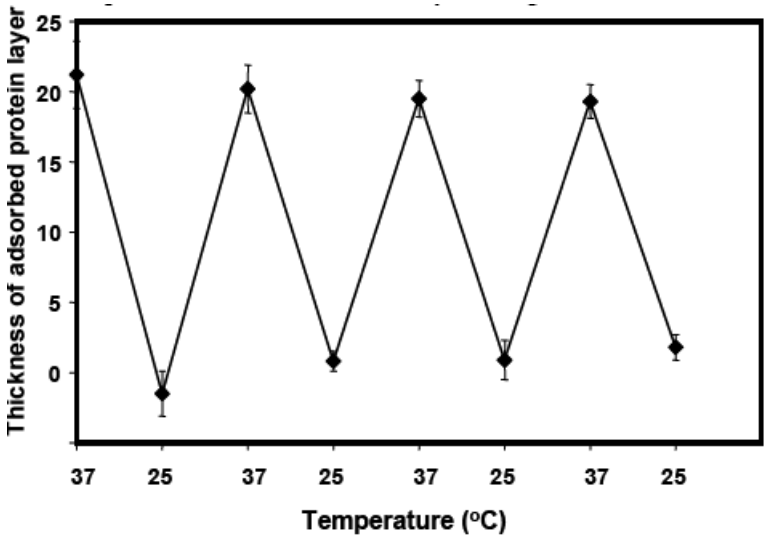


Figure 2.3: Reversible adsorption of the protein lysozyme on the mixed $C_{11}EG_6OH$, $C_{11}CH_3$ SAM surface measured by ellipsometry, taken from Balamurugan, et al. [3]

Balamarugan et al. posited that the change in protein adhesion to the surface is due to the change in molecular confirmation of the $C_{11}EG_6OH$ molecule, and not the result of dehydration [3]. Rather, Balamarugan et al. posit that dehydration of the $C_{11}EG_6OH$ molecule would result in changes in SFG spectra, which were not observed. I hypothesize that the protein resistant helical confirmation is dominantly present in the mixed SAM at 25 °C, while the non-protein resistant *trans* confirmation is dominantly present in the mixed SAM at 37 °C.

2.2 Materials and Methods

Materials Gold (99.999%) 1-3 mm spheres came from Plasmaterials. Chromium rods were aquired from the Mathius Company. $C_{11}EG_6OH$ was synthesized as previously described [32] or purchased from Prochimia, Poland. Dodecane thiol 98%, decane thiol 98%, undecane thiol 98%, hexadecane thiol 98%, benzene thiol 98%,

Dulbecco's phosphate buffered saline (PBS) salt 1x, pH 7.4, and Tris buffer were purchased from Aldrich Chemicals and used as recieved. Ethanol (absolute, 200 proof;) Aaper Alcohols and Chemical Company. Artificial sea water (ASW) produced in house using 24.6 g sodium chloride, 0.67 g potassium chloride, 1.36 g calcium chloride dihydrate, 6.29 g magnesium sulfate septahydrate, 4.66 g magnesium chloride hexahydrate, 0.18 g sodium bicarbonate, and Nanopure water, pH adjusted to 8.0 using HCl. Nanopure water (18.3 MΩ/cm) produced in-house. Tris(hydroxymethyl)aminomethane (TRIS) buffer pH adjusted to 7.4 using HCl.

Materials characterization Ellipsometry was performed with an M-44 ellipsometer from J.A. Woolam Co. The thickness of the SAM layer was measured at least 3 times on different areas of the sample and the average taken. Sessile drop contact angles were taken with a Rame-Hart contact angle goniometer. Temperatures were controlled with a heating ribbon and monitored by a thermocouple. Tensiometer measurements were performed with a Kruss K-100. An external water circulating bath was used to control the temperature of the tensiometer fluid vessel. Tensiometer measurements in each solvent were performed at room temperature (22°C) recording the advancing and receding contact angles. The advancing contact angles are used throughout this work. An external temperature bath raised the surface tension apparatus and test solution temperature to 40 ± 1 °C. Atomic force microscopy images were taken with a Veeco Nanoscope IIIa instrument with software version 4.31 and a silicon nitride cantilever, nominal radius of 10 nm, on a vibration isolation system.

$C_{11}EG_6OH$ synthesis The reaction for synthesis of hexa(ethylene glycol) thiol is shown in Figure 2.4. The first step was to add undecane bromide and hexa(ethylene glycol) in dry DMF and let reaction occur in nitrogen environment for 24 hours. Products were purified by column chromatography over silica in ethyl acetate. Step 1 products were dissolved in deoxygenated methanol and reacted in a UV-quartz vessel for 6 hours. Products were purified by column chromatography over silica in

chloroform/methanol 2:1 by volume. Step 2 products were dissolved in deoxygenated methanol at 60 °C and HCl was added and let react for 24 hours. Products were purified by column chromatography over silica in ethyl acetate. Mass spectrometry showed a large amount of a material at 957.0 m/z ratio. This molecule was likely $C_{11}EG_6OH$ disulfide which was reduced as follows. $C_{11}EG_6OH$ thiol was dissolved in tetrahydrofuran (THF) and a 5 molar excess of lithium aluminum hydride ($LiAlH_4$) was added and let react for 2 hours. Reaction was stopped by placing reaction vessel in an ice bath. Products were separated by separatory funnel using chloroform.

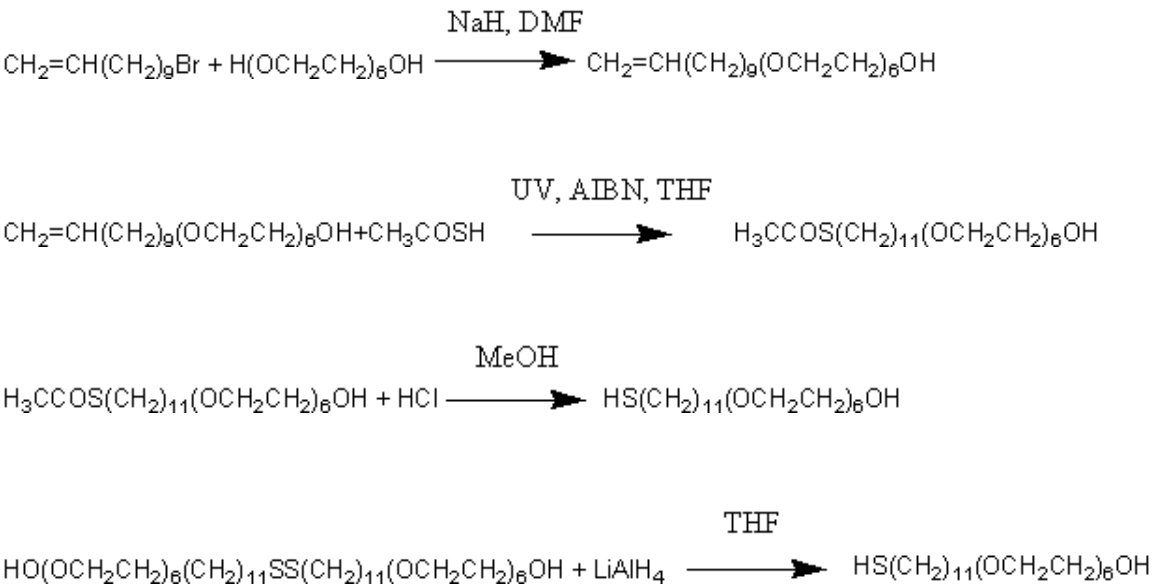


Figure 2.4: $C_{11}EG_6OH$ thiol synthesis

Analysis of $C_{11}EG_6OH$ thiol synthesis

Nuclear magnetic resonance (NMR) spectroscopy was performed after all synthesis steps by a Bruker NMR spectrometer at the Univeristy of Heidelberg, Germany. All spectra were taken at 300 MHz using deuterated chloroform as the solvent ($CDCl_3$). The major peaks from the proton and carbon spectra of the final product ($C_{11}EG_6OH$) are:

^{1}H NMR (300 MHz, $CDCl_3$):
1.2-1.4 (m, 14H), 1.30 (t, J=7.7Hz, 1H), 1.5-1.6(m,4H), 2.48(quart, J=7.4Hz, 2H), 3.35 (s,3H), 3.41 (t, J=6.8Hz, 2H), 3.5-3.6 (m,4H), 3.6-3.7 (m,20H)

^{12}C NMR (300 MHz, $CDCl_3$):
δ 24.6, 26.0, 29.4, 34.0, 61.6, 70.5, 76.6, 77.0, 77.4

Mass spectrometry was performed after all synthesis steps using matrix-assisted laser desorption/ionization (MALDI) with a Bruker Biflex spectrometer at the Univeristy of Heidelberg, Germany. The major peaks from the mass spectrum of the final product ($C_{11}EG_6OH$) are:

MS (MALDI): m/z 172, 190, 491 [$C_{11}EG_6OH$ thiol], 696, 957 [$C_{11}EG_6OH$ disulfide, trace]

SAM preparation SAMs were prepared as previously described [3]. Glass microscope slides (Schott AG or VWR) were rinsed with ethanol and sonicated for 15 minutes. Slides were placed in Piranha etch, 75% H_2SO_4 25% H_2O_2, for 2 hours. Slides were thoroughly rinsed with water (18.3MΩ/cm) and kept in a sealed container with water until metal evaporation. Slides were thoroughly dried and 3 nm of titanium or chromium was deposited on the slides, followed by the desired amount

of gold. 30 nm of gold was used for optically transparent slides and 200 nm for non-transparent slides. Optically transparent slides were used in cellular observations, while the non-transparent slides were used in characterization. A solution of 2.5 mM $C_{11}EG_6OH$ was created with deoxygenated ethanol. A solution of 2.5 mM $C_{11}EG_6OH$ and CH_3 were created using a 95:5 (vol/vol) ratio. The gold slides were cleaned by UV ozone cleaning for 2 hours if not fresh from metal evaporation. The gold slides were then placed in the mixed thiol solution and left overnight. The slides were removed from solution and rinsed with ethanol and dried in a stream of nitrogen.

Rat fibroblast growth and incubation REF-52 established rat fibroblasts were kindly provided by the Spatz research group at the University of Heidelberg in their sixth cell culture passage. The supply strain of fibroblast was kept in standard incubation conditions (37 °C, 5% CO_2) in Dulbco's Modified Eagle Medium (DMEM) with 5% Fetal Bovine Serium (FBS) and 0.1% antibiotics (100 U/ml penicillin, 100 g/ml streptomycin, and 0.25 g/ml amphotericin B). The cell line was split weekly, 10% of the cells were used to innoculate a virgin growing vessel while the remainder was used for cell loading on experimental samples. Seeding densities were on the order of 60,000 cells per centimeter calculated via a cell images from the culture flask. Trypsin was used to enzymatically remove the fibroblasts from the growth plate. Fibroblasts were used from their sixth to fifteenth cell culture passage. DMEM and trypsin were kept at 37 °C prior to usage. The SAM surfaces were removed from the thiol solution and rinsed with 70% ethanol three times, before rinsing with 37 °C DMEM three times. Fibroblasts were then seeded on the test surfaces. All rat fibroblast manipulations were performed in a sterile laminar flow hood, with sterilized tweezers, and sterile pipettes and tips. Samples were kept in incubation conditions, either 37 or 29 °C 5% CO_2, until observation.

Rat fibroblast characterization to the mixed $C_{11}EG_6OH/C_{11}CH_3$ SAM

A Ziess phase contrast microscope was setup so that images could be captured on a CCD camera mounted to the microscope. A movable x-y micropositioning stage was setup so multiple areas of the SAM surface could be examined by the microscope. The stage also doubled as a heating element where the temperature could be controlled from 22 to 60 ± 0.1 °C and was set to the incubation temperature used in the experiment.

XPS characterization of post DMEM samples Mixed SAMs of $C_{11}EG_6OH$ and $C_{11}CH_3$ were created as previous described. A DMEM solution was created with 10% FBS. Three samples were placed into this solution and allowed to sit for 24 hours, 48 hours and 72 hours at 37 °C. After the samples were removed from solution they were thoroughly rinsed with 1x PBS solution and dried in a stream of nitrogen and stored in a hermetically double sealed container with nitrogen. Samples were shipped to NESAC/BIO at the University of Washington for XPS analysis.

XPS spectra of the DMEM stored samples were taken on a Kratos Axis-Ultra DLD spectrometer. This instrument has a monochromatized Al Kα X-ray and a low energy electron flood gun for charge neutralization. X-ray spot size for these acquisitions was on the order of 300 x 700mm (Kratos 'Hybrid' mode). Pressure in the analytical chamber during spectral acquisition was less than 5 x 10^{-9} Torr. Pass energy for survey and detail spectra was 80 eV. Pass energy for high resolution scans was 20 eV. The take-off angle (the angle between the sample normal and the input axis of the energy analyzer) was 0° (0 degree take-off angle @ 100 $\mathring{A}$ sampling depth). Three areas per sample were analyzed per sample per experiment. The Kratos Vision2 software program was used to determine peak areas and to calculate the elemental compositions from peak areas. The binding energy scale for identification of elements was calibrated using the C 1s peak set to 285.0 eV. All sample handling and sample cutting was done with double solvent cleaned tweezers and scissors. The solvents used were acetone and methanol (both HPLC grade). All

sample handling utensils were cleaned before and after sample handling. Fit peaks were constrained by a full width half maximum value between 1.2 and 2 eV.

2.3 Results and Discussion

2.3.1 Mixed $C_{11}EG_6OH/C_{11}CH_3$ SAM characterization

The gold surfaces without SAMs present on the surface were characterized by AFM. The three thickness of gold are shown on glass coverslips, shown in Figure 2.5. The coverslips were used because they were assured by the manufacturer to be smoother than glass microscope slides. As the gold thickness increases, the 'rolling hills' topography becomes more apparent. The average surface roughness of the gold thickness are: 0.44 nm, 0.67 nm, 1.65 nm for 15, 25 and 60 nm gold thickness, respectively. This value was calculated by the AFM software over the entire surface scan, peak to valley height difference.

Mixed $C_{11}EG_6OH/C_{11}CH_3$ surfaces were sucessfully created and characterized via ellipsometry, contact angle goniometry, and XPS. The ellipsometric thickness varied from 13 $\AA$ for pure $C_{11}CH_3$ to 28 $\AA$ for pure $C_{11}EG_6OH$. The ellipsometric values are exactly consistent with those reported by Pale Grosdemange et al., 13 ± 2 $\AA$ for $C_{11}CH_3$ and 28 ± 2 $\AA$ for $C_{11}EG_6OH$ SAMs [31]. Sessile (static) drop contact angles varied from 110° for pure $C_{11}CH_3$ SAM to 26° for pure $C_{11}EG_6OH$. The value for the methyl terminated SAM is identical to that reported in the literature, 110° [39]. The contact angle for the $C_{11}EG_6OH$ SAM is slightly lower than the reported values: 34-38° advancing contact angle and 22-25° receding contact angle [31] and 39° sessile [3]. If this value of the sessile drop is not truely static (but was evaporating during the time of measurement), it would be closer to the receding angle measurement. The measurement was taken in Albuquerque, where the relative humidity averages

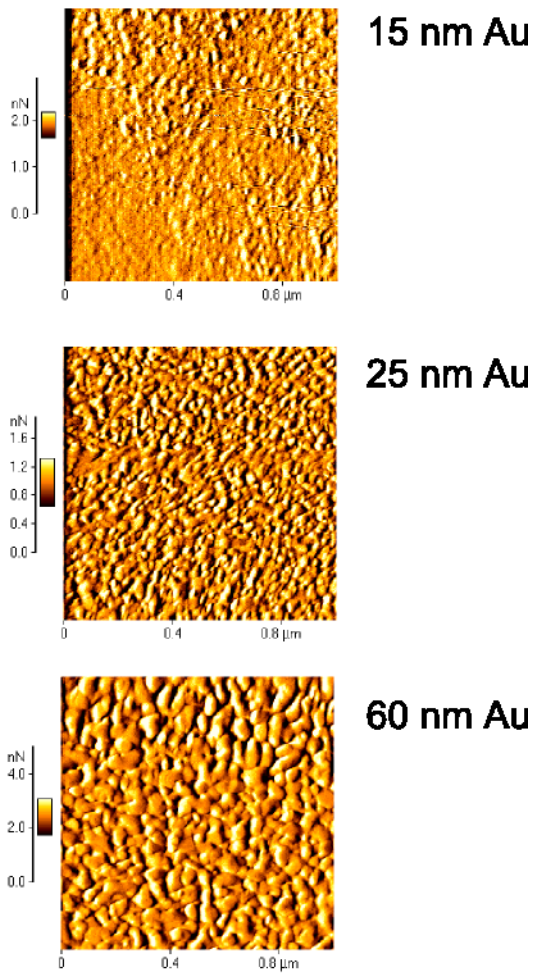


Figure 2.5: AFM micrographs of three gold deposition thickness on glass coverslips.

20%; thus evaporation and a receding angle measurement are likely.

The XPS spectra for the mixed $C_{11}EG_6OH$ samples are shown in Figure 2.6. The pure $C_{11}CH_3$ SAM is shown with a red curve, having a peak at 285 eV. The pure $C_{11}EG_6OH$ is shown in gold, with a peak at 285 eV and another peak at 286.8 eV. The volume fractions of each thiol solution are shown as an inset on the graph in

ascending order of $C_{11}EG_6OH$ to $C_{11}CH_3$. The nearly 2 eV distance between the peaks is consistent with the reported literature [31], although there is a 0.5 eV shift in peaks to higher energy for the alkyl and ether carbons in our spectra. The shift is from the data fitting of the C 1s peak to 285.0 eV. The surface mole fraction of $C_{11}EG_6OH$ can be calculated from the XPS spectra in Figure 2.6. The area of the carbon or oxygen peaks can be used to determine the surface loading of the SAM, Equation 2.1 [2]. The area of the fitted peaks of the high resolution carbon spectra are used to calculated the surface mole fraction of $C_{11}EG_6OH$. These values are displayed in Table 2.1. A very similar result can be obtained when the elemental peaks are fit to the survey spectrum using CasaXPS software. The results can be seen in Table 2.3. Table 2.2 shows the high resolution carbon 1s composition.

$$\chi_{OEG} = \frac{Area_{O1s}(Unknown - CH_3)}{Area_{O1s}(OEG - CH_3)} \tag{2.1}$$

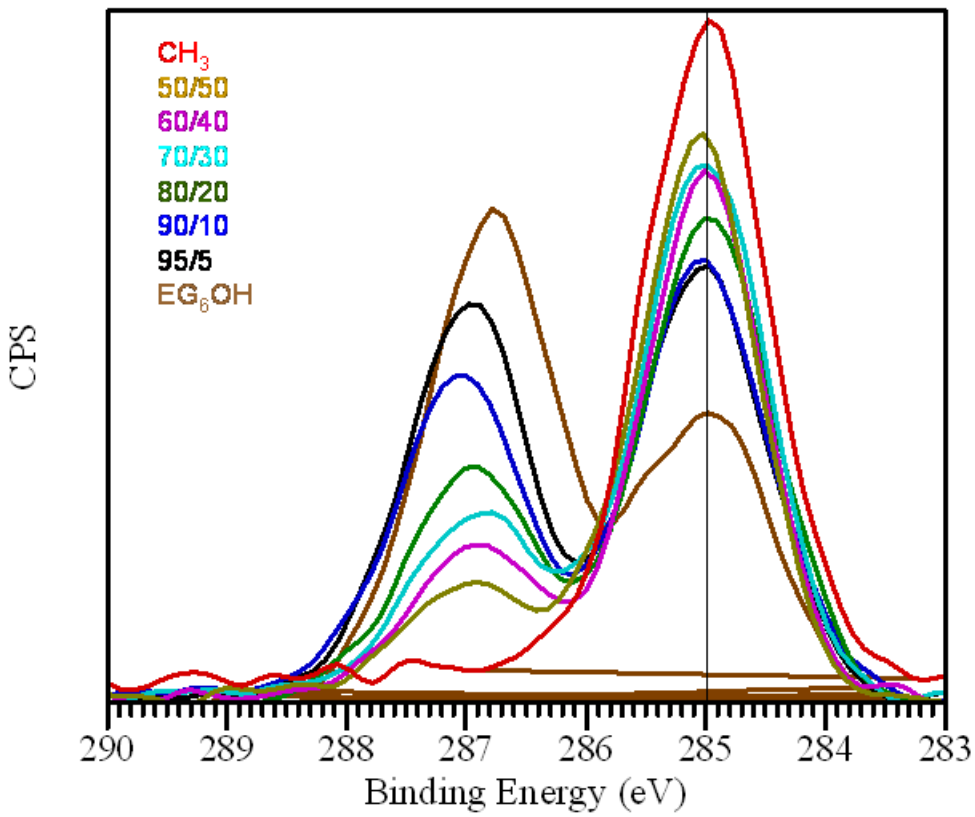


Figure 2.6: XPS spectra of the various volume fractions of commercial obtained $C_{11}EG_6OH$ mixed with $C_{11}CH_3$.

From the data in Figure 2.6 and Table 2.1 it is observed that very high volume fractions of $C_{11}EG_6OH$ thiol solution result in nearly 1:1 surface mole fraction. I believe this result comes from two factors: 1) the $C_{11}EG_6OH$ molecule being more soluble in ethanol than $C_{11}CH_3$, and 2) the $C_{11}EG_6OH$ molecule being bulker and having a slow diffusion coefficient. When the gold surface is place in solution the two thiols are in competition for surface binding sites. The less soluble and faster diffusing $C_{11}CH_3$ molecule has a faster binding rate than $C_{11}EG_6OH$, thus the higher volume fraction are needed to yield a 1:1 surface mole ratio.

It is possible to calculate the thickness of the SAM using the decrease in area of

Table 2.1: Surface loading of $C_{11}EG_6OH$ thiol calculated from XPS in Figure 2.6

vol % $C_{11}EG_6OH$ thiol	Carbon 1s % $C_{11}EG_6OH$ surface loading	Oxygen 1s %$C_{11}EG_6OH$ surface loading
100	100	100
95	76	84
90	65	70
80	53	62
70	45	49
60	38	43
50	32	39
0	0	0

Table 2.2: Elemental composition from XPS survey spectra of the various SAMs, n=3, standard deviations are less than 2%

SAM	C %	O %	N %	S %
$C_{11}CH_3$	100	0	0	0
50	73	26	0	0
60	81	19	0	0
70	70	30	0	0
80	63	37	0	0
90	56	44	0	0
95	49	51	0	0
$C_{11}EG_6OH$	45	54	0	0

the Au 4f peak measured by XPS. The attenuation of the Au 4f peak comes scattering of the photoelectrons which can be described by modifying Beer-Lambert's Law. The modification to Beer-Lambert's Law is:

$$I_a = I_o exp(\frac{-d}{\lambda_{KE}} cos\theta) \tag{2.2}$$

where I_a is the attentuated photoelectron signal from the unknown SAM thickness, I_o is the photoelectron signal from a gold surface with no SAM present, d is the unknown SAM thickness, λ_{KE} is the wavelength at a set energy, and θ is the take-off angle [40]. The decrease in peak area to SAM height is shown in Figure

Table 2.3: High Resolution C1s composition from XPS spectra of the various SAMs, n=3, standard deviations are less than 2%

SAM	C-H %	C-O %
$C_{11}CH_3$	100	0
50	83.3	16.7
60	77.8	22.2
70	73.4	26.6
80	68.7	31.3
90	57.4	42.6
95	52.3	47.7
$C_{11}EG_6OH$	36.5	63.5

2.7. It is more common to examine the SAM thickness via ellipsometry. While XPS tends to yield both more accurate and precise values, the results by ellipsometry are more quickly obtained. The SAM thickness can also be used to determine the mixed SAM surface mole fraction. The mixed SAM thickness should be between the height of a pure $C_{11}CH_3$ SAM, 13 $\mathring{A}$, and a pure $C_{11}EG_6OH$ SAM, 28 $\mathring{A}$. Both XPS and ellipsometry report an averaged thickness value over a sample area containing only two thicknesses, thus the reported thickness is a measure of the surface mole fraction.

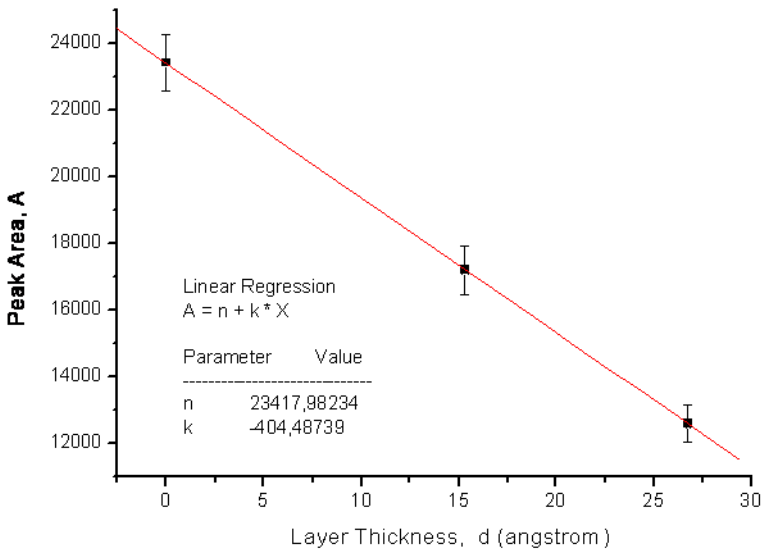


Figure 2.7: Calculation of the thickness of the SAM layer by linear interpolation of the area of the Au 4f peak, graphic made by Xinyu Cao.

2.3.2 Thermal response of the mixed $C_{11}EG_6OH/C_{11}CH_3$ SAM

Figure 2.8 shows the change in contact angle of the mixed SAM containing commercially obtained $C_{11}EG_6OH$. The commercially obtained $C_{11}EG_6OH$ contained less than 5% disulfide and exhibits a relatively large change in contact angle with change in temperature. The amount of disulfide was calculated by the area of the mass spectroscopy thiol peak at 491 to disulfide peak at 957 m/z. The change in contact angle at 32 °C is also not as sharp as previously published [3], the change is more gradual and occurs over a span of temperatures from 8 to 10 degrees Celsius. Several volume fractions yield a thermally responsive surface. Figure 2.9 shows the reversibility of the change in contact angle for the mixed $C_{11}EG_6OH/C_{11}CH_3$ SAM over several temperature cycles. The thermal response was greatest for the initial

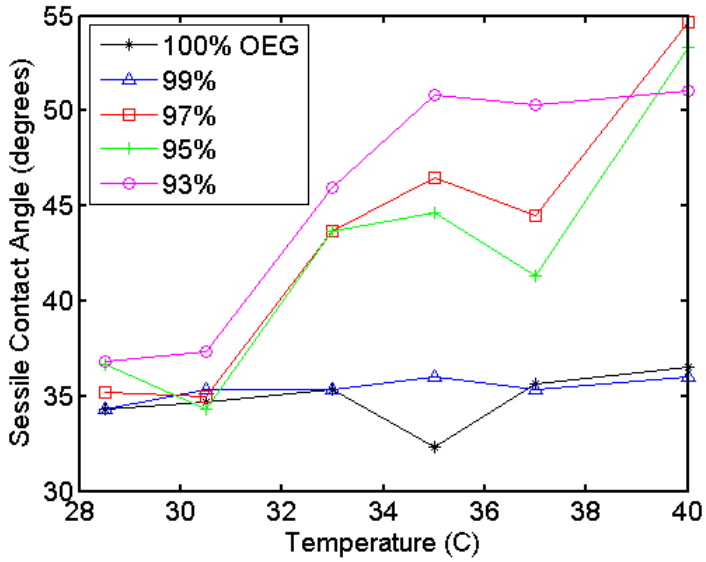


Figure 2.8: Thermal responsiveness observed by contact angle for commercially obtained $C_{11}EG_6OH$ mixed with $C_{11}CH_3$. One sample was used with three sessile drop measurements, error no greater than 5°.

thermal cycle and then slightly decreased for the following thermal cycles. It may be that the SAM is undergoing molecular rearrangement on the gold surface possibly phase separating. It may also be that the thiolate bond to the gold is being oxidized to sulfonate, the sulfonate is then easily displaced by another thiol molecule [41]. Another plossible explanation being the degredation of the ethylene glycol section of the $C_{11}EG_6OH$ molecule [4].

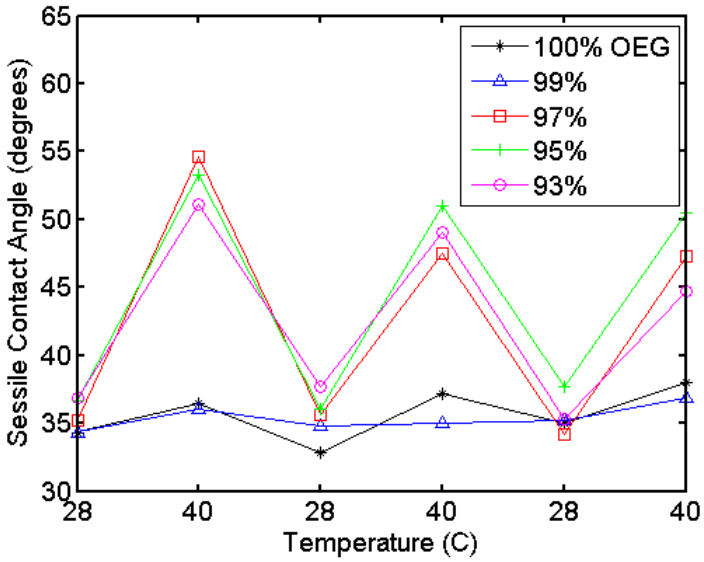


Figure 2.9: Cyclic thermal responsiveness observed by contact angle for commercially obtained $C_{11}EG_6OH$ mixed with $C_{11}CH_3$. One sample was used with three sessile drop measurements, error no greater than 5°.

To ensure that the change in contact angle is a property of the surface (and not due to the temperature dependence of the surface tension of water), a control was run. The effect of temperature on the contact angle is often minimal, -0.1° per Kelvin for temperature changes of the liquid [42]. It is also known that the value of the surface tension of a liquid decreases with temperature until the critical temperature, *Tc*, where liquid and gas phase are identical [43]. In Figure 2.10 the change in contact angle on a native silicon surface is measured for a change in temperature. The data points are the average of three measurements on a single surface with the standard deviation of measurements as error bars. The contact angle changes by 6° over 20 °C, which is higher than the prediction of Adamson [42]. The prediction is for the change of surface tension of water with change in temperature and should be applicable to any contact angle measurement technique.

The advancing contact angle measured by tensiometry for the various solution

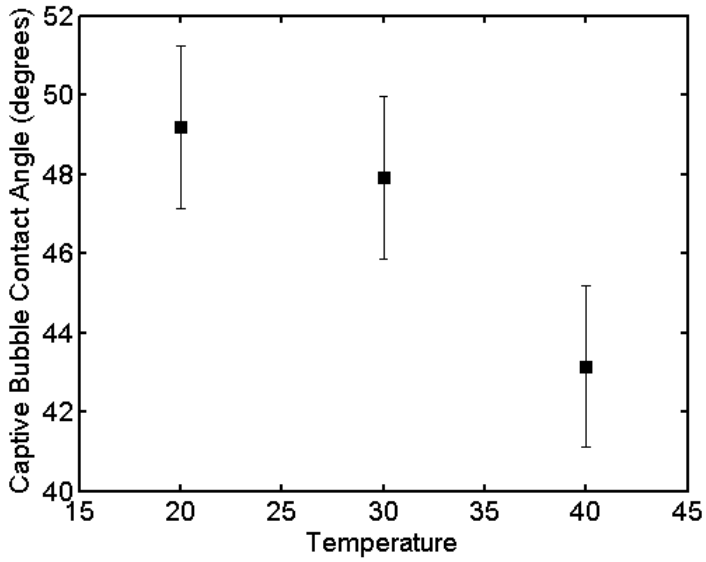


Figure 2.10: Characterization of thermal drift of the captive bubble contact angle on a native silicon wafer in nanopure water. One sample was used with three captive bubble measurements, error report is deviation between measurements.

media can be seen in Figure 2.11. It is interesting to note that the change in contact angle for water is much smaller than shown in Figures 2.8, 2.9, and 2.20. The method used to calculate the contact angle in the tensiometer, Wilhelmy plate method, may have additional influence from the sides of the slide, may be explaining the difference between the measurement types. However, the change in contact angle becomes more pronounced for various buffer solutions. The change in contact angle for the mixed $C_{11}EG_6OH/C_{11}CH_3$ SAM surface is about 10 times that of the predicted value for pure water-surface interactions. These data along with the sum frequency spectroscopy data published by Balamarugan et al. confirm the thermally responsive behavior of the mixed SAM surface [3].

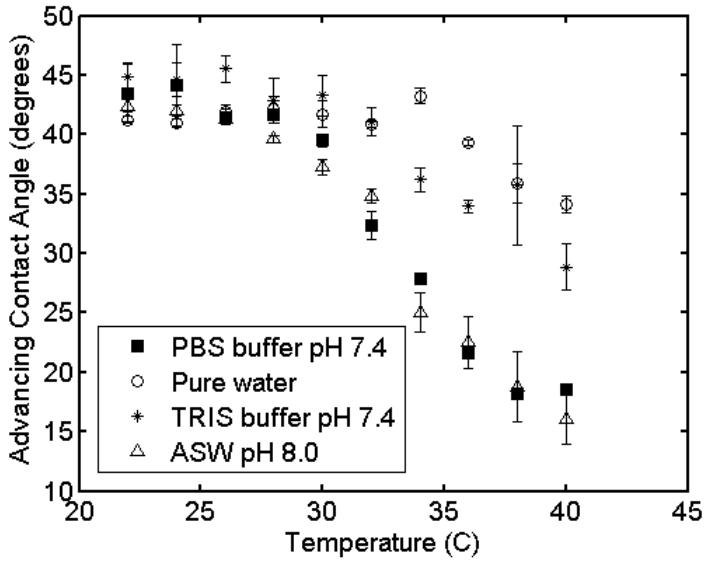


Figure 2.11: Effects of various buffer solutions on advancing contact angle measured by tensiometry for the mixed $C_{11}EG_6OH/C_{11}CH_3$ SAM. The media tested were phosphate buffered saline (PBS), water 18.3 MΩ/cm, tris(hydroxymethyl)aminomethane (TRIS) buffer, and artificial sea water (ASW). One sample was used with three advancing conctact angle measurements, error report is deviation between measurements.

2.3.3 Rat fibroblast growth on mixed $C_{11}EG_6OH/C_{11}CH_3$ SAMs

It was believed that the the mixed $C_{11}EG_6OH/C_{11}CH_3$ SAM surface would be a reversible adhesive to mammalian cells. Rat fibroblasts were grown on the mixed $C_{11}EG_6OH/C_{11}CH_3$ SAM surface along with control surfaces of the individual component thiolates and untreated glass in the modified DMEM solution for three days. The experiment was performed at 37 °C and 29 °C. To examine the fibroblasts after the growth period, twelve images were taken that generated a 0.9 by 1.2 mm rectangular image of the surface. Each test surface was imaged three times by the method described at random locations. The concatenated images for each surface are

shown in Figure 2.12. Figure 2.12A is the untreated glass surface. Fibroblast growth reached confluency on this control and was used as a baseline for fibroblast growth in normal conditions. Figure 2.12B shows the fibroblast attachment on the $C_{11}CH_3$ surface. The attachment on the $C_{11}CH_3$ surface is less than that of the glass control, implying the fibroblast attachment was inhibited by the $C_{11}CH_3$ SAM. The fibroblasts on the surface also appear cylindrical in shape and filipodia are more elongated. Figure 2.12C is the $C_{11}EG_6OH$ surface where fibroblast attachment is also inhibited by the surface chemistry when compared to the glass control. This is consistent with literature reports for the anti-fouling nature of ethylene glycol molecules. Again the fibroblasts appear cylindrical and attachment points elongated. Figure 2.12D shows the fibroblast attachment on the mixed SAM surface. The fibroblast attachment on the mixed SAM surface appears to be more like the glass control in fibroblast attachment. The appearance of the fibroblasts is also more closely related to the glass control, in that the fibroblast appear semi-circular and do not exhibit elongated filipodia connections to the surface. The other two areas examined were consistent with the concatenated images shown in Figure 2.12.

The same experiment was performed but the incubation temperature was changed to 29 °C resulting in Figure 2.13. Again the experiment was performed on several surfaces to act as controls for the change in attachment conditions to the thermally responsive mixed SAM. Figure 2.13A shows the fibroblast attachment on the untreated glass. It should be noted that fibroblast growth and attachment is reduced by the lower incubations temperature. The fibroblasts that did attach showed a semi-circular growth pattern along with large filipodia on the surface. The $C_{11}CH_3$ terminated thiolate surface is in Figure 2.13B, where fibroblast attachment is again reduced by the lower temperature yet still shows semi-circular appearance of the fibroblast. Figure 2.13C is the $C_{11}EG_6OH$ surface where fibroblast attachment was completely inhibited. The mixed SAM surface in Figure 2.13D1 and 2.13D2 show an interesting phenomena. On some areas examined fibroblast attachment was com-

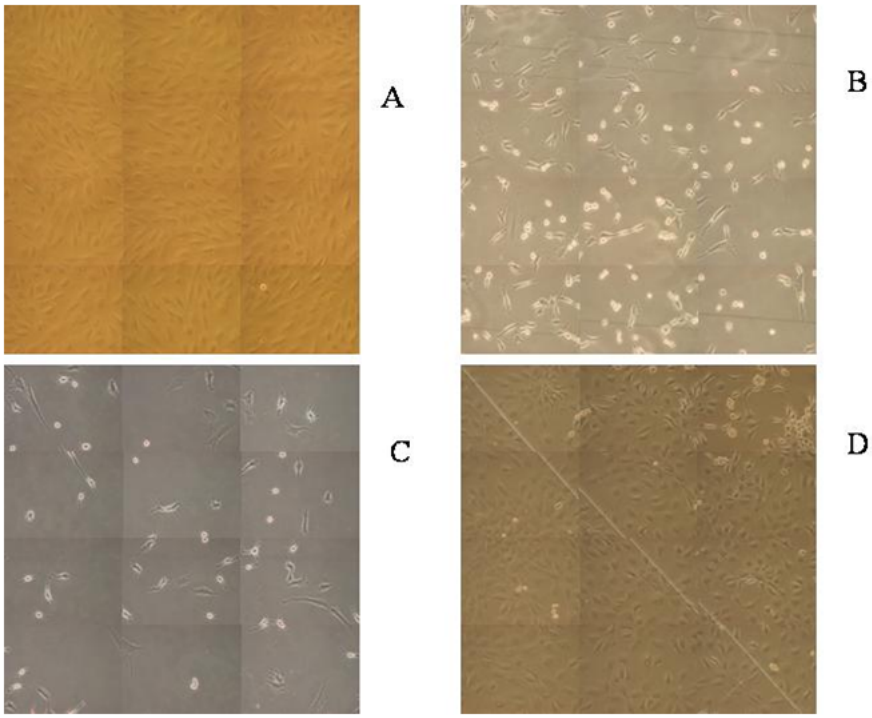


Figure 2.12: Fibroblast growth on the various surfaces at 37 °C after incubation for 3 days. A is the untreated glass control, B the pure component $C_{11}CH_3$ SAM, C the pure component $C_{11}EG_6OH$, D is the mixed $C_{11}CH_3/C_{11}EG_6OH$ SAM. One concatentated image is shown of the three images sets taken randomly from entire surfaces.

pletely inhibited, Figure 2.13D1. In other areas of examination, fibroblast attachment was not completely inhibited, Figure 2.13D2. It is possible that some areas contain more $C_{11}CH_3$ thiolate and offer more friendly attachment conditions. While other areas are thermally responsive inhibiting the attachment of the fibroblasts. The island pattern of fibroblast attachment was seen on several mixed SAM samples.

The island, or patchy, attachment of the rat fibroblasts was also seen at 37 °C. Figure 2.14 shows one of the areas of observation showing both confluent attachment and attachment inhibition. This patchy attachment gave rise to high error when the cellular attachment was quantified.

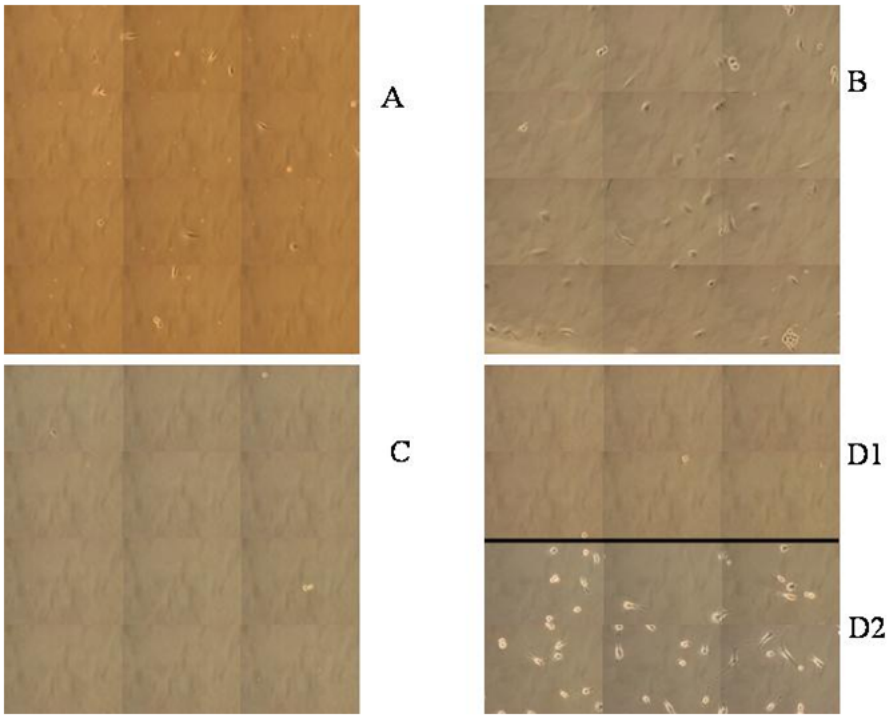


Figure 2.13: Fibroblast growth on the various surfaces at 29 °C after incubation for 3 days. A is the untreated glass control, B the pure component $C_{11}CH_3$ SAM, C the pure component $C_{11}EG_6OH$, D1 is one image the mixed $C_{11}CH_3/C_{11}EG_6OH$ SAM showing no fibroblast attachment, while D2 is another area imaged showing fibroblast attachment. One image of the three randomly examined areas is shown, two images are shown of the mixed $C_{11}CH_3/C_{11}EG_6OH$ SAM to show the patchy attachment of the fibroblasts.

The images in Figure 2.12 and Figure 2.13 were quantified by counting the number of adhered cells and divided by the area of examination, thus the fibroblast cell density is obtained. Non-attached or dying cells were neglected from count by visual examination and personal judgement. The values from the three areas of the concatenated images were averaged, and plotted in Figure 2.15. The large error bar in the mixed SAM data comes from the comparision of the three positions on the surface. Some areas allowed fibroblast growth while other areas did not. Because mixed SAMs of $C_{11}EG_6OH$ and $C_{11}CH_3$ allow protein adhesion above the molecular

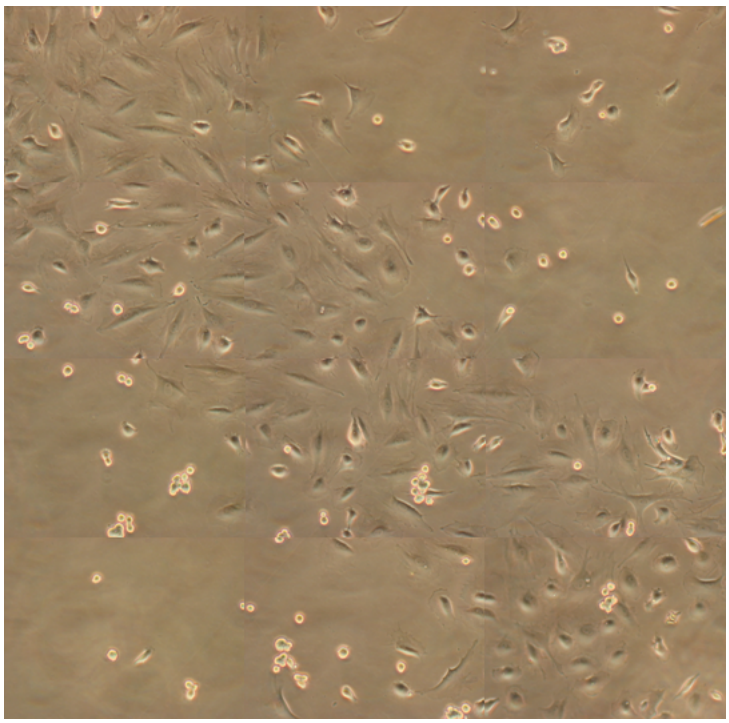


Figure 2.14: Patchy fibroblast attachment on the mixed $C_{11}CH_3/C_{11}EG_6OH$ SAMs at 37 °C after incubation for 3 days.

conformation change (temperatures ¿32 °C) [3], something must be changing the surface chemistry to prevent cell adhesion. This will be discussed in more detail later in this chapter. The data supports the existing evidence that for temperatures above the molecular conformational change, proteins adsorb (ie, the binding proteins present on the fibroblasts), while proteins do not adsorb for temperatures below the molecular conformational change [3].

In a final experiment to prove our hypothesis, rat fibroblasts were grown for three days in incubation conditions on each of the test surfaces. The surface was imaged and the 12 concatenated images are shown in Figure 2.16. The patchy growth of the rat fibroblasts are observed showing regions of well spread fibroblasts next to areas displaying dendritic growth.

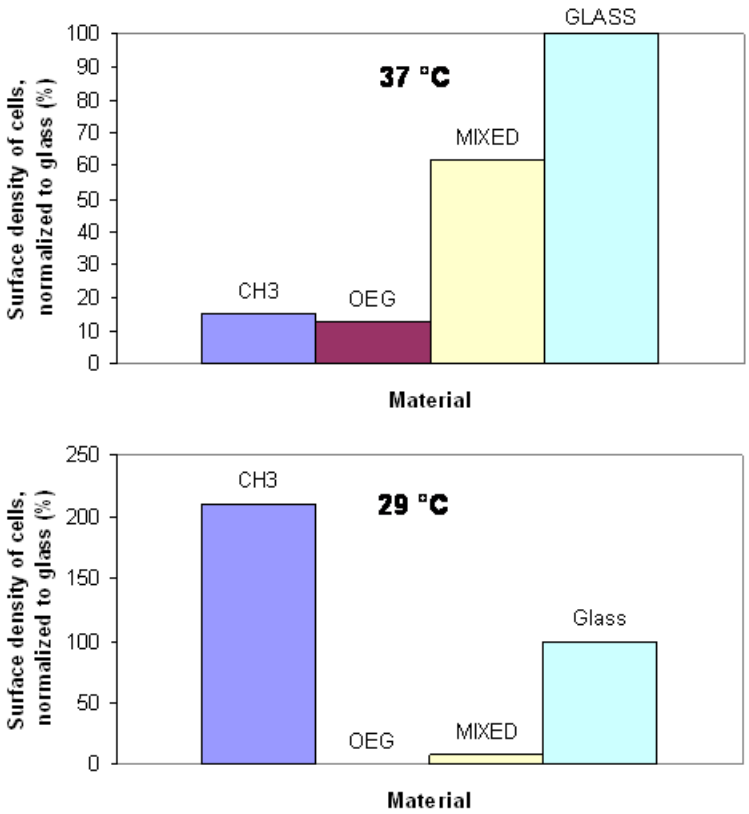


Figure 2.15: Quantification of adhered fibroblasts grown at a temperature above, 37 °C, and below, 29 °C the change in molecular conformation to the various SAM surfaces, $C_{11}EG_6OH$ is abbrev. as OEG, $C_{11}CH_3$ abbrev. as CH3, and mixed $C_{11}CH_3/C_{11}EG_6OH$ SAM abbrev. as MIXED.

All the test surfaces were gently rinsed with 4 °C DMEM solution three times and reexamined. The glass, and $C_{11}CH_3$ showed no observable changes in cell adhesion after rinsing. The $C_{11}EG_6OH$ surface had a small quantity of weakly adhered fibroblasts on the surface and after rinsing showed complete removal of fibroblasts. It should be noted that perturbing fibroblasts adhered on the $C_{11}EG_6OH$ SAM would often results in their removal from the surface at any temperature. In support of our hypothesis, the mixed $C_{11}CH_3/C_{11}EG_6OH$ SAM showed cell detachment after rinsing with 4 °C DMEM solution. The entire mixed $C_{11}CH_3/C_{11}EG_6OH$ SAM surface

was imaged in a movie that showed nearly complete detachment of the fibroblasts. Nine images were extracted from that movie and concatenated for Figure 2.17. Fibroblasts that did not detach from the surface were observed to sway around a single pivot point when the surface was perturbed.

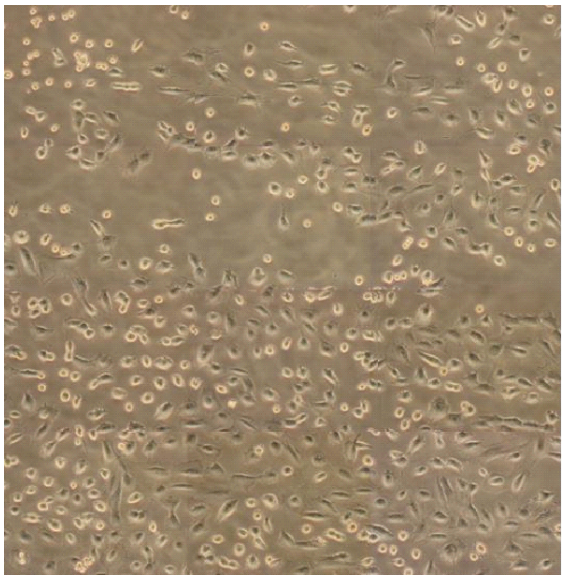


Figure 2.16: Fibroblast growth after 3 days at 37 °C in a incubator on mixed $C_{11}CH_3/C_{11}EG_6OH$ SAM prior to wash step.

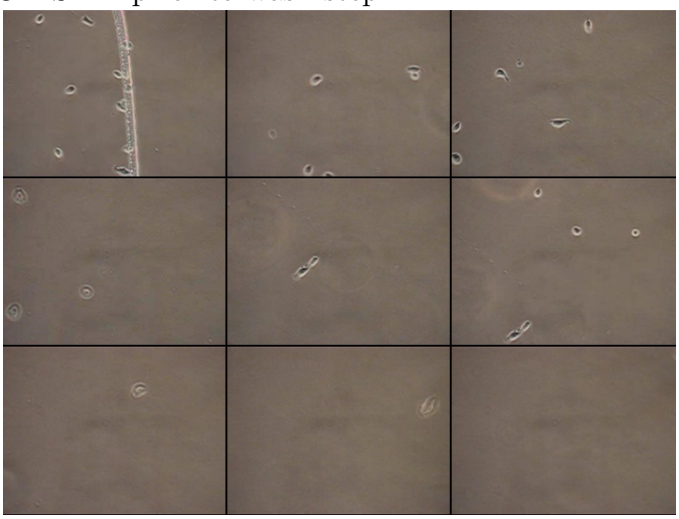


Figure 2.17: Concatentation of nine images taken from a movie examining the entire mixed $C_{11}CH_3/C_{11}EG_6OH$ SAM after three gentle rinses with 4 °C DMEM solution. Figure 2.16 is the the surface prior to the rinsing.

XPS analysis after DMEM immersion

XPS was used to examine the chemical changes that occur in the mixed $C_{11}EG_6OH$/ $C_{11}CH_3$ SAM surface after incubation. Table 2.4 shows the surface composition after the samples were immersed in DMEM for various periods of time. Sample 1 was scanned three times in different locations on the surface. It had been immersed in DMEM solution at 37 °C for 1 day. The gold, sulfur, carbon and oxygen are present in the thiolate. Importantly, any protein adsorbed to the surface would show in the nitrogen scan. As can be seen there is very little nitrogen on the SAM, implying the mixed SAM does not absorb protein from the DMEM solution. Sample 2 was kept in DMEM at 37 °C for 2 days. Again is it important to note that there is very little nitrogen in the elemental composition, implying no protein adhesion to the mixed SAM surface. The same is true for sample 3 which was kept in DMEM for 3 days at 37 °C. It should also be noted the decrease in the oxygen ratio. It is believed that the OEG molecule first degrades in the ethylene glycol chemistry prior to oxidation of the sulfur-gold bond. The mechanism of degredation has not yet been elucidated. The decrease in the oxygen ratio from the first sample, 16, to mid 13 means the oxygen within the ethylene glycol is rearranging and or possibly leaving in the form of water. The six segments of the ethylene glycol are slowly reacting, and changing the chemistry of the molecule and SAM surface properties.

Low resolution XPS scans after the DMEM immersion, not shown, show the characteristic peaks for the mixed SAMs. The sulfur, carbon, and oxygen bonds are seen at 164, 285, and 531 eV respectively. The high resolution C 1s spectra for the mixed SAM surface after 1,2, and 3 days post-immersion in DMEM at 37 °C is shown in Figure 2.18.

High resolution C 1s XPS spectra of the mixed SAM surface are shown in Figure 2.18 for 1, 2, and 3 days post-immersion in DMEM at 37 °C. There is a decrease in the peak intensity for C-H and C-O photoelectrons. This is implying a loss of

Table 2.4: Chemical composition ,%, of the mixed SAMs after immersion in DMEM for 1, 2 and 3 days.

Day	Au 4f	C 1s	O 1s	N 1s	S 2p
1^{st} scan 1	24.3	53.0	16.9	1.9	4.0
1^{st} scan 2	25.5	53.0	15.8	0.0	5.7
1^{st} scan 3	25.6	54.4	15.3	0.8	3.9
Average	25.1	53.5	16.0	0.9	4.5
std. dev	0.7	0.8	0.8	0.9	1.0
2^{nd} scan 1	29.7	50.3	13.2	0.0	6.8
2^{nd} scan 2	32.6	46.7	14.3	0.0	6.5
2^{nd} scan 3	30.6	50.1	13.4	0.0	6.0
Average	31.0	49.0	13.6	0.0	6.4
std. dev	1.5	2.0	0.6	0.0	0.4
3^{rd} scan 1	34.3	45.3	16.2	0.0	4.3
3^{rd} scan 2	35.4	47.5	12.4	0.6	4.1
3^{rd} scan 3	32.6	45.6	14.3	2.4	5.1
Average	34.1	46.1	14.3	1.0	4.5
std. dev	1.4	1.2	1.9	1.2	0.5

thiolates from the gold surface. Interestly, there is a small carboxyl photoelectron peak present on gold surface. Neither component SAM of the mixed SAM contains carboxyl carbons it may be the ether carbons present in $C_{11}EG_6OH$ are reacting to become this source of carboxyl photoelectrons. The composition of the SAM surface from the high resolution C 1s spectra can be seen in Table 2.5.

High resolution O 1s XPS spectra of the mixed SAM surfaces are shown in Figure 2.19 for 1, 2, and 3 days post-immersion in DMEM at 37 °C. The area of the O 1s

Table 2.5: High Resolution C1s composition from XPS spectra removal from DMEM for various times, n=3, standard deviations are less than 2%

Day in DMEM	C-H %	C-O %	O-C=O
1	55.2	38.7	6.1
2	51.5	30.7	3.1
3	36.8	27.6	5.9

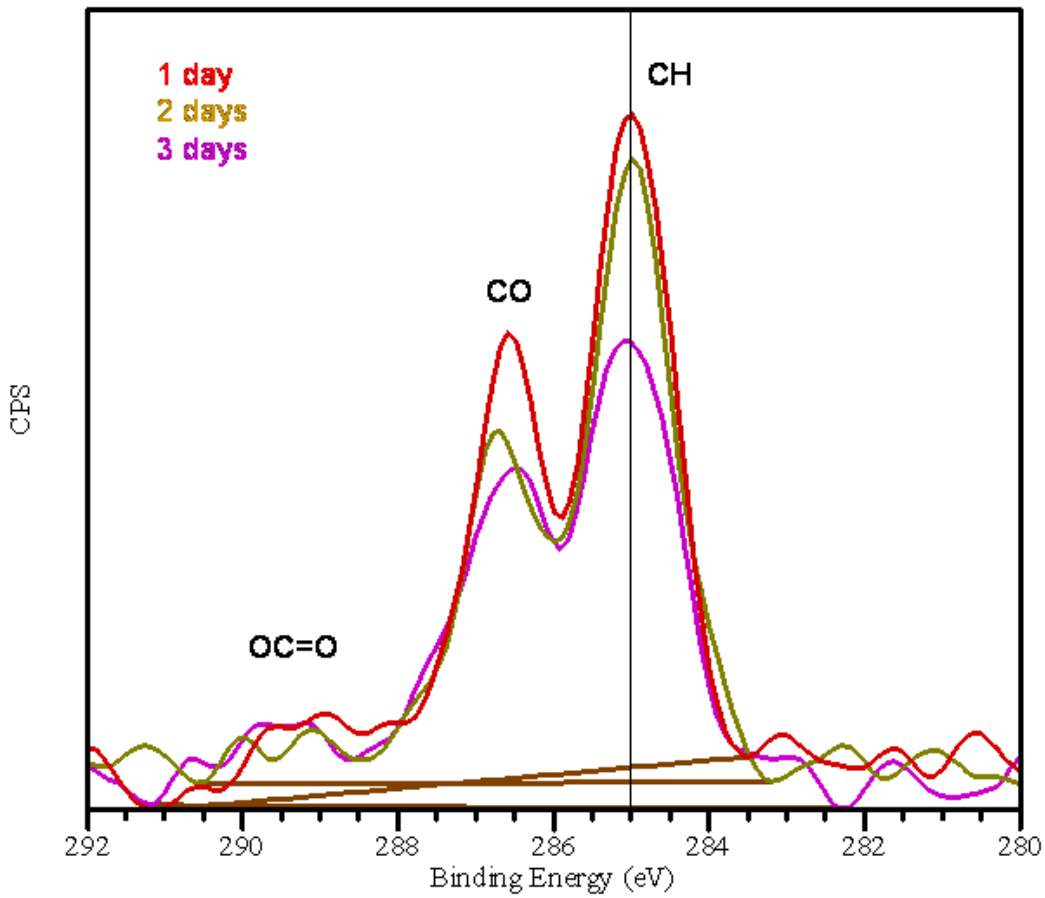


Figure 2.18: High resolution XPS scans of the carbon 1s mixed SAM surface after immersion in DMEM for 1,2, and 3 days at 37 °C.

peak is decreasing with increased immersion time in DMEM, indicating a change in the amount of oxygen present on the gold surface. The peak at 545 eV is from the Au 4p electrons, which is increasing slightly with DMEM immersion time. The increased signal from gold electrons comes from the decrease in photoelectron scattering from the SAM, thus there is a loss thiolates from the gold surface. Sulfate electrons would be seen around 532 eV. The sulfate peak is close enough to the oxygen peak, within 1 eV, that it may not be separately detectable.

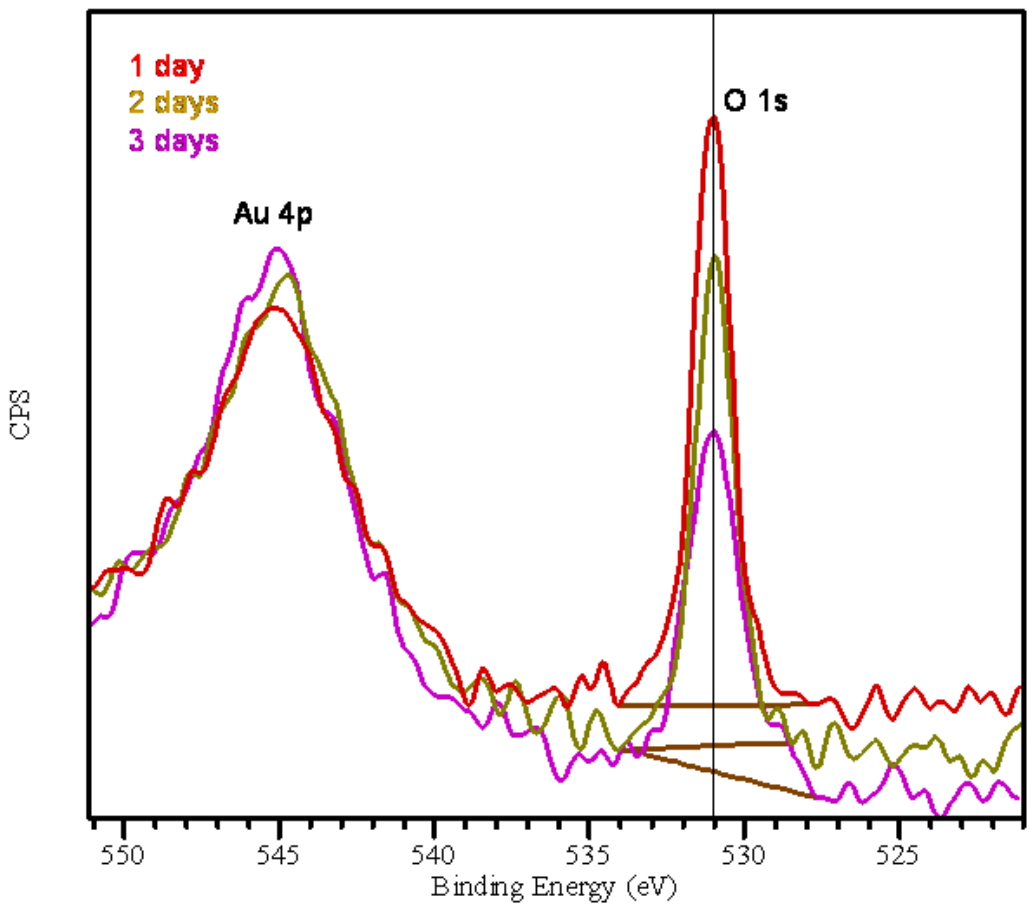


Figure 2.19: High resolution XPS scans of the oxygen 1s mixed SAM surface after immersion in DMEM for 1, 2, and 3 days at 37 °C.

2.3.4 Degradation of the mixed $C_{11}EG_6OH/C_{11}CH_3$ SAM

$C_{11}EG_6OH$ thiol is a very environmentally sensitive molecule. $C_{11}EG_6OH$ is sensitive to oxygen. Prochimia, a thiol manufacturer, suggests that you do not keep a $C_{11}EG_6OH$ thiol solution for more than 2 weeks before making a fresh solution [44]. During the third step ambient air was still in the rotovap when extracting the solvent from the $C_{11}EG_6OH$ product. The heat (40 °C) and oxygen during the solvent extraction (30 minutes) changed the $C_{11}EG_6OH$ product from 10% disulfide to 80%

disulfide as measured by mass spectroscopy before and after solvent extraction. The disulfides are produced when the two thiol molecules react with the loss of hydrogen gas.

It was very difficult to create a mixed SAM containing a 1:1 surface loading using the $C_{11}EG_6OH$ containing 80% disulfide. Very high volume fractions of $C_{11}EG_6OH$ were used, although XPS and ellipsometric thickness showed that the surface mole fraction varied greatly from sample to sample. The mixed SAM surfaces created with the 80% disulfide did not show and change in contact angle with change in temperature. The failure to obtain a change in contact angle and non-reproducable surface loading was attributed to the percentage of disulfide in the $C_{11}EG_6OH$ batch. To correct this the disulfide bond was reduced from 80% to about 30% in an additional step shown in Figure 2.4.

The reduced $C_{11}EG_6OH$ containing 30% disulfide was used generate Figure 2.20, which shows the change in contact angle with temperature. The change in contact angle is not seen until lower concentrations of $C_{11}EG_6OH$ volume fraction. The contact angle change is also not as large as mixed SAM created from commercially obtained $C_{11}EG_6OH$.

There is a small range in surface mole fraction of mixed SAM where it is thermally responsive [2]. In Figure 2.2 it is evident that proteins will adsorb below a $C_{11}EG_6OH$ surface mole fraction of 0.4 while not adsorbing at a surface mole fraction above 0.6. Difficultly in reproducing this data may be attributed to shifting of the $C_{11}EG_6OH$ surface mole fraction. It is believed that the EG_6OH molecule in the mixed SAM surface is degrading due to oxidation shifting the surface mole fraction to the region of non-thermal response allowing protein and cell adhesion. It is known that molecules of PEO in solution are susceptible to oxidation [45, 30]. After eight days in growth medium, the $C_{11}EG_6OH$ SAM has degraded enough to allow for fibroblast growth while other SAMs continued to prevent fibroblast growth,

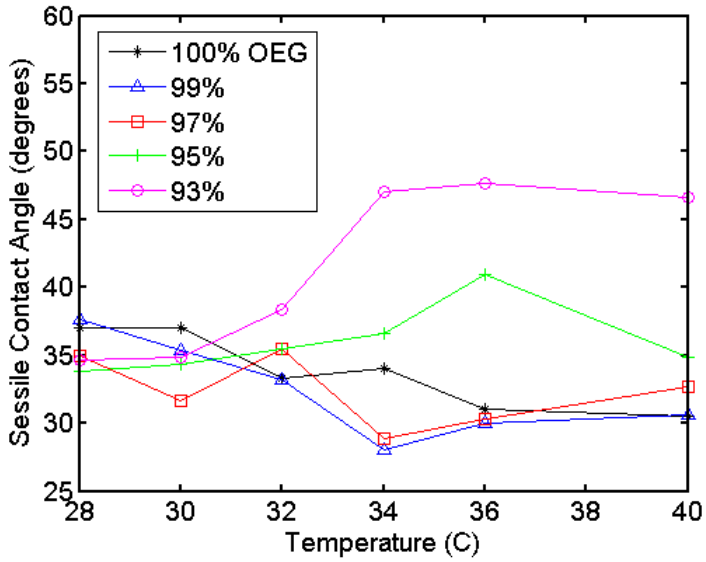


Figure 2.20: Thermal responsiveness observed by contact angle for synthesized $C_{11}EG_6OH$ mixed with $C_{11}CH_3$.

see Figure 2.21. Using XPS, mass spectrometry (MS), and FTIR, Valiokas et al. determined that the $C_{11}EG_6OH$ SAM first degrades by loss of the oligomer section and then detachment of the alkylthiolate [46]. While other SAMs are less susceptible to oxidation and degradation, only the mixed $C_{11}EG_6OH$/ $C_{11}CH_3$ SAM is thermally responsive.

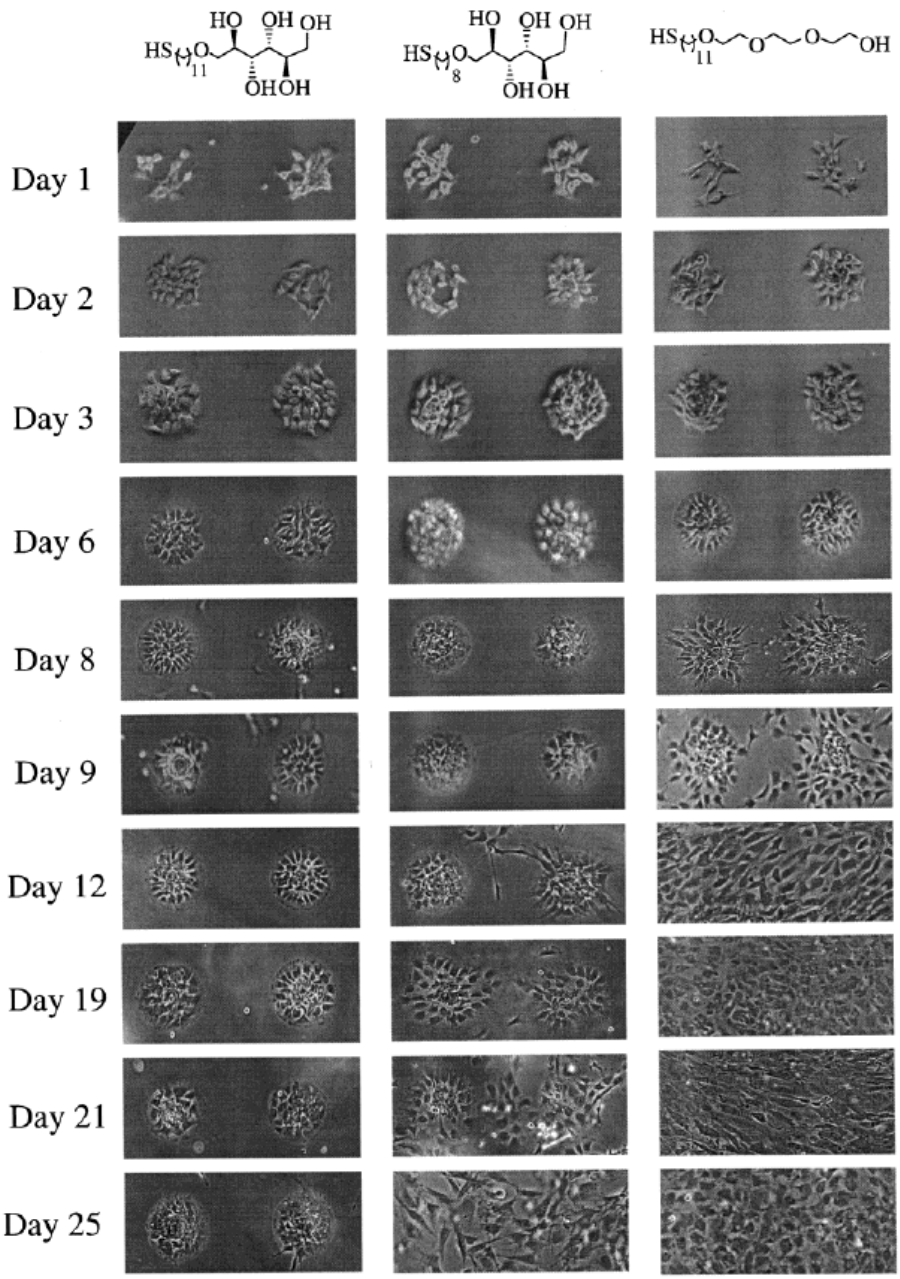


Figure 2.21: Images of rat fibroblasts on various SAM surfaces. The rat fibroblasts growing outside the initial non-SAM circles on each surface show how the passivated areas degrade with time, tri(ethylene gylcol) is the right most image set. Image taken from Luk et al. [4]

The age of the $C_{11}EG_6OH$ thiol also matters. It was discovered that 1 year old $C_{11}EG_6OH$ was a waxy yellowish-white solid. The $C_{11}EG_6OH$ had been stored at room temperature in argon during its non-usage. Its NMR and MS spectra confirmed that it was $C_{11}EG_6OH$. This $C_{11}EG_6OH$ created a SAM and had contact angles consistent with literature. Yet, it was not thermally responsive when mixed with $C_{11}CH_3$ at any surface coverage ratio and any temperature tested.

Another factor is the age of the SAM. Mixed $C_{11}EG_6OH/C_{11}CH_3$ SAMs would show a larger change in contact angle the sooner they were tested after removal from the solution of creation. If the SAMs were dried and kept in nitrogen container for an a week or more they would exhibit a smaller change in contact angle change with temperature or show none at all. We believe the the thiol molecules on the the surface of the gold would start to phase separate. It is known that the upper most layer of gold atoms is mobile allowing for diffusion of thiolate molecules within the SAM [47]. It has also been shown that SAMs can phase separate [48]. The thiolates would have a driving entropic force to phase separate creating islands of $C_{11}EG_6OH$ and $C_{11}CH_3$ molecules. This hypothesis was never confirmed spectroscopically but in experiments with rat fibroblasts the cells had preference to specific areas. This observation tended to support the phase separation hypothesis. The phase separation hypothesis can be verified by examining changes in the mixed SAM with tunneling force microscopy with time.

The underlying surface roughness may also affect the molecular transition of $C_{11}EG_6OH$. Microscope slides are fairly rough by their nature of manufacture, while coverslips were assured to us to be much smoother. It was discovered that thermally responsive $C_{11}EG_6OH/C_{11}CH_3$ SAMs on coverslips would show a larger change in contact angle than that on microscope slides.

The amount of gold deposited onto a surface also may effect in the arrangement and molecular transition of the $C_{11}EG_6OH/C_{11}CH_3$ SAM. AFM measurements show

that evaporated gold will give a "rolling hills" topography to the surface. The average roughness, from AFM scans, for a 15 nm surface is 4.4 $\mathring{A}$. 25 nm gold has a average roughness of 6.7 $\mathring{A}$. 60 nm gold has a average roughness of 16.5 $\mathring{A}$. This hypothesis was never tested but was believed to be a factor in thermal response.

Observations of the thermal response of the mixed $C_{11}EG_6OH/C_{11}CH_3$ SAMs were made at seven minute intervals. The microscope slides or coverslips were placed on the goniometer stage and allowed to thermally equilibrate for the seven minutes. The selection of seven minutes was arbitrary and was believed to be enough time for thermal equilibrium to be obtained by the samples. The seven minutes is not necessarily the time for the mixed $C_{11}EG_6OH/C_{11}CH_3$ SAM to exhibit the thermal response. At the elevated temperatures, when the water drop is evaporating, the contact angle should be obtained quickly to avoid observing the receding contact angle. It was seen by myself, Xinyu Cao, Linnea Ista, and the researchers the University of Gotenberg, Sweden that the thermal responsive contact angle was more a gradual change over a 10 °C temperature range than the very sharp transition temperature published [3].

Volume fractions of the $C_{11}EG_6OH$ thiol solution and $C_{11}CH_3$ solution should be 95:5. This ratio of solution gives a surface loading of each thiol of about 50:50 as confirmed by XPS oxygen ratios and ellipsometric thickness. The thermally responsive nature of $C_{11}EG_6OH$ can be observed beyond this range from about 97.5% to 93% and possible lower volume fractions as seen in Figure 2.8. There appears to be a small window in which the kinetic rates of thiol attachment to the gold surface will give a equal surface loading of both thiolates. The $C_{11}EG_6OH$ molecule has a higher solubility in ethanol than the $C_{11}CH_3$ giving a slower rate of adsorption and thus requiring a higher concentration. In the self-synthesized $C_{11}EG_6OH$ there existed more contaminants and disulfide $C_{11}EG_6OH$ than the commercially obtained $C_{11}EG_6OH$ so the thermal responsive change in contact angle was not as large and sometimes

not present in similar volume fractions as seen in Figure 2.20. The cyclic nature of the thermal responsiveness can be seen in Figure 2.9. The change in contact angle appears to be decreasing with each thermal cycling. An interesting experiment not performed, would be to see how many cycles the mixed $C_{11}EG_6OH/C_{11}CH_3$ SAM would exhibit before the thermal responsive nature is no longer observed. We hypothesize that chemical changes are occuring in the $C_{11}EG_6OH$ molecule, similar to those seen in Figures 2.18 through 2.19, that will eventually lead to loss of thermal response.

It was hypothesized that changing the length of the alkyl backbone of the $C_{11}CH_3$ molecule in the mixed SAM would change the thermal responsive property. Dodecane thiol was changed to decane thiol (C-10) and also undecane thiol (C-11). No change was observed in the thermal responsive nature of the mixed SAMs at similar volume ratios. Contact angles along with the change in contact angles were the same as those in the $C_{11}CH_3$ mixed SAMs.

It was hypothesized that changing the $C_{11}CH_3$ molecule to a molecule of larger radial size would change the thermal responsive property. When benzene thiol was mixed with $C_{11}EG_6OH$ the contact angle varied from 30 degrees (pure $C_{11}EG_6OH$) to 65 degrees (pure benzene thiol). There was no thermal responsive behavior in any of the volume fractions tested.

2.4 Conclusion

The gold coated slides were characterized by AFM to show an increasingly rough surface as the gold thickness increased. After deposition of the thiols on the gold, the resulting SAMs were characterized by ellipsometry and contact angle goniometry, and show evidence of SAM formation. Two methods were given to calculate the surface fraction of the $C_{11}EG_6OH$ molecule present in the mixed $C_{11}EG_6OH/C_{11}CH_3$ SAM.

The mixed $C_{11}EG_6OH/C_{11}CH_3$ SAMs were confirmed as reversibly thermally responsive surfaces. The factors that made for a thermally responsive surface were also discussed along with degredation of the SAM surfaces. How the mixed $C_{11}EG_6OH/C_{11}CH_3$ SAM surface affect rat fibroblast growth was also qualitatively and quantitatively shown. Lastly, the mixed SAM surfaces were characterized by XPS after exposure to experimental conditions.

Chapter 3

Use of Atomic Force Microscopy in Quantification of Bioadhesion on Thermally Responsive Mixed Self-Assembled Monolayers

3.1 Introduction

This chapter reports on the adhesion of model proteins to mixed hexa(ethylene glycol) thiolate ($C_{11}EG_6OH$) and dodecane thiolate ($C_{11}CH_3$) self-assembled monolayers (SAMs) above and below their molecular transition. It should be noted that the mixed $C_{11}EG_6OH/C_{11}CH_3$ SAM surface was confirmed to be thermally responsive by contact angle goniometry before any protein adhesion experiments were performed.

The Results and Discussion Section of this chapter can be loosely divided into six parts. The first part explains the choice of proteins used in my experiments. The second part examines the surface topography of the mixed $C_{11}EG_6OH/C_{11}CH_3$

SAMs before the protein adhesion experiments were performed. The third part discusses the force distance curves, data processing, and observations made during experimental controls. The method used to calculate the area of interaction for an unmodified cantilever to the mixed $C_{11}EG_6OH/C_{11}CH_3$ SAMs is described in the fourth part. The fifth part shows the protein adhesion data of the model proteins to the mixed SAM in the form of adhesion force histograms and sequencial adhesion force data. The sixth part concludes with an analysis and comparison of the data obtained with relevant data from literature.

Protein adsorption is a critical initial event when a foreign body comes into contact with a living fluid such as blood [49, 50]. To understand bioadhesion the study of protein adsorption to surfaces is critical. A good review of protein adsorption at a solid-liquid interface is given by Malmsten [49]. A more detailed review of the factors that influence protein adhesion is also presented by Malmsten [51]. Because there are so many factors involved in protein adsorption, a model to predict adsorption is quite complex and statistical in nature [50]. Researchers do not agree about what characteristic inherent in a protein or a surface determines protein adhesion. It is believed that most important factors in protein adhesion are: surface free energy [52], surface wettability [53], different functional endgroups [54], residence time [55], loading force [55], buffer medium [56], electrostatic effects [56], and pH [55].

Intermolecular forces can be classified into three loose categories, including: covalent or chemical bonding forces, electrostatic forces or Coulumb forces, and polarization forces. While covalent forces are necessary for chemical bonding, covalent forces are not as relevant in protein adsorption as electrostatic and polarization forces, and will not be discussed in this chapter. An electrostatic force originating from a molecules' charge creates a permanent dipole within the molecule, which leads to further fractionation of the dipole charge. Polarization forces arise from dipole moments, which are induced by electric fields, nearby charges or permanent dipoles.

Polarization is particularly important for protein adhesion because all intermolecular interactions in a solvent medium involve polarization forces.

The van der Waals forces are a grouping of attractive and repulsive forces arising from polarization forces. The van der Waals forces are composed of three forces, including: (1) dipole-dipole forces, (2) induced dipole-induced dipole forces and (3) instantaneous induced dipole-induced dipole. Hydrogen bonding, a special case of dipole-dipole interaction, is one of the most important intermocular forces. Hydrogen bonding dictates the folding of proteins, the solubility of proteins in solution, and the wetting of surfaces. Thus, the hydrogen bond and its related hydrophobic effect are key in protein adhesion to surfaces. A favorite quote describing the hydrophobic effect is, "Water simply loves itself too much to let some substances get in the way" [57].

When considering what forces dominate protein adhesion to a thermally responsive surface, it is important to remember that the SAM surface of interest here have a hydrophobic $C_{11}CH_3$ thiolate and a hydrophilic $C_{11}EG_6OH$ thiolate. In addition, each protein examined may be charged, or not, polarized, have regions of hydrophobicity and hydrophilicity, and may exhibit all of the intermolecular forces at the same time. For these reasons, it is very difficult to extract which forces are determinative in protein adhesion.

Most protein adsorption experiments determine only if protein is present or not. For example, ellipsometry measures the thickness of an adsorbed protein thin film on a surface, thereby indicating whether adhesion has occurred. However, there are several indirect ways to quantify the bioadhesive force to a thermally responsive material. Five such methods are discussed below. One method is to use a centrifugal force device to remove adherent cells using a rotating disk in a liquid medium [58]. This device is good for obtaining the force necessary for removing cells but not applicable to protein removal. A second method for finding the force of adhesion of

cells is by using shear stress in a laminar flow fluid device [59]. Again this device is good at calculating the force necessary for removing cells, but is not applicable to proteins. A third method, surface plasmon resonance (SPR), uses a modification of a laminar flow cell and can detect protein adsorption and displacement. It was shown using a SPR device that no protein adsorbed to a mixed SAM of oligo(ethylene glycol) methyl methacrylate and $C_{11}CH_3$, although SPR provides no information on the force of protein adsorption [60]. SPR may only be used on substrates that exhibit a plasmon resonance upon light irradiation [61]. Such substrates are typically confined to metals such as gold or silver. A fourth method, quartz cyrstal microbalance (QCM), also uses a laminar flow cell and is often used to detect adsorption rates of proteins onto a crystal surface. The QCM has been used to show protein adsorption on quartz crystal modified thiolate surfaces of hydroxyl and methyl termination [62]. However, the QCM does not allow for direct measurement of the force of protein adsorption to surfaces. The force needed to remove the protein from the surface must be calculated from shear stress relationships from fluid flow rate. A fifth method used to measure protein adsorption utilizes a surface force apparatus (SFA). SFA was used to show the force of adhesion of a mussel foot protein to mica [63]. This was an impressive quantification of a very strong adhesive protein common in nature. However, SFA is not a very common instrument. The area of interaction is large in comparison to the subject of inspection, and the substrates must be very smooth half cylinders, typically mica [57]. The limitations in the methods described above, require a more readily available device to measure directly protein adhesion.

The most commonly used device to measure molecular scale force is the AFM [64, 65, 66]. AFM has been used to measure the adhesive force between two bovine serum albumin (BSA) proteins, BSA and a SAM, and BSA and a dextran modified surface [67]. Wang et al. attempted to reproduce what occurs naturally between proteins and surfaces of different chemical composition. AFM has also been used to quantify the protein adhesive force to SAMs. A large comparison of seven surface

bound proteins and their interactions with eight SAM modified AFM tips, including tri(ethylene gylcol), were examined [53]. In that study, Sethuraman et al. provided a very thorough examination of the interaction possibilities in bioadhesion. The thiolate terminal groups were intended to represent the many possible chemical surfaces for bioadhesion found in nature, while the proteins were used as models for cellular adhesion molecules. AFM has been used to measure the forces between two proteins, albumin and fibronectin, to PNIPAAm above and below the temperature required for a change in molecular conformation [68]. This was an important work because it showed that AFM can detect the force of adhesion between the protein and PNIPAAm substrate, and confirmed that the PNIPAAm substrate used was thermally responsive. Another important work showed the adhesive force between a PNIPAAm surface and BSA at steps of two degrees during the change in molecular conformation [5]. The force curve obtained can been seen in Figure 3.1. At temperatures lower than the LCST, approximately 24 °C, the adhesive force of the BSA protein to PNIPAAm is zero, but as the temperature increases, the protein exhibits an adhesive force to the PNIPAAm surface.

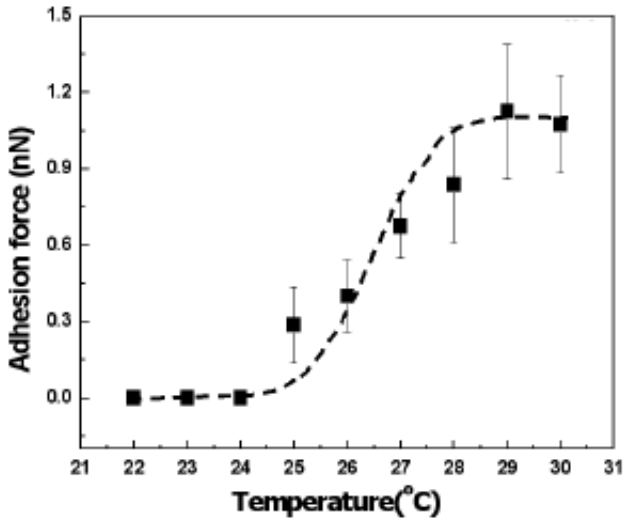


Figure 3.1: The adhesive force of a BSA coated AFM tip measured during the LCST of PNIPAAm measured by AFM, taken from Cho et al. [5]

To determine the adhesive force between the model proteins and the mixed $C_{11}EG_6OH/C_{11}CH_3$ SAM above and below the molecular transition, we used a similar method to that of Cho et al. by physically adsorbing proteins to an AFM cantilever and observing the adhesive force above and below the molecular transition to mixed $C_{11}EG_6OH/C_{11}CH_3$ SAMs. We hypothesize that using AFM the difference in adhesive force of the six proteins will be observed above and below the molecular transition to thermally responsive mixed $C_{11}EG_6OH/C_{11}CH_3$ SAMs. To our knowledge, there are no published studies on the protein adhesive forces between a mixed SAM of $C_{11}EG_6OH$ and $C_{11}CH_3$.

3.2 Materials and Methods

Materials Circular microscope coverslips, 11 mm in diameter, were obtained from VWR. Gold (99.999%) 1-3 mm spheres used in metal evaporation were acquired from

Plasmaterials. Chromium rods were purchased from Mathius Company. $C_{11}EG_6OH$ was purchased and used as receieved from Asemblon, Redmond, WA. Dodecane thiol 98%, phosphate buffered saline (PBS), collagen from bovine achilles tendon (C9879-1G), lysozyme from chicken egg white grade VI (L2879), ribonuclease A from bovine pancreas (R6513-10MG), pyruvate kinase from rabbit muscle Type III (P9136-1KU), cholera toxin subunit B were purchased from Sigma-Aldrich Chemicals.

The gold coated circular microscope coverslips were prepared as described in chapter 2. Mixed SAMs of $C_{11}EG_6OH/C_{11}CH_3$ were created as described in chapter 2.

Protein solutions were created at 1 mg/mL in PBS buffer 1x pH 7.4 and passed through a 0.2 micron syringe filter, stored at 4 °C, and degassed in low vacuum for a minimum of 30 minutes prior to usage. Buffer solutions were degassed by exposure to low vacuum for a minimum of two hours.

Characterization Ellipsometry was done with an M-44 ellipsometer from J.A. Woolam Co. The thickness of the SAM layer was measured at least 3 times and the average taken. Sessile drop water contact angles were taken with a Rame-Hart contact angle goniometer. The temperature was controlled with a heating ribbon and monitored by a thermocouple.

Silicon nitride AFM cantilevers (MSCT-UNM nominal tip radius 10 nm) were purchased from Veeco Probes. Force measurements were carried out with a Veeco Nanoscope IIIa Atomic Force Microscope on SAM prepared circular gold coated coverslips in a standard fluid cell filled with 1x phosphate buffered saline (PBS). Tip movements and data collection were collected with Veeco program version 6.1. Protein was physically adsorbed onto the AFM cantilever by placing a drop of 1 mg/mL protein solution on the cantilever for 15 minutes. An O-ring and fluid cell containing the AFM cantilever was then set on top of the sample. Degassed PBS was

Table 3.1: List of proteins and properties used the adhesion to mixed SAM experiment.

	Bovine serum albumin	Collagen	Pyruvate kinase	Cholera toxin subunit B	Ribonuclease A	Lysozyme
PI	4.7	8.3	6.3	6.6	7.8	11
Mw	66.4K	300K	237K	12K	14K	14.5K
Charge at pH 7.4	+	-	+	+	0	-
Protein Behavior*	"Soft"	"Soft"	"Soft"	"Hard"	"Hard"	"Hard"

* see text

injected into the fluid cell and the film was allowed to equilibrate with the medium for 10 minutes. The force sensitivity was updated for each cantilever prior to data collection. Tip-sample force was calculated using a spring constant of the cantilever of 0.02 N/m as provided by the manufacturer. Force-distance curves collected at room temperature (22 °C) were performed in ambient conditions. Force-distance curves at 39 °C were performed in a plexiglass container with heat lamps connected to variable voltage and monitored with a thermocouple placed near the fluid cell. Force-distance curves were performed at 0.1 Hz scan rate, and 0.5 nN depression force. The x and y coordinates were moved 50 nm for each force-distance curve.

3.3 Results and Discussion

The model proteins used in this experiment are listed in Table 3.3. They were chosen because they are the standard proteins used in many adsorption to studies [3, 2, 32, 54, 53, 67, 69]. The proteins have positive, negative, and neutral charges at the experimental pH of 7.4. They have different sizes, shapes, and behaviors. Proteins displaying large conformational changes on adsorption can be referred to as 'soft' [49, 51]. Proteins undergoing limited or no conformational changes upon adsorption are referred to as 'hard' [49, 51]. The structures of the proteins used along with their dimensions are presented in the Appendix. The amino acid composition

of each protein is also provided in the appendix of this work.

The water contact angles of mixed $C_{11}EG_6OH/C_{11}CH_3$ SAMs were measured at different temperatures. Static water contact angles at 22 °C were 32 ± 4°, while contact angles at 40 °C were 52 ± 6°. The change in contact angle verifies that the mixed $C_{11}EG_6OH/C_{11}CH_3$ SAM has thermally responsive properties.

The mixed $C_{11}EG_6OH/C_{11}CH_3$ SAM surface was imaged by AFM to confirm that the topography had not changed when switching to the circular glass coverslip. Figure 3.2 shows the mixed $C_{11}EG_6OH/C_{11}CH_3$ SAM surface. The mixed $C_{11}EG_6OH/C_{11}CH_3$ SAM surface is very similar to the mixed $C_{11}EG_6OH/C_{11}CH_3$ surface characterized in chapter 2; the roughness and topography are nearly identical. The rolling hills topography of the gold is again observed. Although great care was taken to keep the sample free of contamination the larger and higher islands are likely dust particles. The exact composition of the larger islands is not known. The SAM surface was reconstructed into a 3D-topography map in Figure 3.3. Again the rolling hills can be seen with an occasional dust particle on the surface.

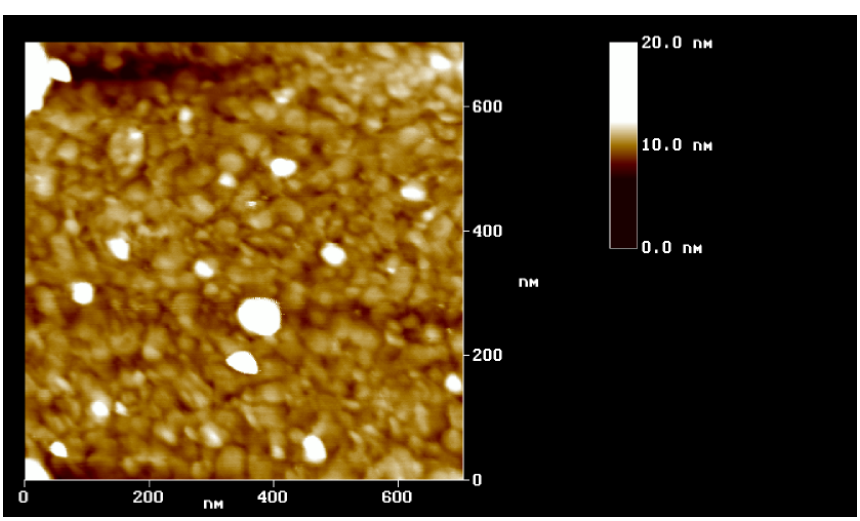


Figure 3.2: AFM micrograph of a mixed SAM surface on the gold coated circular coverslip, taken in air.

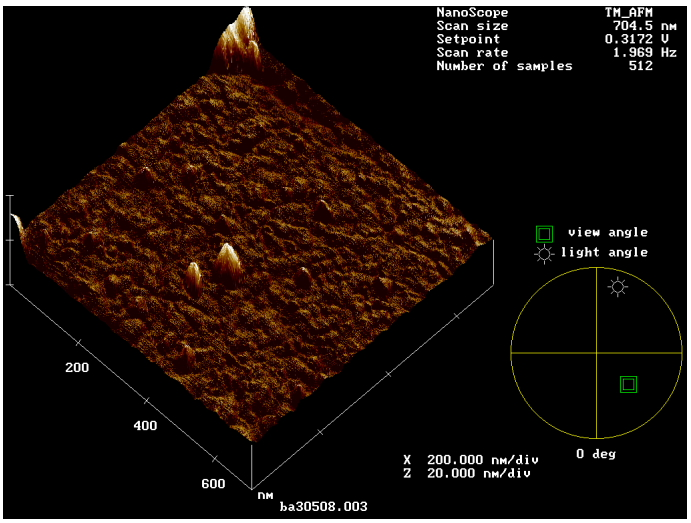


Figure 3.3: 3D reconstruction of a mixed $C_{11}EG_6OH/C_{11}CH_3$ SAM surface on a gold coated circular coverslip.

In order to ensure adhesion and other phenomena are not observed as noise, a force curve from a bare AFM tip into a hard glass surface was recorded, shown in Figure 3.4. A straight line was fit to the data that yielded a standard deviation of 5 pN. Any measurement above 5 pN has a realistic force interaction between the cantilever and surface. The same experiment was performed at 39 °C, which confirmed that the noise was about 5 pN. At 39 °C, AFM signal noise can increase because of laser drift off the detector. The drift arises from the temperature changing the index of refraction in several positions: the fluid cell, the fluid within the cell, air between sample, and detector. Care was taken to keep the noise about 5 pN at 39 °C by adjustment of the detector position.

A typical force-distance curve for an AFM tip with an adsorbed protein (BSA) without adhesion is shown in Figure 3.5. This result is typical of what is observed for protein coated tips at 22 °C. Extension occurs when the cantilever is pushed into the surface via the piezo electric drive motor. Retraction occurs when the sample is moved away from the cantilever and returned to its starting position.

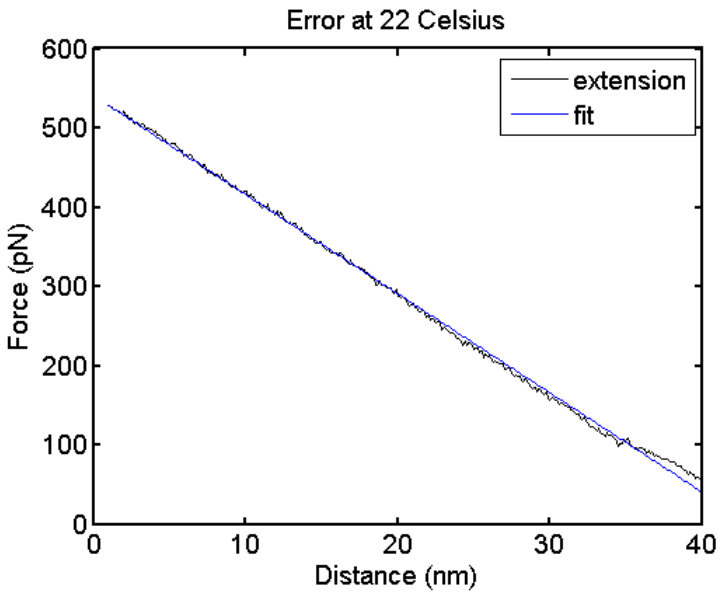


Figure 3.4: Force-distance curve of a bare AFM tip into a hard glass surface at 22 °C, standard deviation is 5 pN.

The AFM recorded cantilever deflection as a function of an arbitrary position. The software calculated the force via the spring constant of the AFM cantilever and force sensitivity calibration. The distance scale was set to zero at the point of maximum force. The force was set to zero at large tip-sample distances. The maximum force applied in this graph was about 550 pN.

Figure 3.6 shows an interesting phenomenon of compression of the material between the AFM cantilever and glass surface. In the extension curve at about 300 pN the force drops in a step and then continues to increase after the step. It is possible that this might be the compression of the protein, although this phenomenon has been observed in data collected without protein on the cantilever. It is also possible that this compression is compression of the mixed $C_{11}EG_6OH/C_{11}CH_3$ SAM layer. The hexa (ethylene glycol) groups extending above the methyl groups might be displaced or compressed prior to the compression of the rest of the SAM layer. The decrease in force might also be from the compression of the gold layer. The

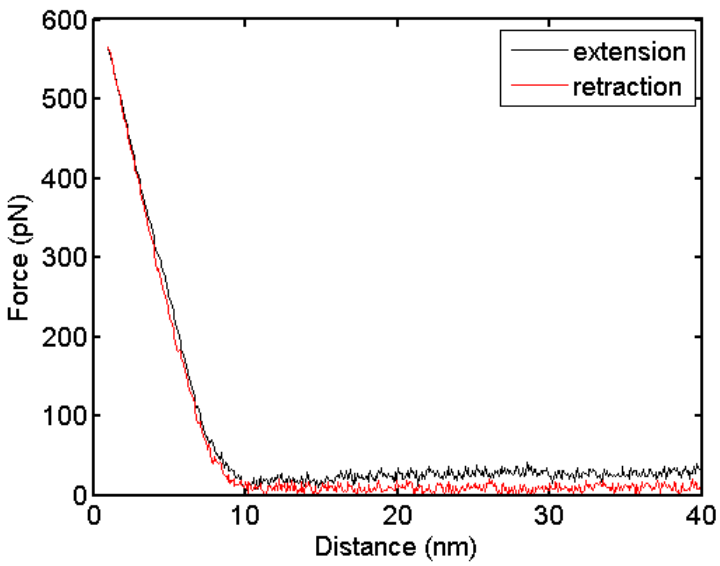


Figure 3.5: A typical force curve at 22 °C on the mixed $C_{11}EG_6OH/C_{11}CH_3$ SAM with BSA coating on the AFM cantilever.

step decrease in force indicates that it is unlikely that the gold layer was compressed because gold normally follows a linear compression.

An important factor in adhesive force is the surface area of interaction between the two opposing surfaces. The area of interaction can be both illustrated and calculated. A schematic of the surface with cantilever drawn to scale is shown in Figure 3.7. The cartoon shows that many thiolates are interacting with the cantilever. The exact number of thiolates can be calculated, using the model of Johnson-Kendall-Roberts (JKR) [70, 39]. The contact radius, a, for compliant materials (or materials of similar composition) is

$$a = \left(\frac{3\pi\gamma R^2}{K}\right)^{1/3} \tag{3.1}$$

where γ is the surface tension of the SAM, R is the radius of the AFM cantilever,

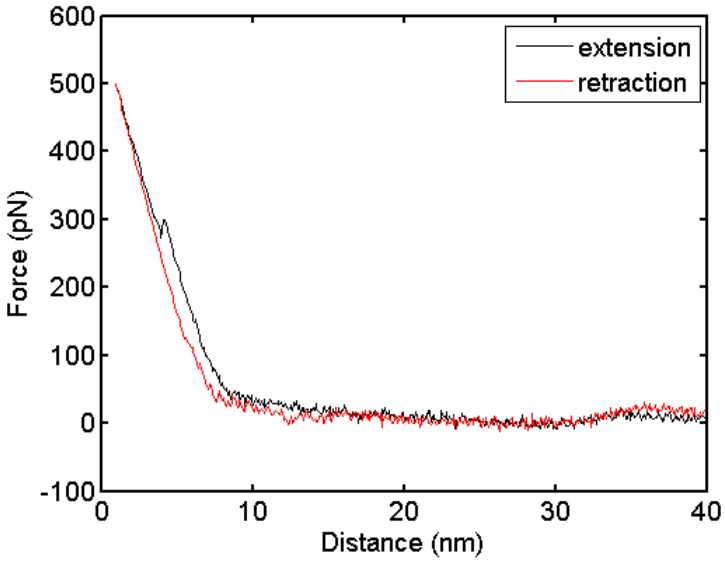


Figure 3.6: A force curve at 22 °C exhibiting a "compression" of the layer underneath the AFM cantilever ($C_{11}EG_6OH/C_{11}CH_3$ SAM with BSA on the AFM cantilever).

where K is,

$$K = \frac{2}{3}\frac{E}{1-\nu^2} \tag{3.2}$$

E is the Young's modulus of the SAM, and ν is the Poisson ratio. The Young's modulus of the SAM is essentially that of bulk gold [66, 39].

$$E_{Au-SAM} = \frac{(E_{Au}t_{Au} + E_{SAM}t_{SAM})}{t_{Au} + t_{SAM}} \approx E_{Au} \tag{3.3}$$

The Young's Modulus and Poisson ratio of Gold is 78 GPa, and 0.4498, respectively [71]. On the opposing surface the packing density per molecule on a SAM surface is 0.2 nm^2 [72, 39].

Using this calculation, we estimate that 63 thiolates interact with the bare cantilever during a force-distance curve. The force of interaction between the AFM

cantilever and SAM surface can be approximated by the sum of 63 short-range intermolecular interactions over a radius of 10 nm. It should be noted that this approximation is for a flat substrate. The values may be slightly more or less due to the 2 nm gold roughness.

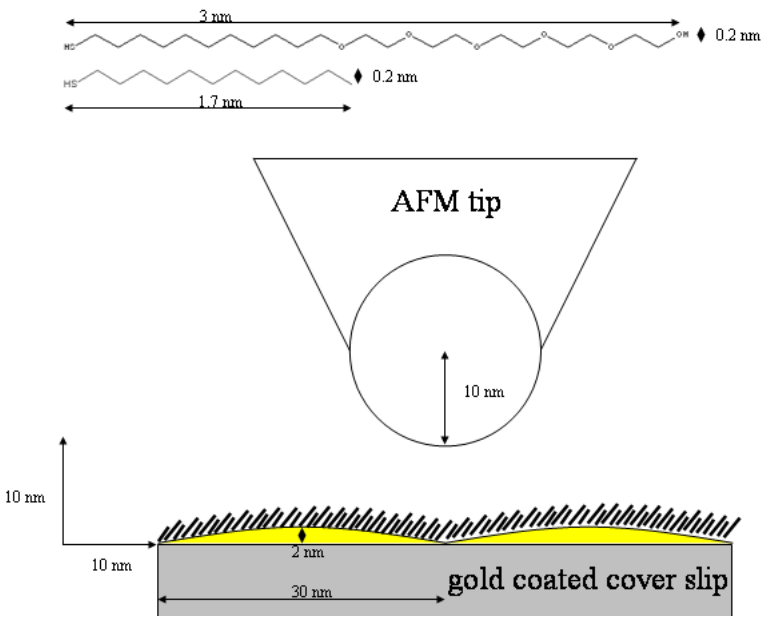


Figure 3.7: Schematic of the AFM cantilever and SAM to scale.

It is not as easy to understand how a protein modified cantilever and SAM interact. For one, it is not known how many proteins adsorb on the cantilever surface and in what conformation. It may be that the proteins absorb to the surface in their native conformation, although after the first force-distance curve this may probably no longer be the case. Denaturing of the protein on the cantilever will be discussed in more detail later in this chapter.

An example of an atypical adhesion force which are observed in a minority of measurements is shown in Figure 3.8. This is atypical because adhesion was most

often not observed at 22 °C. Of the 25 force curves performed for BSA on the mixed $C_{11}EG_6OH/C_{11}CH_3$ SAM at 22 °C, only one force-distance curve showed adhesion. There is another interesting artifact present Figure 3.8. In that Figure, the force increases from 5 nm to 20 nm, and then decreases to zero at 40 nm. This artifact is the result of the Fabre-Perot interference of the gold-coated backside of the cantilever and the gold coated surface of the coverslip. As the cantilever travels away from the surface, the laser intensity changes due to interference produced from laser light reflected off the SAM. The increase and decrease in force is only an optical effect and is disregarded in our analysis.

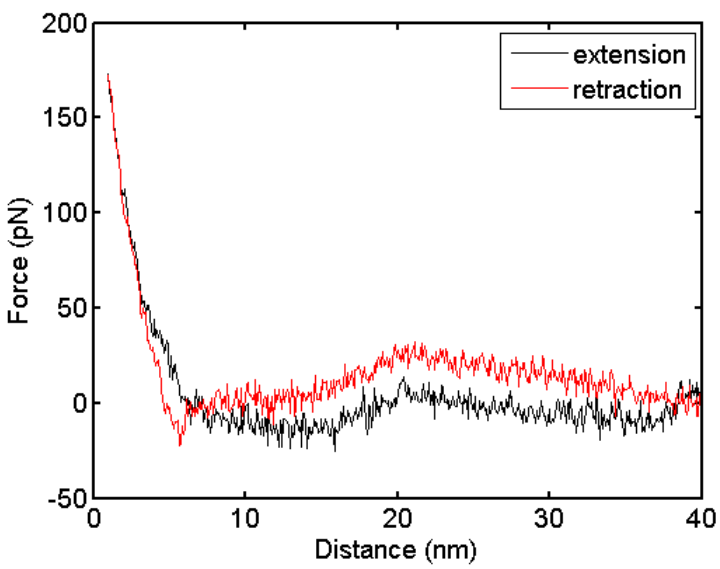


Figure 3.8: An atypical adhesion force curve at 22 °C of BSA on the mixed $C_{11}EG_6OH/C_{11}CH_3$ SAM with BSA coating on the AFM cantilever.

Figure 3.9 shows the typical force distance curve for adhesion of BSA to the mixed $C_{11}EG_6OH/C_{11}CH_3$ SAM at 39 °C. Thermal drift of the surface away from the AFM cantilever is why the extension curve start and retraction curve end do not match up. Even though the AFM was placed in a temperature controlled environment to minimize thermal drift effects, thermal drift was still present.

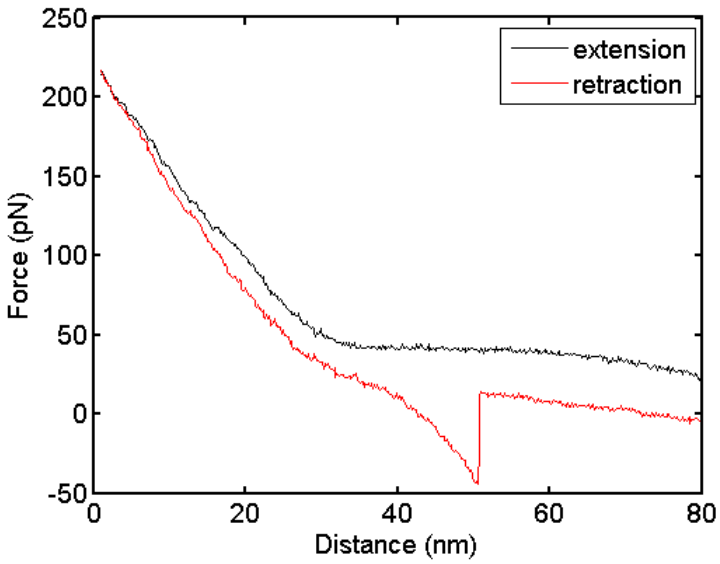


Figure 3.9: A typical force distance curve showing the adhesion of BSA to the mixed $C_{11}EG_6OH/C_{11}CH_3$ SAM at 39 °C

The force-distance curve in Figure 3.5 is very similar in nature to the force-distance curve between fibrinogen on an all helical $C_{11}EG_3Me$ SAM formed on gold shown in Figure 3.10 a) [6]. The two curves are similar in that they both do not exhibit any van der Waals attractive force upon approach and there is also no adhesion to the surface upon retraction. This is in contrast to Figure 3.10 b) which contains the all trans conformation of $C_{11}EG_3Me$ which exhibits both van der Waals attractive forces upon approach and adhesion between protein and SAM surface upon retraction. Yet, Figure 3.9 and Figure 3.10 b) support of the evidence that above the molecular transition temperature the $C_{11}EG_6OH$ within the mixed SAM is displaying a more all trans conformation behavior. It is not known exactly why some force-distance curves have a single adhesion release, such as Figure 3.5, and why others have multiple release events, Figure 3.10 b. The lack of information about the number of proteins on the AFM cantilever, the protein conformation, AFM tip shape, and substrate surface features make interpretation of the force-distance curves

difficult. It may be that the protien releases from the surface only to interact with other proteins. These interactions would have a different adhesive force at longer distances. It is also possible that the proteins are denaturing during compression and as the proteins unravel present different adhesive forces between AFM cantilever and substrate.

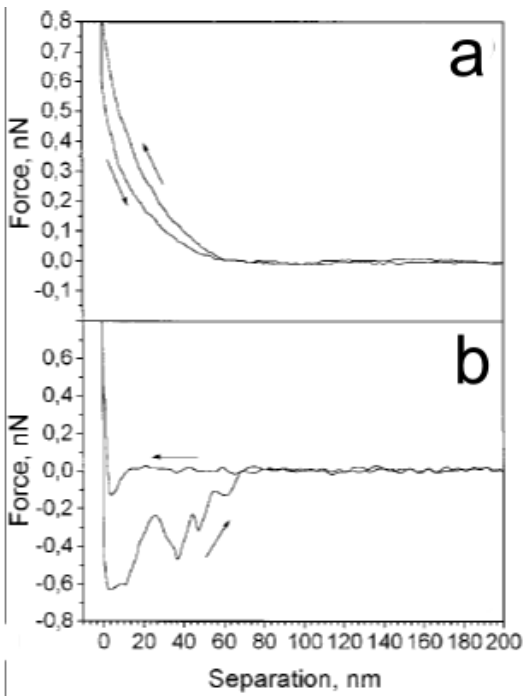


Figure 3.10: Force-distance curves between fibrinogen and the $C_{11}EG_3Me$ SAM on gold (a) and silver (b). The $C_{11}EG_3Me$ molecule displays the helical conformation on the gold surface, while displaying the all trans conformation on the silver surface. Force-distance curves were performed in the temperature range of 27 to 30 °C. Image taken from [6].

Figure 3.11 shows the double adhesion of collagen to the mixed $C_{11}EG_6OH/C_{11}CH_3$ SAM. The adhesion force was measured as the total force of the two adhesion steps. This is evidence that the proteins might be denaturing from the force-distance curves. At the start of the cantilever retraction the protein adheres to both surface and cantilever. As the cantilever retracts the protein stays attracted to both surfaces keeping

the cantilever at the same distance, this gives rise to the first attractive force. When the protein unravels, it releases the cantilever, showing the first step decrease in force. As the cantilever continues to travel away from the surface, the protein continues to unravel presenting a constant force on the cantilever. As the protein reaches an unraveling maximum, it releases from either the cantilever or the surface giving the last step decrease in force. Also seen in this figure is a small offset in zero value of force. The offset is due to thermal drift of the surface away from the cantilever during the force-distance curve. This double adhesion or possible denaturing of the protein was also seen for all the other proteins used in this experiment. Double adhesions tended to be the most prevalent yet multi-adhesion retractions where also observed.

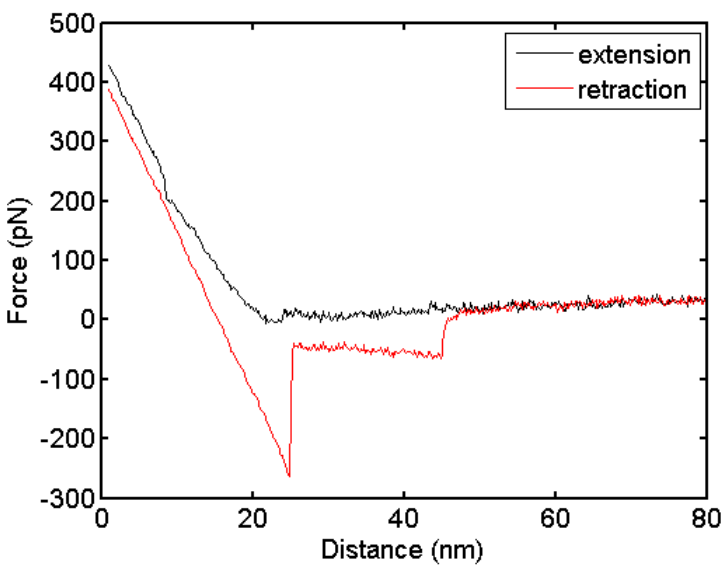


Figure 3.11: Plot of the double adhesion, or denaturing, of collagen to the mixed $C_{11}EG_6OH/C_{11}CH_3$ SAM at 39 °C

In order to verify the change in protein adhesion on the thermally responsive mixed $C_{11}EG_6OH/C_{11}CH_3$ SAMs is not a characteristic of either individual SAM, a series of controls were performed. The adhesive force between the pure component SAMs was examined at both 22 °C and 39 °C. The adhesive force is defined as the

lowest value of the force before cantilever snap-back. For each protein, 15 to 20 force curves were obtained on a single sample. This quantity was chosen because of observed protein loss from the tip (at high temperatures) around the 20^{th} force-distance curve. The data is reported in histograms of adhesive force between the SAM and protein adsorbed cantilever. The controls for the experiment can be seen in Figure 3.12. Figure 3.12 a) is the adhesive force histogram to the pure component $C_{11}EG_6OH$ SAM at 22 °C, b) is the adhesive force histogram to the pure component $C_{11}EG_6OH$ SAM at 39 °C. This figure shows that, in the majority of cases no adhesion between the BSA protein and the $C_{11}EG_6OH$ surface was observed. This is consistent with published findings that the $C_{11}EG_6OH$ SAM passivates the surface to protein adhesion [2]. In Figure 3.12 d) the pure component $C_{11}CH_3$ SAM shows a number of adhesions with $\sim$ 20 pN in magnitude. There is a tail to the histogram with adhesion forces up to 200 pN, which may be due to the denatured protein interacting with the hydrophobic surface. The same trend is seen in Figure 3.12 d) when the temperature is raised to 39 °C and BSA adheres to the $C_{11}CH_3$ SAM. It should be noted that neither pure component SAMs showed significant change in protein adhesion at the two temperatures.

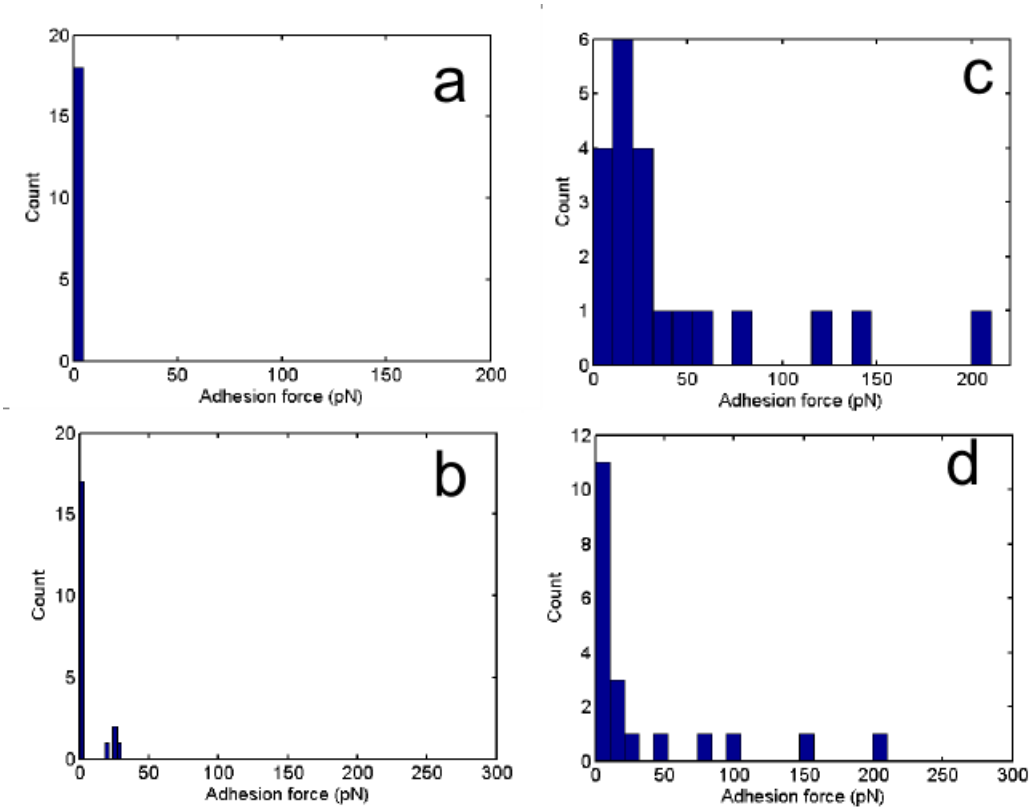


Figure 3.12: BSA adhesion to the pure component SAMs at high and low temperature, where a) is the $C_{11}EG_6OH$ at 22 °C, b) is the $C_{11}EG_6OH$ at 39 °C c) is the $C_{11}CH_3$ at 22 °C, and d) is $C_{11}CH_3$ at 39 °C.

Figure 3.13 shows the histograms of protein adhesion force at 22 °C for BSA, collagen, pyruvate kinase, cholera toxin subunit B, Ribonuclease A, and lysozyme. The majority of the force-distance curves exhibited no adhesion to the mixed $C_{11}EG_6OH/C_{11}CH_3$ SAM. These results are consistent with the hypothesis that the protein does not adhere to the mixed $C_{11}EG_6OH/C_{11}CH_3$ SAM surface at temperatures below the mixed $C_{11}EG_6OH/C_{11}CH_3$ SAM's molecular transition. It may be that the protein is denaturing to some extent during each force distance measurement. The extent of protein denaturing may give rise to the ocassional spurious adhesion event measured.

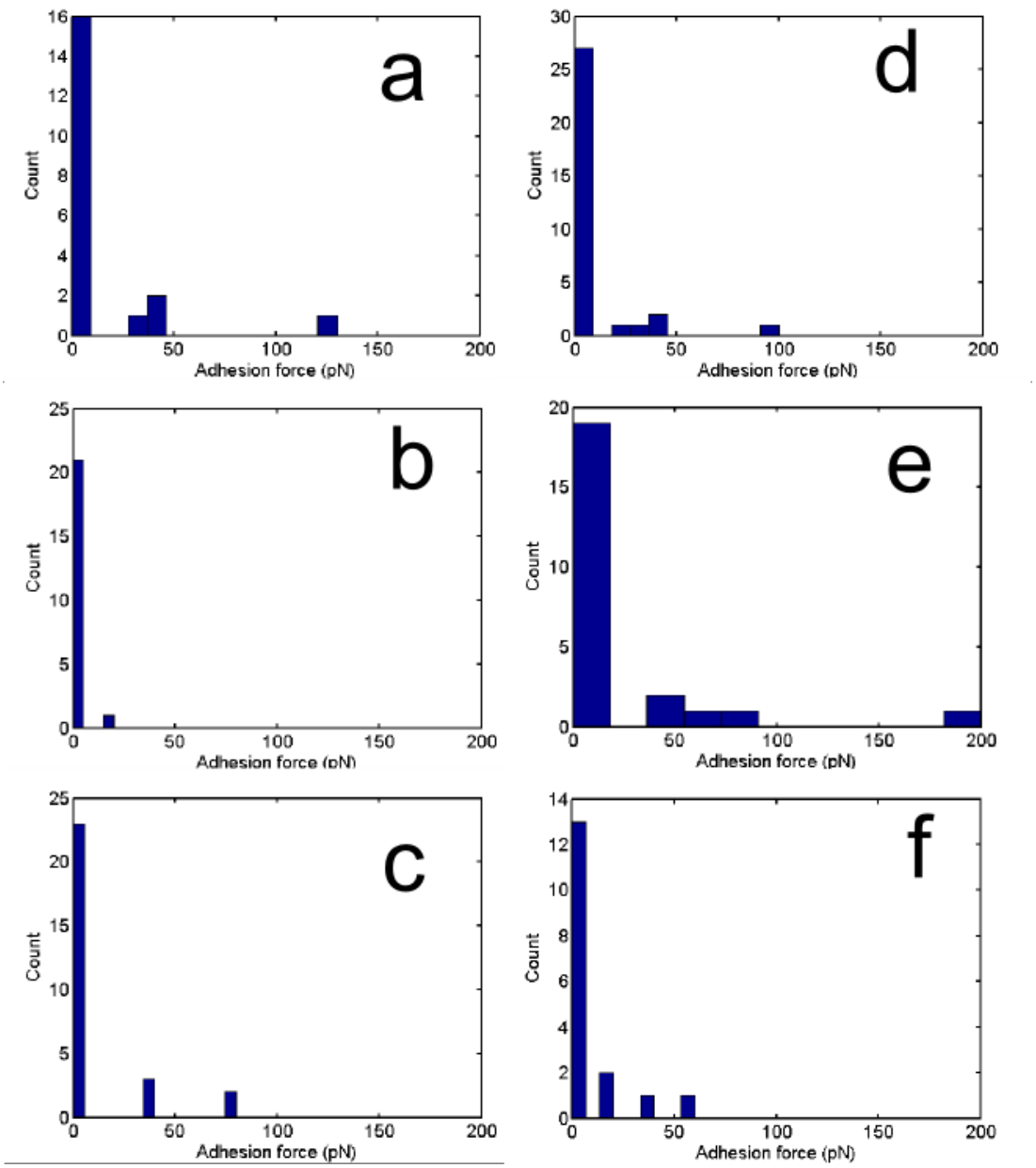


Figure 3.13: Adhesion force histograms of the various proteins to the mixed $C_{11}EG_6OH/C_{11}CH_3$ SAM at 22 °C, where a) is bovine serum albumin, b) is collagen, c) is pyruvate kinase, d) is cholera toxin subunit B, e) is ribonuclease A, and f) is lysozyme.

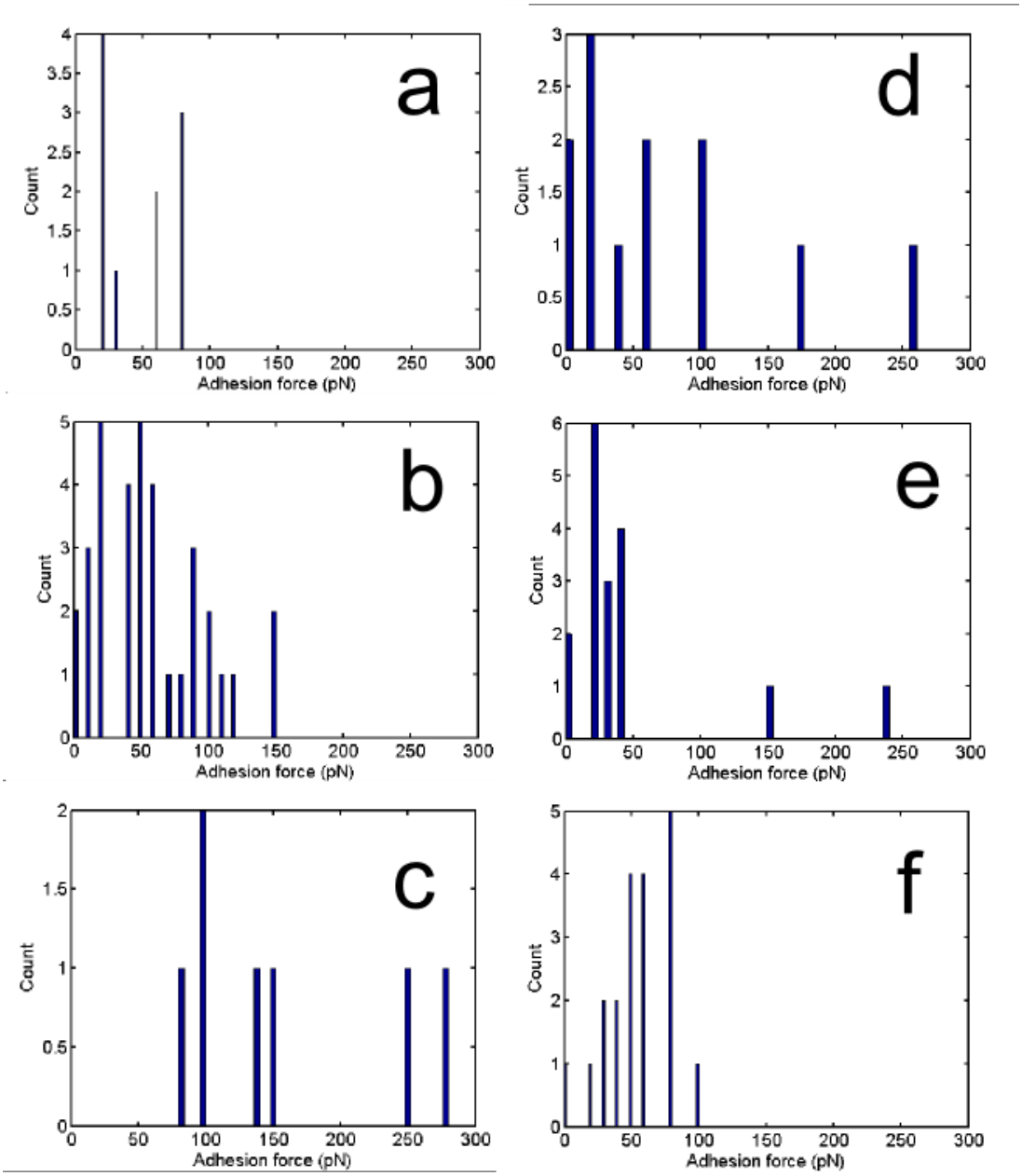


Figure 3.14: Adhesion force histograms of the various proteins to the mixed $C_{11}EG_6OH/C_{11}CH_3$ SAM at 39 °C, where a) is bovine serum albumin, b) is collagen, c) is pyruvate kinase, d) is cholera toxin subunit B, e) is ribonuclease A, and f) is lysozyme.

Figure 3.14 shows the histograms of protein adhesion at 39 °C, for BSA, col-

lagen, pyruvate kinase, cholera toxin subunit B, ribonuclease A, and lysozyme. In contrast to the measurements at 22 °C, the majority of the force-distance curves exhibited adhesion to the mixed $C_{11}EG_6OH/C_{11}CH_3$ SAM. The experiment was stopped when the force-distance curves showed 5 sequential non-adhesion events. It was assumed that at this point, the protein was displaced from the cantilever, because prior experiments showed no adhesion between a bare cantilever and the mixed $C_{11}EG_6OH/C_{11}CH_3$ SAM. The last 5 non-adhesion force curves were not included in these data. These results are consistent with the hypothesis that protein adheres to the mixed $C_{11}EG_6OH/C_{11}CH_3$ SAM at temperatures above the mixed $C_{11}EG_6OH/C_{11}CH_3$ SAM's molecular transition.

The majority of the adhesion strength lay below 100 pN; forces above 100 pN tended to be in the tail of the adhesive force population. Because the protein was dislodged from the cantilever, large sets of data were hard to acquire, making statistical analysis of the data difficult. Comparison to other protein on SAM studies is difficult because the surface chemistry of this mixed $C_{11}EG_6OH/C_{11}CH_3$ SAM is so unique. Futhermore, physical adsorption of the protein to the cantilever is different from the chemical attachment performed by other researchers. This will be discussed in more depth later in this chapter.

For temperatures above the molecular transition, the oligo ethylene glycol thiolate no longer has tightly bound water acting as a barrier to protein adhesion [3]. Thus, the molecule is less hydrophilic and the displaced water molecules allow for protein adhesion to the SAM surface.

Figure 3.15 shows the protein adhesion force measurements in sequence for the various proteins to the mixed $C_{11}EG_6OH/C_{11}CH_3$ SAM at 39 °C. The first data point in each of these curves gives information on the initial adhesion, when the protein is most likely to be in its native conformation. The sequential data points provide information about the adhesive forces for the protein when it maybe denaturing upon

the AFM cantilever. It has been shown that proteins can denature when exposed to hundreds of picoNewtons of force [64]. The force exerted in the experimental force-distance curves is approximately 500 pN. As the protein denatures during the force-distance curves, it may expose new regions of the protein that may be hydrophilic or hydrophobic in nature. It then follows that the adhesion trend will vary from force-distance curve to force-distance curve.

It is difficult to observe a correlation between protein size and adhesive force to mixed $C_{11}EG_6OH/C_{11}CH_3$ SAM surface. A comparison of lysozyme and collagen adhesion shows that both negative proteins tend to have peak adhesion strength in the tens of piconewtons and have no different in force-distance trends, Figure 3.14 and 3.15, b and f. The same is true for the positive proteins BSA and pyruvate kinase, Figure 3.14 and 3.15, a and c.

The same difficulty in observing a correlation is seen between protein charge and adhesive force. Collagen and pyruvate kinase, which are about the same molecular weight but of opposite charge, have similar adhesion forces and show no similar trends in sequencial force distance data, Figure Figure 3.14 and 3.15, b and c. The same is true for BSA and lysozyme, which are both about the same size but of opposite charge. Again the difficultly is present with ribonuclease A and lysozyme, a neutral and negative protein of similar size, Figure 3.14 and 3.15, e and f.

After the initial force-distance curve, it is believed that the proteins start to denature. Again it is difficult to observe a correlation between exposed amino acids and adhesive force and force trend for the proteins. Any correlation between collagen, which has the highest hydrophobic amino acid ratio, and the other more hydrophilic amino acid loaded proteins is difficult to argue. The ratio of hydrophilic to hydrophobic amino acid composition for the various proteins are: collagen (1:2), pyruvate kinase (1.2:1), CTB (1.5:1), BSA (1.6:1), lysozyme (1.7: 1), and ribonuclease A (2.4:1).

Until this point it was assumed that there is a single protein on the AFM cantilever. This is unlikely. There is probably a random number of proteins on the cantilever. The proteins are also likely in a distribution of configurations. The stochastic nature of the protein loading on the AFM cantilever makes it very difficult to observe and correlations between multiple variables.

Before the experimental values discussed above are compared to those obtained from literature, the attachment methods should be examined. Both a chemically bound protein and physically adsorbed protein on a cantilever will experience similar intermolecular forces. In both experiments, the protein can denature. Arguably, it is not known whether it is more realistic to chemically attach or physically adsorb a protein to an AFM cantilever. If the first force-distance curve denatures a protein, then both a chemically and physically adsorbed protein will encounter the same intermolecular forces at the SAM. If the forces between the cantilever and protein are greater than the forces between the tip and surface, the protein will remain on the cantilever. If the forces between the cantilever and protein are equal to the forces between the protein and surface, then the protein will adhere to both surfaces. This occurred on the mixed SAM at 39 °C where the protein was adsorbed strongly enough to both the cantilever and surface that it may have denatured as the cantilever was retracted. For cantilevers with chemically bound proteins, it is not necessary to consider the force between the cantilever and protein. As previous stated, where the extension (press force) for chemically bound proteins is greater than a couple hundred piconewtons then the protein can denature on the cantilever. Thus, the physically adsorbed protein data and chemically bound protein data can be compared. It is still not known what configuration or conformation the protein is in during any experiment at any given time. It should also be noted that only semiquantitative analysis of the force-distance data is possible due to the unknown precision of the cantilever spring constant and tip radius [6].

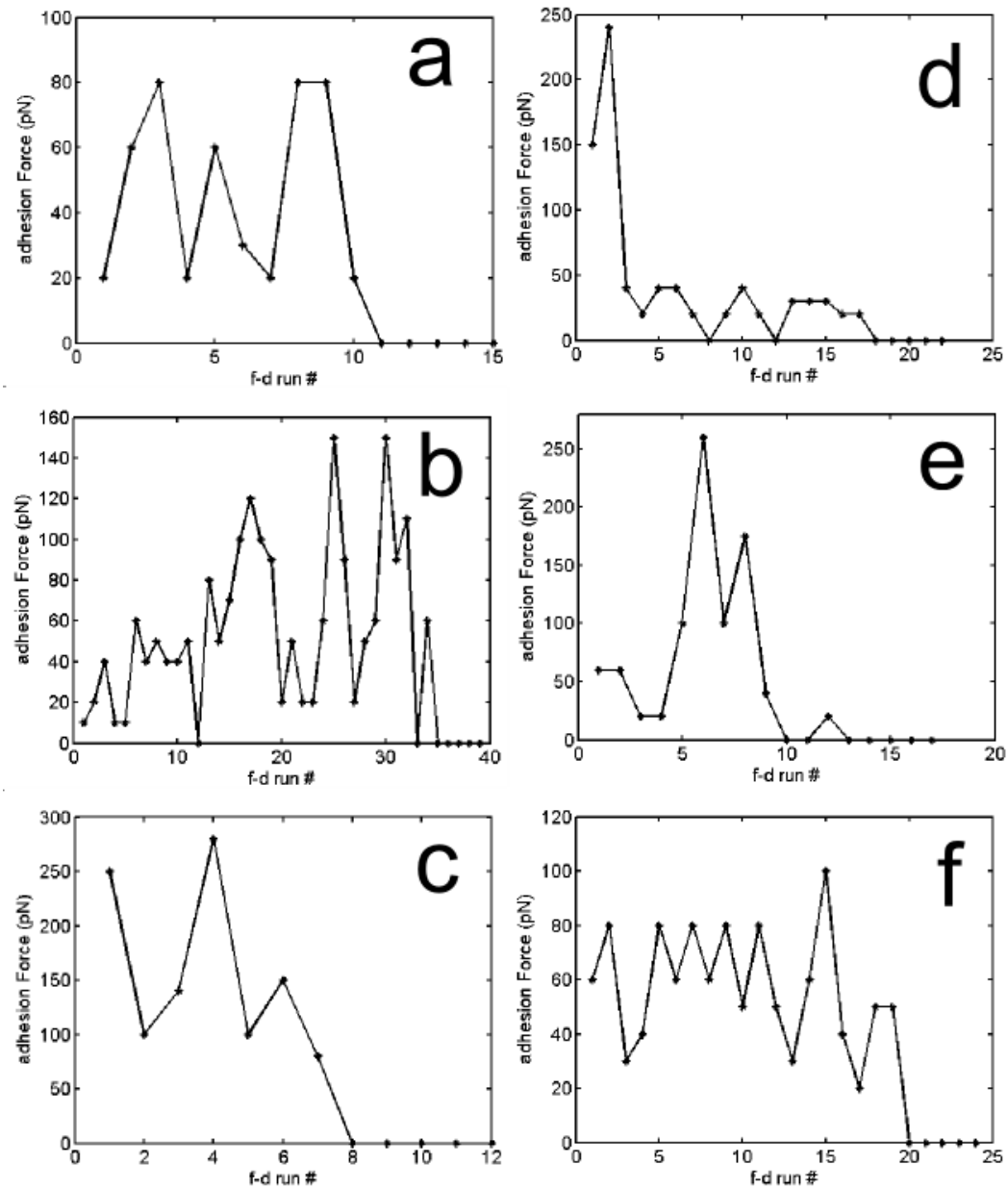


Figure 3.15: Sequential adhesion force measurements as a function of run number for the various proteins to the mixed SAM surface at 39 °C. a) is bovine serum albumin, b) is collagen, c) is pyruvate kinase, d) is cholera toxin subunit B, e) is ribonuclease A, f) is lysozyme. Measurements were terminated in each case after five consecutive measurements of no adhesion.

Various protein adhesion values from various surfaces relevant to the mixed $C_{11}EG_6OH/C_{11}CH_3$ SAM experiment have been taken from literature and presented in Table 3.3. The most important experimental variables that may determine the force of adhesion between a protein and surface are listed along with the source of the data. In an attempt to normalize all of the experimental data, the protein adhesive force was divided by the radius of the AFM cantilever used in the experiment. The first value in the table is a reference value of adhesion of a bare cantilever to a methyl terminated surface. All of the experiments in Table 3.2 were performed at room temperature (22 °C). In addition, all of the proteins were chemically attached to the AFM cantilever. From the table, it may be observed that the adhesion force is in the tenths of nN/nm irregardless of scan rate, contact time, and press force. There is a value in the table where the AFM cantilever had no point, thus the adhesive force is quite large and could not be ratioed to tip radius. The tipless cantilever has a large surface area giving rise to a larger force of adhesion than in other experiments with a pointed cantilever. It may also be observed that the $C_{11}EG_3OH$ surface is three oligo ethylene gylcol units shorter than $C_{11}EG_6OH$, but should still passivate the surface to protein adhesion [73]. In contrast, passivation is not seen and in one value the force of adhesion to the $C_{11}EG_3OH$ surface is greater than that to the methyl SAM. To make comparison even more difficult, passivation is seen on the methoxytri(ethylene glycol) EG_3Me SAM on gold, yet not on EG_3Me SAM on silver [6]. The exact reason for the inconsistency found in the literature is not known. It may be that the different experimental parameters may have influenced the results, in combination with the lack of knowledge of the amount of protein present on the AFM cantilever, cantilever geometry and nature of the surface during each force-distance curve.

There is some consistency between these experimental results, because the adhesive force of fibrinogen to the methyl SAM, 0.12 and 0.10 nN/nm, is nearly identical even though other experimental parameters were different. Before comparing our

Table 3.2: Table of protein adhesion forces to SAM surfaces at 22 °C with experimental parameters taken from literature.

AFM tip	Surface	Medium	Scan Rate	Contact Time	Press Force	Adhesion Force	Reference
Bare	CH_3	Air	1 Hz	< 1 sec	0 to 80 nN	0.30 nN/nm	[39]
Ribonuclease A	CH_3	PBS	0.1 Hz	10 sec	6 nN	0.06 nN/nm	[53]
Lysozyme	CH_3	PBS	0.1 Hz	10 sec	5 nN	0.12 nN/nm	[53]
Pyruvate kinease	CH_3	PBS	0.1 Hz	10 sec	5 nN	0.14 nN/nm	[53]
Fibrinogen	CH_3	PBS	0.1 Hz	10 sec	5 nN	0.12 nN/nm	[53]
Ribonuclease A	EG_3OH	PBS	0.1 Hz	10 sec	5 nN	0.12 nN/nm	[53]
Lysozyme	EG_3OH	PBS	0.1 Hz	10 sec	5 nN	0.05 nN/nm	[53]
Pyruvate kinease	EG_3OH	PBS	0.1 Hz	10 sec	5 nN	0.20 nN/nm	[53]
BSA no point	CH_3	PBS	4 Hz	< 1 sec	11 nN	0.87 nN	[67]
Albumin	CH_3	PBS	3.2 Hz	< 1 sec	2 nN	0.10 nN/nm	[74]
IgG	CH_3	PBS	3.2 Hz	< 1 sec	2 nN	0.08 nN/nm	[74]
Fibrinogen	CH_3	PBS	3.2 Hz	< 1 sec	2 nN	0.10 nN/nm	[74]
Fibrinogen	CH_3	PBS	0.5 Hz	2 sec	0.8 nN	0.10 nN/nm	[6]
Fibrinogen	EG_3Me-Au	PBS	0.5 Hz	2 sec	0.8 nN	no adhesion	[6]
Fibrinogen	EG_3Me-Ag	PBS	0.5 Hz	2 sec	0.8 nN	0.02 nN/nm	[6]

experimental results to the literature discussed here, it should be noted that the adhesive force is a function of many experimental parameters. These parameters were described in the introduction to this chapter.

The data collected in Table 3.3 was taken from the force-distance data presented earlier at 39 °C. We collected approximately 20 adhesion force values for each protein-surface interaction, from which we selected the most frequently occuring adhesion force values for the the table. First it should be noted that the press force used in collecting our data was in most cases an order of magnitude smaller than those found in the literature. The scan rate and contact time are similar in value to those in the literature. It is also noticed that our force of adhesion values are in the thousandths of nN/nm, which is two orders of magnitude smaller than those reported in the literature. This may be because of experimental factors that contribute to the adhesion force. The difference may also arise from the fact the protein is not chemically attached to the cantilever. The source of the adhesion force value should also be considered in comparison to the literature values. The adhesion force in Table

Table 3.3: Table of protein adhesion forces to the SAM surfaces at 39 °C.

AFM tip	Surface	Medium	Scan Rate	Contact Time	Press Force	Adhesion Force
BSA	CH_3	PBS	0.1 Hz	10 sec	0.5 nN	0.002 nN/nm
BSA	EG_6OH	PBS	0.1 Hz	10 sec	0.5 nN	no adhesion
BSA	mixed	PBS	0.1 Hz	10 sec	0.5 nN	0.002 nN/nm
Collagen	mixed	PBS	0.1 Hz	10 sec	0.5 nN	0.004 nN/nm
Pyruvate kinase	mixed	PBS	0.1 Hz	10 sec	0.5 nN	0.010 nN/nm
CTB	mixed	PBS	0.1 Hz	10 sec	0.5 nN	0.002 nN/nm
Ribonuclease A	mixed	PBS	0.1 Hz	10 sec	0.5 nN	0.002 nN/nm
Lysozyme	mixed	PBS	0.1 Hz	10 sec	0.5 nN	0.008 nN/nm

3.3 is from a population of adhesion values, which range from zero to 0.026 nN/nm. The data taken from literature were extracted from a single force-distance curve. The literature did not report any statistical measurements of the force-distance curves of the protein to the various surfaces. The difference in values could be from the unknown effect of temperature on the adhesive force. It is also possible that our thermally responsive mixed $C_{11}EG_6OH/C_{11}CH_3$ SAM cannot be directly compared to SAMs that are not thermally responsive.

3.4 Conclusion

The data presented in this chapter are consistent with the hypothesis that there is a change in protein adhesive force to the mixed $C_{11}EG_6OH/C_{11}CH_3$ SAMs above and below the molecular transition. We have shown semi-quantitatively that protein adhesion can be controlled by the thermally repsonsive mixed $C_{11}EG_6OH/C_{11}CH_3$ SAM surface. This chapter provided a description of the numerous factors, surface properties, and intermolecular forces that may govern protein adhesion. The mixed $C_{11}EG_6OH/C_{11}CH_3$ SAM used in this section were confirmed to be thermally responsive. The results of the mixed $C_{11}EG_6OH/C_{11}CH_3$ SAM characterization by AFM and contact angle goniometry were shown to be similar to the characterization results described in chapter 2. The force-distance data were described along with

the method used to process the data. The population of force-distance data was given along with a sequencial presentation of each protein force-distance curve. The data of the adhesive force of the protein to the various SAMs were presented and compared with relevant values taken from literature.

Chapter 4

Lewis Acid-Base Surface Energies of Mixed Self-Assembled Monolayers

4.1 Introduction

Researchers are looking to find a determining factor that can predict bioadhesion to surfaces. It is widely held that surface free energy is a determining factor in bioadhesion [75, 76, 77, 78, 79, 52, 80]. Often confusing at first, surface free energy (J/m^2) is interchangable with surface tension (N/m) [57, 80]. To examine the surface free energy of bioadhesion, the surface free energy can be separated into the sum of three parts: (1) the surface tension for the adhering species with surface, (2) the surface tension between medium and adhering species, (3) and the surface tension of the solid surface and medium. To stay consistant with published literature, the adhering species will be labeled (B) for bacteria, the medium will be (W) for water, and (S) for substrate. Thus, the surface free energy of bioadhesion can be written

[14],

$$\Delta G = \gamma_{BS} - \gamma_{BW} - \gamma_{SW} \tag{4.1}$$

where γ_{BS} is the surface tension between bacteria and substrate, γ_{BW} is the surface tension between bacteria and water, γ_{SW} is the surface tension between water and substrate. To find the surface free energy of bioadhesion the surface tension between the substrate and water must be found.

Over the last century, many different models have been used to measure surface energy via contact angle, including: the Zisman method [81], the Good-Garifalco method [82], the Fowkes method [83], the Geometric mean method (Owens-Wendt method) [84], the Wu method [85], the Equation of State method, and the van Oss-Good-Chaudhury method (Lewis acid-base model) [86]. For a comprehensive comparison of these models, see the work of Sharma and Rao [79].

For the purposes of this research, the Lewis acid-base model (LAB) was used because it has been argued that this model best describes hydrogen bonding, a critical factor in bioadhesion [14]. It should be noted that the LAB model has been criticized for using incorrect water parameters [87] and failing to yield solutions to all, rather than only some, solvents [79]. The corrected parameters result in only a small change in final free energy values when compared to the original parameters [80].

In the LAB model, a Lewis acid compound accepts a pair of electrons from a Lewis base. Figure 4.1 shows how the lone electron pair on ammonia, a Lewis base, is donated to the incoming proton, a Lewis acid.

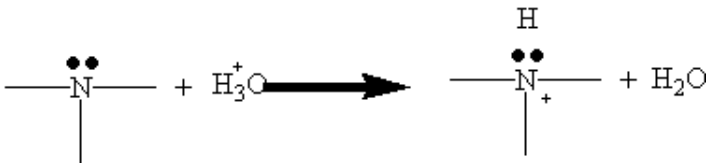


Figure 4.1: Example of the Lewis acid-base interacts

The surface tension can be represented as the sum of the Lifshitz-van der Waals (LW) surface tension and the acid-base (AB) surface tension,

$$\gamma = \gamma^{LW} + \gamma^{AB}. \tag{4.2}$$

The acid-base component of the surface tension can be expanded further into individual components,

$$\gamma_i^{AB} = 2\left(\gamma_i^+ \gamma_i^-\right)^{1/2} \tag{4.3}$$

where γ_S^+ is the acidic component of the surface tension, and γ_S^- is the basic component of the surface tension.

The following Equation 4.4 shows the LAB model:

$$\gamma_L\left(1 + cos\theta\right) = 2\left(\gamma_S^{LW} \cdot \gamma_L^{LW}\right)^{1/2} + 2\left(\gamma_S^+ \cdot \gamma_L^-\right)^{1/2} + 2\left(\gamma_S^- \cdot \gamma_L^+\right)^{1/2} \tag{4.4}$$

where γ_L is the surface energy of the liquid, θ is the contact angle of the liquid phase on the solid phase, γ_S^{LW} is the Lifshitz-van der Waals surface energy of the solid, γ_L^{LW} is the Lifshitz-van der Waals surface energy of the liquid. In order to use this model the contact angle of three liquids must be obtained on the surface, one of the liquids must be an apolar species while the other two polar. An ideal choice of polar liquids would have a large acidic surface tension while the basic surface tension is very weak. The other polar liquid should have a strong basic

surface tension and weak acidic surface tension. There are three sets of combinations that are less sensitive to solvent choice when used in the LAB model, they are: (water, glycerol, bromonapthalene), (water, diiodomethane, glycerol), and (water, diidomethane, formamide) [80].

For an apolar species, where the acid and base components are 0, Eq. 4.4 simplifies to,

$$\gamma_S^{LW} = \frac{\gamma_L^2 \left(1 + cos\theta\right)^2}{4\gamma_L^{LW}}. \tag{4.5}$$

For diiodomethane, where Liftshitz-van der Waals energy is equal to the surface energy of the liquid, further rearrangement yields,

$$\gamma_S^{LW} = \frac{\gamma_L \left(1 + cos\theta\right)^2}{4}. \tag{4.6}$$

To obtain the γ_S^+ and γ_S^- the system of three equations must be solved with the contact angles and parameters from the three probe liquids.

Our research group hypothesizes that surfaces with varied acid-base energies will exhibit different bioadhesion. For this chapter we hypothesize that varying the surface mole fraction of N,N,N-Trimethyl-10-undecenylammonium chloride thiol (NMe_3) relative to $C_{11}CH_3$ will change the surface energy and result in increased or decreased bacterial adhesion. To test our hypothesis, we used the LAB model to characterize two mixed SAM surfaces: $C_{11}EG_6OH/C_{11}CH_3$ and $NMe_3/C_{11}CH_3$. In the next phase of our research, Linnea Ista will examine the attachment of bacteria to the $NMe_3/C_{11}CH_3$ SAM. We selected NMe_3 because the end ammonium group possesses a positive charge and should be Lewis basic, whereas $C_{11}EG_6OH$ has an end group that possesses a lone pair of electrons and should be Lewis acidic.

4.2 Materials and Methods

N,N,N-Trimethyl-10-undecenylammonium chloride thiol (NMe_3) and hexa(ethylene glycol) thiol ($C_{11}EG_6OH$) were purchased from Prochimia, Poland and were used in 1mM ethanic solutions. 1-dodecanethiol 98% ($C_{11}CH_3$), formamide 99%, diiodomethane 99.5%, were purchased from Sigma-Aldrich and were used as received. Nanopure water (18.3 MΩ) was produced in-house.

Microscope coverslips (25mm X 50 mm) were cleaned in piranha etch, 75% H_2SO_4 25% H_2O_2 (vol/vol), for 2 hours and then rinsed with copious amount of nanopure water and dried with a steam of nitrogen. An adhesion promoting layer of chromium (30 $\AA$) followed by gold layer (300 - 3000 $\AA$) was deposited by thermal evaporation at 10^{-6} Torr. The same procedure was repeated for the opposite side. 1 mM NMe_3 was mixed with 1 mM CH_3 in ethanol to give the desired volume fractions ranging from pure NMe_3 to pure CH_3. The slides were then placed in ethanol solutions at room temperature overnight. The slides were removed from solution and rinsed with ethanol and dried in a stream of nitrogen.

Equipment Contact angles were then obtained with a Kruss K-100 tensiometer. Immersion depth was 5 mm into each of the solvents. An external water circulating bath was used to control the temperature of the tensiometer fluid vessel. Tensiometer measurements were recorded for the mixed $NMe_3/C_{11}CH_3$ SAM at room temperature (22°C) recording the advancing and receding contact angles. The software program LabDesk calculated the advancing and receeding contact angles from the tensiometer force measurements. The six solvents used were: deionized water, chloroform, hexadecane, formamide, glycerol, ethyl acetate, bromoform, and diiodomethane. Only values collected from water, formamide, and diiodomethane were used in the calculation of the LAB model. For the mixed $C_{11}EG_6OH/C_{11}CH_3$ SAM, an external temperature bath raised the surface tension apparatus and test so-

lution temperature to 40 ± 1 °C. The advancing contact angles are used throughout this work.

XPS scans were performed with a Kratos Axis Ultra spectrometer using an Al Kα X-ray source. An electron flood gun for charge neutralization and hemispherical analyzer with eight multichannel photomultiplier detector was employed for analysis. Three areas per sample were analyzed with a 90 degree take-off angle (TOA), 8-10 nm depth. Area of analysis was 700 x 300 microns in size. Survey spectra (low resolution wide scan) were acquired at 80 eV pass energy for four minutes. High resolution spectra were acquired at 20 eV pass energy. The C-C calibrated to 285.0 eV. Fit peaks were constrained by a full width half maxium value between 1.2 and 2 eV. The C-C peak fit was further constrained to a position of 284.9 to 285.1 eV.

4.3 Results and Discussion

The SAM surfaces created with the two thiols, NMe_3 and $C_{11}CH_3$, were characterized with XPS, data shown in Figure 4.2. The survey spectrum of the mixed SAM showed only carbon and gold peaks, the nitrogen, and sulfur peaks were not distinguishable from background noise. The pure component $C_{11}CH_3$ SAM has a characteristic carbon-carbon peak at 285 eV. The pure component NMe3 SAM has a characteristic nitrogen-carbon peak at 287 eV. While this peak may also correspond to photoelectrons from an ether carbon, it is believed that they are not present in either SAM. The surface mole fraction can be calculated by comparing the area under the XPS peaks of a mixed $NMe_3/C_{11}CH_3$ SAM to that of the pure component peak areas, as discussed in chapter 2 for the mixed $C_{11}EG_6OH/C_{11}CH_3$ SAMs. The surface mole fraction as a function of NMe_3 thiol volume fraction is shown in Figure 4.4. This graph was calculated using the area of the high resolution C 1s carbon-carbon peak fits of the pure $C_{11}CH_3$ to the pure NMe_3. A linear fit between the

two pure component thiolates results in the surface mole fraction of NMe_3. NMe_3 is similar to the $C_{11}EG_6OH$ molecule in that it is more soluble in solution than the $C_{11}CH_3$. The same arguements for needing a higher volume fractions of $C_{11}EG_6OH$ presented in chapter 2 can also be applied to mixed $NMe_3/C_{11}CH_3$ SAM surface loading. Thus, volume fractions of almost pure NMe_3 would yield an equal ratio of thiols components on the surface.

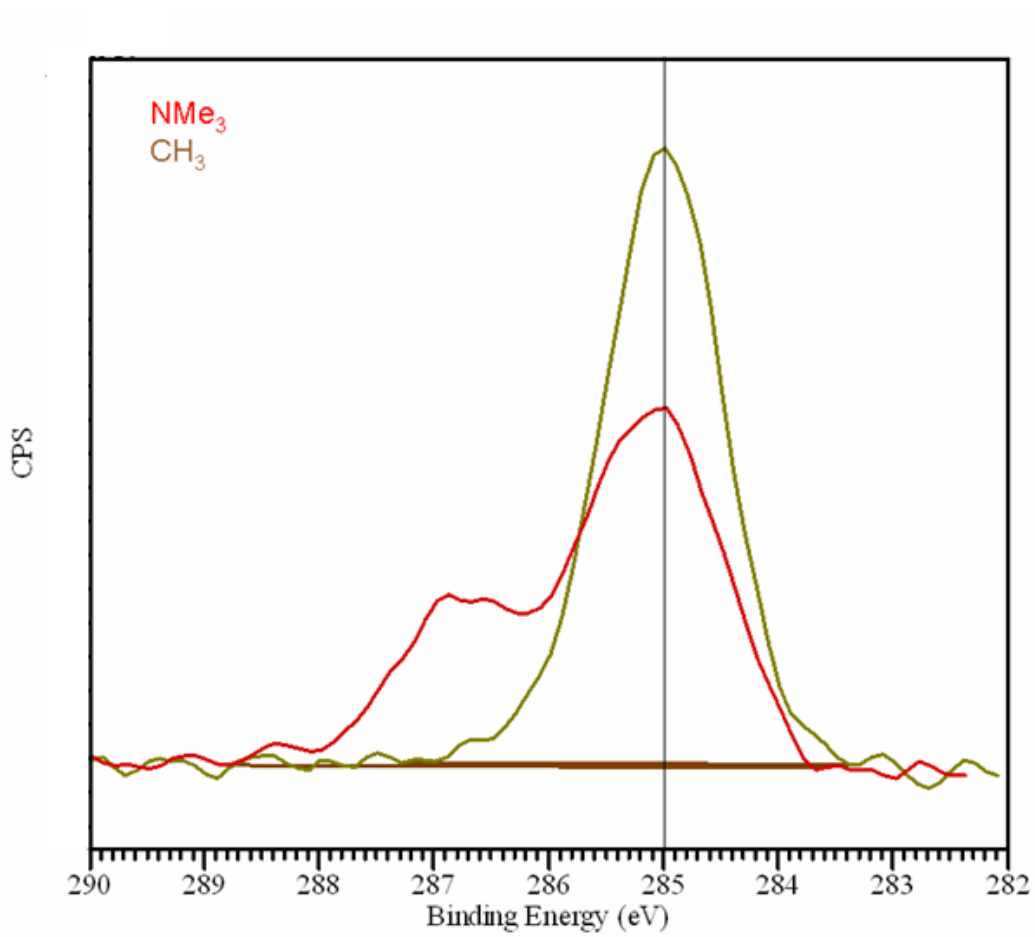


Figure 4.2: High resolution XPS spectrum of pure $C_{11}CH_3$ and NMe_3 surfaces

The elemental composition from XPS is shown in Table 4.1. Figure 4.3 shows the high resolution C 1s spectrum of the NMe_3 SAM. The predicted atomic composition of the NMe_3 SAM is C-H 69.3% and C-N 30.7%. This is very similar to the observed

Table 4.1: Elemental composition from XPS survey spectra of the SAMs, one sample scanned in three areas, standard deviation is less than 2%.

SAM	C %	O %	N %	S %
$C_{11}CH_3$	100	0	0	0
NMe_3	83.3	0	16.7	0

Table 4.2: High Resolution C1s composition from XPS spectra of the SAMs, one sample scanned in three areas, standard deviation is less than 2%.

SAM	C-H %	C-N %
NMe_3	69.1	30.9

fits of 69.1% and 30.9% shown in Table 4.2. The peak at 286.8 eV may be from the photoelectrons of an ether carbon, but the presence of ether carbons in either SAM is unlikely.

Contact angle goniometry was used to examine the change in wettability of the surfaces, thus supporting a change in surface chemistry. A single double-sided surface SAM was used to obtain the contact angles of water, diiodomethane, and formamide for the various volume fractions are shown in Figure 4.5. The NMe_3 SAM surface should be hydrophilic (sessile drop water contact angle $< 15°$ [88]), which is consistent with the data. As the surface mole fraction of NMe_3 decreases, the contact angle increases, showing a increasing hydrophobic character of the surface. A pure component $C_{11}CH_3$ surface should have a water contact angle of about 110° [39, 89, 90]. The contact angle value for a pure $C_{11}CH_3$ surface, not shown in the graph, was confirmed by experiment to be 110°.

Contact angle values obtained in Figure 4.5 and the data in Table 4.3 can be used with Equation 4.6 to calculate the LAB surface energy of the various SAMs. It was confirmed that the combination of diiodomethane, water and formamide yielded solutions to Equation 4.4. Combinations of the other solvents often yielded complex

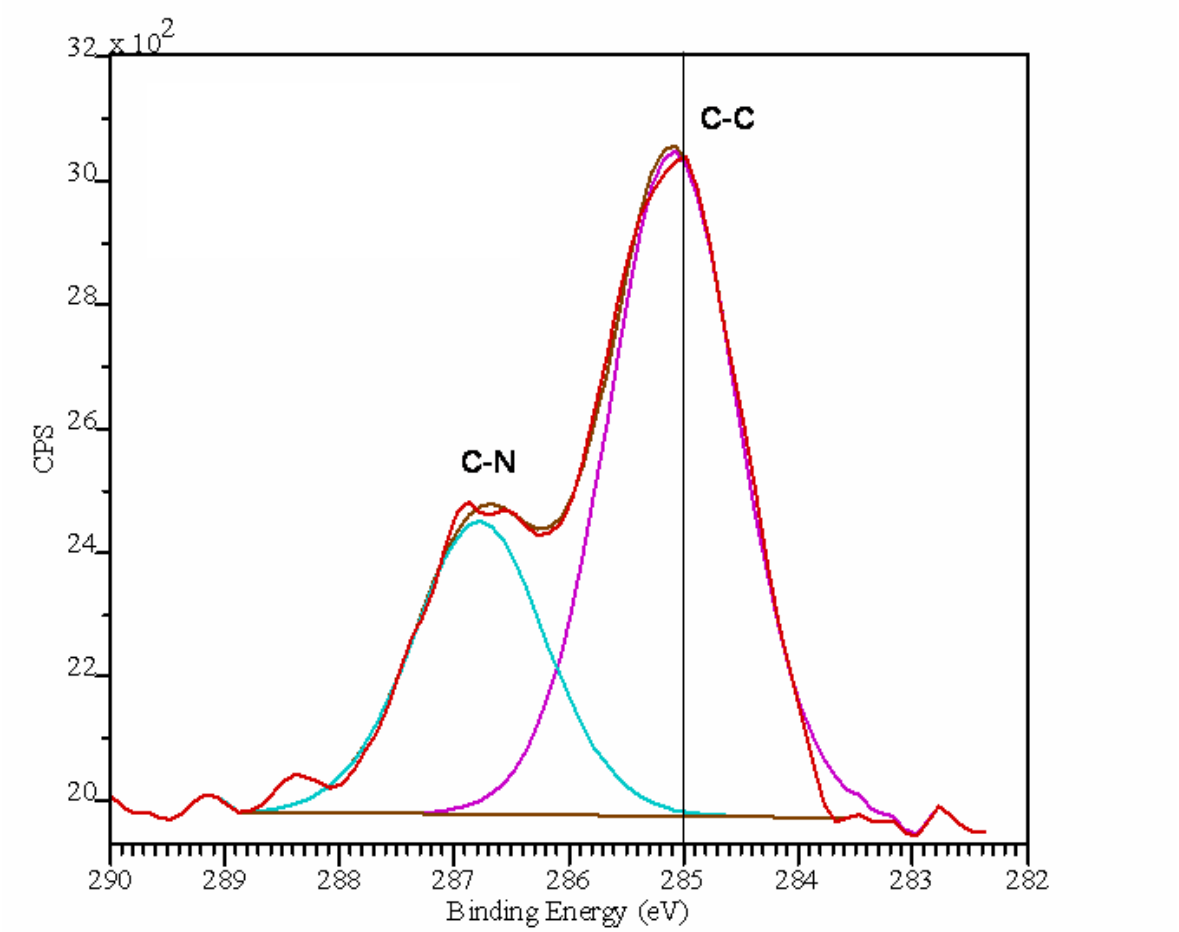


Figure 4.3: High resolution XPS spectrum of a pure NMe_3 SAM with compositional fit.

or non-realistic (negative or zero surface energy) results. This is consistent with literature [79, 80]. The resulting LAB surface energy values are shown in Figure 4.6. The values do not follow a linear combination between the two pure component SAMs. This is likely because of the non-linear surface loading shown in Figure 4.4. The error bars shown in the surface energy values are the standard deviation carried over from the contact angles. The results we obtained for the Liftshitz-van der Waals energy of a methyl terminated SAM, 17 $\pm$ 1 mJ/m^2, which are lower than AFM measurements in air performed by Beach et al., 25 mJ/m^2, [39], yet similar

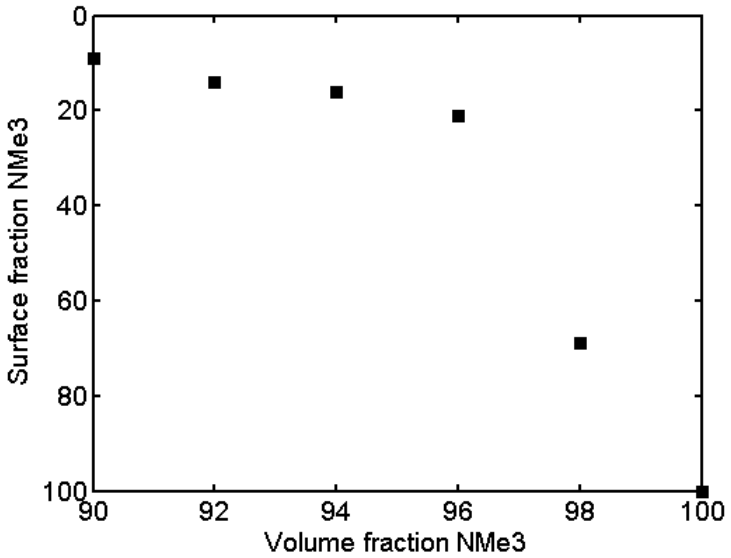


Figure 4.4: Surface volume fraction compared to the volume fraction used to create the mixed $NMe_3/C_{11}CH_3$ SAM surfaces.

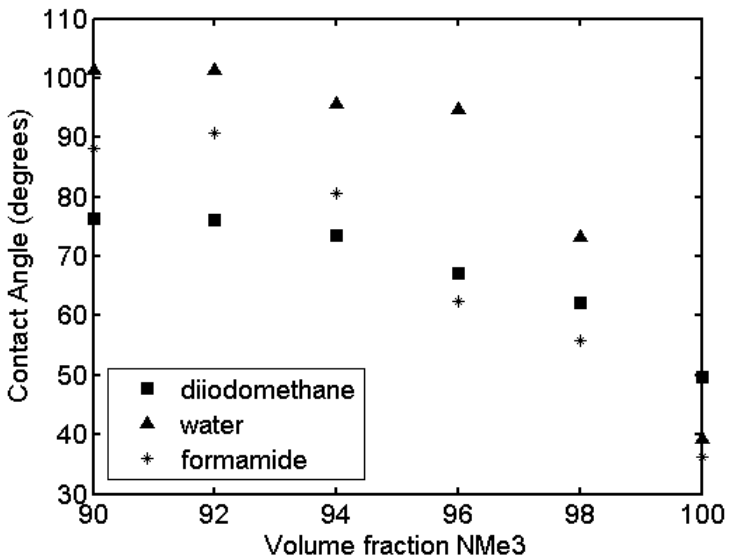


Figure 4.5: Contact angles for various liquid on the mixed $NMe_3/C_{11}CH_3$ SAM surfaces. Error is less than 5°.

to those reported by contact angle, 19.3 mJ/m^2 [89]. The fabrication methods for SAMs are different in every laboratory, different metal depositon techniques, different substrates and surface roughness. The surface irregularities of the gold and glass substrate determine thiol arrangement on the surface of the gold can give rise to the differences in calculated free energy values. Of course the model used to calculated the surface free energy is also a factor in the results. The higher the volume fraction of NMe_3 the higher the surface energy. This is expected because the NMe_3 charge gives rise to charge-dipole and other intermolecular forces which raise the surface tension of the medium [57].

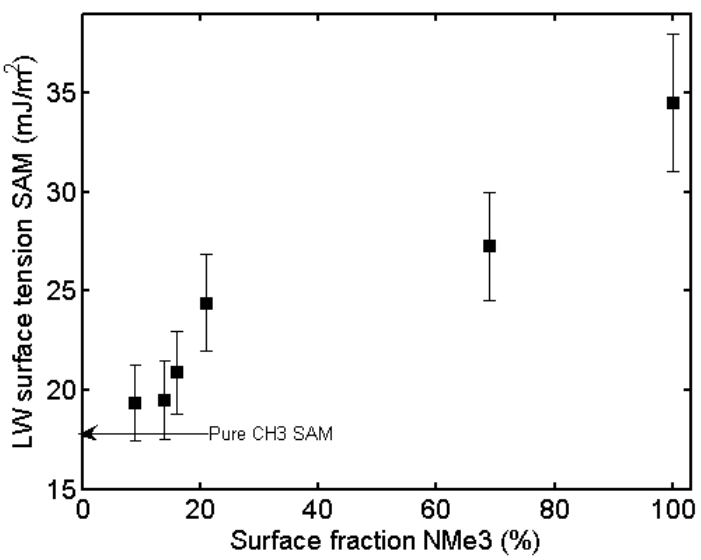


Figure 4.6: The Lifshitz-van der Waals surface tension for the various fractions of mixed SAMs

The acid and base surface tension components are shown in Figure 4.7. The calculated acid and base surface tension of the $C_{11}CH_3$ SAM was zero for both, this is consistent with literature [39]. As the surface mole fraction of NMe3 increases, the acidic component of the surface tension stays around zero. Again, the values do not follow a linear combination between the two pure component SAMs. This is likely

Table 4.3: Surface tension values used in the calculation of surface free energy of the mixed SAMs. Values taken from [14] or documentation provided by Kruss for tensiometry.

Solvent	$\gamma_L(mJm^{-2})$	$\gamma_L^{LW}(mJm^{-2})$	$\gamma_L^{+}(mJm^{-2})$	$\gamma_L^{-}(mJm^{-2})$
Water	72	21.8	25.5	25.5
Chloroform	38.8	27.15	1.5	0
Hexadecane	51.3	27.47	0	0
Formamide	58.0	39.0	2.28	39.6
Glycerol	64.0	34.0	3.92	57.4
Ethyl acetate	25.95	23.9	0	6.2
Bromoform	41.4	15.0	15.7	3.59
Diiodomethane	50.8	50.8	0	0

because of the non-linear surface loading shown in Fig. 4.4. The basic component of the surface tension increases with increasing NMe_3 surface fraction. This follows logic, increasing the number of tertiary nitrogen carrying a positive charge increases the number of electron accepting sites resulting in the increase in Lewis acidic nature.

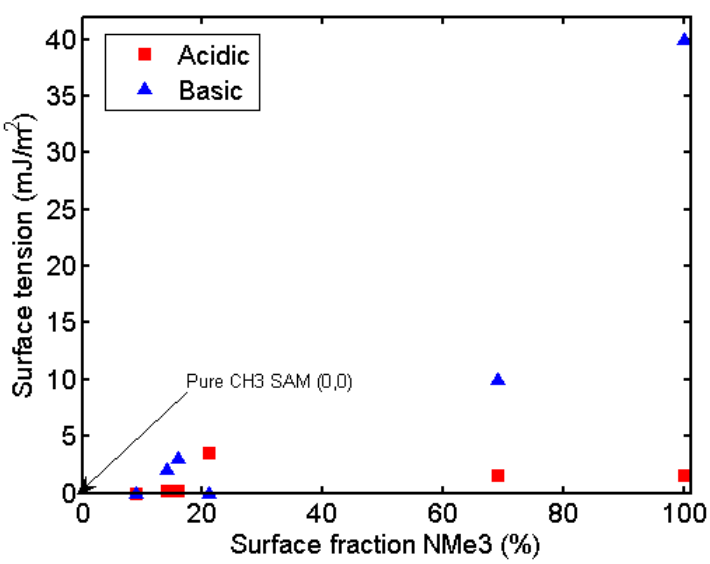


Figure 4.7: The acid and base surface tensions for the various fractions of mixed $NMe_3/C_{11}CH_3$ SAMs, error is not shown and is no greater than 2 mJm^{-2}

The full test of the LAB method will come with the results of the bacterial adhesion to the mixed $NMe_3/C_{11}CH_3$ surface. Yet, the various surfaces characterized tend to stay consistent with the predictions of the model.

4.3.1 Lewis acid-base surface tensions of mixed $C_{11}EG_6OH/C_{11}CH_3$ SAMs

Again, the problem of bioadhesion is quite complex. If the LAB model can help predict resistance to bioadhesion it should be examined. To calculate the acid-base surface tensions above and below the molecular transition the model must be tested at 22 and 40 °C. The LAB model was used to calculate the acid-base tensions of the mixed $C_{11}EG_6OH/C_{11}CH_3$ SAMs. The resulting values are in Table 4.4.

The change in surface tension should be a linear combination of the two individual components. The total surface energy being the sum of the individual components [14]. Figures 4.8, 4.9, and 4.10 show the surface tension, Lewis acid and base surface tension with a linear fit to show the deviation from the predicted behavior of the two individual components. In Figures 4.8, 4.9, and 4.10 the colder values shown in blue correspond to higher values of the surface tension. The measurements at 40 °C should be lower than the blue values in accordance with the decrease in surface tension of water. The noise in the data makes verification of the decrease in surface

Table 4.4: Surface tension values of the mixed $C_{11}EG_6OH/C_{11}CH_3$ SAMs

SAM and Temperature (°C)	$\gamma_S^{LW}(mJm^{-2})$	$\gamma_S^{+}(mJm^{-2})$	$\gamma_S^{-}(mJm^{-2})$
$C_{11}EG_6OH$ 22	42	15	13
$C_{11}EG_6OH$ 40	38	12	14
$C_{11}EG_6OH/C_{11}CH_3$ 22	41	12	13
$C_{11}EG_6OH/C_{11}CH_3$ 40	40	11	13
$C_{11}CH_3$ 22	17	0	1
$C_{11}CH_3$ 40	19	0	1

tension difficult.

The calculated surface free energy of a pure $C_{11}CH_3$ SAM at 22 °C is 17 ± 2 mJ/m^2. This value is in agreement with literature for a methyl terminated SAM obtained by contact angle, 19.3 mJ/m^2 [89]. The calculated value differs slightly when compared to the surface free energy of a $C_{11}CH_3$ SAM obtained by AFM force measurements, 25 mJ/m^2 [39]. The roughness, purity, and uniformity of the gold layer underlying the SAM could account for these differences. The models used to calculate the surface free energy may be the reason why AFM and goniometry produce different results.

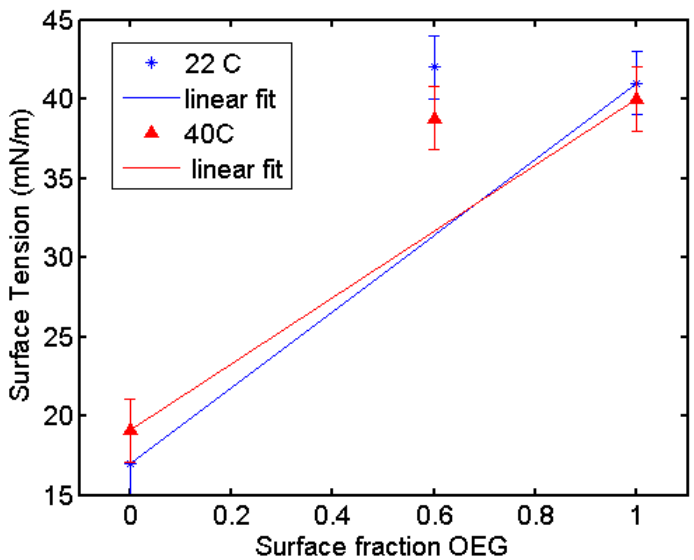


Figure 4.8: Mixed $C_{11}EG_6OH/C_{11}CH_3$ SAM surface tension

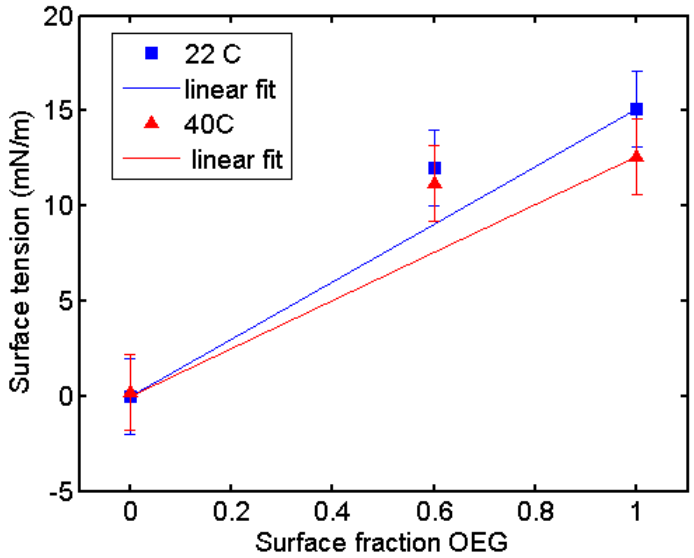


Figure 4.9: Mixed $C_{11}EG_6OH/C_{11}CH_3$ SAM acidic component of surface tension

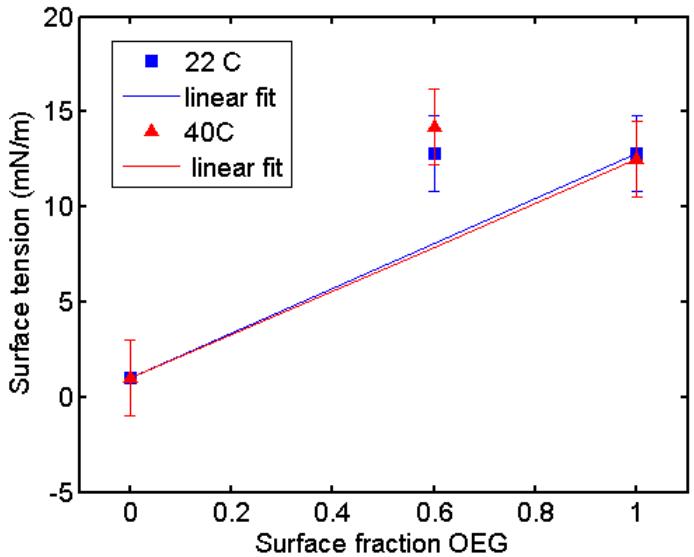


Figure 4.10: Mixed $C_{11}EG_6OH/C_{11}CH_3$ SAM basic component of surface tension

4.4 Conclusion

This work was done in collaboration with a coworker who will examine the effects of these mixed $C_{11}CH_3/NMe_3$ surfaces with respect to adhesion of bacteria. The experimental values calculated for the LAB surface energies of the $C_{11}CH_3$ surface were consistent with literature. The surface energies increased with increasing mole fraction of NMe_3. The base component of the surface energy stayed near a zero value for all surface fraction of NMe_3, which was expected. The acid component of the surface energy increased with increasing surface fraction of NMe_3, which is again as expected. The mixed $C_{11}EG_6OH/C_{11}CH_3$ SAMs LAB surface energy was examined above and below the molecular transition. The mixed $C_{11}EG_6OH/C_{11}CH_3$ SAM did not follow a linear trend between the individual SAM surface energies.

Chapter 5

Synthesis and Characterization of Poly(*N*-isopropylacrylamide) as a Model Thermally Dependant Bioadhesive Surface

5.1 Introduction

PNIPAAm is a thermally responsive polymer exhibiting a lower critical solution temperature (LCST) in water of approximately 32 °C [91, 92, 93, 94, 95]. The LCST is the temperature at which the polymer collapses from a hydrated random coil to a dehydrated globule, and was first observed by laser light scattering [96]. PNIPAAm has a hydrophilic amide group, and a hydrophobic isopropyl group, as seen in Figure 5.1.

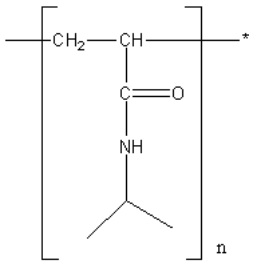


Figure 5.1: Chemical structure of PNIPAAm

At temperatures below the LCST, it is believed the polymer in solution is stabilized by the presence of hydrogen bonds between the hydrophilic groups and water, and by ice-like water structures around the hydrophobic sections of the molecule [57]. As temperature increases, the hydrogen bonding of the amide group shifts from occuring between water molecules to occuring with other amide groups. The shift in hydrogen bonding during the LCST transition was initially observed by FTIR [97, 95]. The shift in hydrogen bonding causes the precipitation of the PNIPAAm molecule above the LCST. A similar shift in hydrogen bonding was observed by sum frequency generation spectroscopy for surface grafted and spin coated PNIPAAm before and after the LCST [98].

Many of the bulk solution properties of PNIPAAm have been studied by thermal [91], mechanical [92], structural [94, 99], chemical [95, 100], and optical techniques [93, 91]. Surface grafted PNIPAAm exhibits a similar molecular conformation change compared to bulk PNIPAAm at the LCST [5, 101, 102, 68, 10, 103, 104, 105, 106].

The change in molecular conformation of PNIPAAm was first used to elicit the adhesion and then release of bovine hepatocyctes on a radiation grafted PNIPAAm Petri dish [107]. Since this first study, many researchers have used the thermal response of PNIPAAm grafted surfaces to release cell sheets, thus forming a powerful approach to tissue engineering [92, 108, 27, 109, 110, 104]. PNIPAAm has also been used to release surface attached marine biofilms [111], and adsorbed proteins

[112, 101]. The Lewis basic nature of PNIPAAm, which results in hydrogen bonding to water, is thought to prevent protein adhesion [112]. When PNIPAAm undergoes the change in molecular conformation, the hydrogen bonding to water is no longer present and proteins will thus adsorb to a PNIPAAm surface [36, 112]. Water acts as a moving barrier that prevents protein adsorption [35]. Thus, when the PNIPAAm molecule collapses and looses hydrogen bonding with water it no longer possesses this moving barrier against protein adsorption.

There are many methods to graft PNIPAAm to a surface. As indicated above, surface modification with PNIPAAm was first performed by gamma radiation to a Petri dish [107]. This method is effective, but few laboratories are set-up for gamma radiation grafting. PNIPAAm was polymerized within a porous membrane using ultra-violet radiation, which is safer than gamma radiation, but offers little control over the polymerization [113]. Plasma polymerization of PNIPAAm (pPNIPAAm) allows a variety of chemically different surfaces to be grafted [102, 114]. However, the vacuum equipment and plasma chamber required for this method make plasma polymerization more expensive than solution chemistry. PNIPAAm can be grown from SAMs with azo-initiators, but result in poor yield and non-uniform surface coverage [115]. Reversible addition fragmentation chain transfer (RAFT) offers control of polymerization in bulk solution [116]. As of yet, commercial reagents for using RAFT to graft to surfaces are not available.

In comparison, ATRP is a living radical polymerization and gives some control over the degree of polymerization [117]. The initiators needed for ATRP polymerization can be commercially obtained or synthesized [118]. Most studies of surface grafted PNIPAAm brushes with controlled molecular weight and height use ATRP [5, 101, 68, 10, 103, 104]. Solution-based ATRP reactions are preferred due to simplicity. ATRP initiator surface density affects the homogeneity, and terminal polymer thickness [119]. Initiator surface density and reaction method also affect the LCST

of PNIPAAm [10]. A follow-up study of surface grafted PNIPAAm at low molecular weight showed that it does not exhibit a thermo-response [103]. It is therefore important to have a reaction that can control both the surface density of the initiator and the degree of polymerization. The ATRP reaction can be stopped by oxygen, or other electronegative atoms and molecules [120]. Therefore it is important to preform ATRP reactions in a clean, oxygen free environment. Yet, ATRP in air is not impossible, adding select reducing agents can reverse the oxidation by oxygen to enable ATRP to be performed in air [121]. With the reagents commercially available, the ability to control the degree of polymerization and uniform surface coverage, ATRP is a preferred method of controlled PNIPAAm surface grafting.

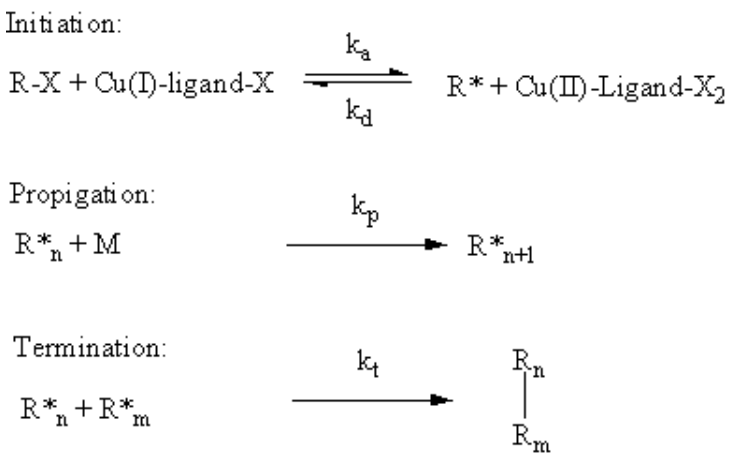


Figure 5.2: Schematic of the ATRP reaction

The ATRP reaction scheme is shown in Figure 5.2. Where k_a is the activation rate, k_d is the deactivation rate, and k_t is the termination rate. The reaction starts when a radical is formed from a halogen molecule reacting with a copper-ligand complex. The polymer propogates by reacting with a monomer. The ATRP reaction is terminated when radical molecules react.

A method for attaching an ATRP initiator is shown in Figure 5.3. A silicon oxide surface is hydroxylated and reacted with 3-(trimethoxysilypropyl)-2-bromo-2-

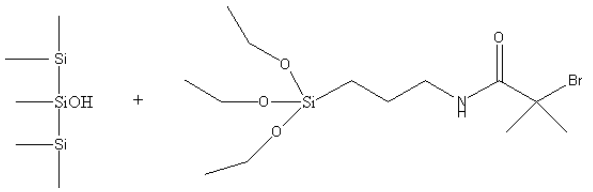


Figure 5.3: Pre-attachment of initiator to the surface of silicon (left)

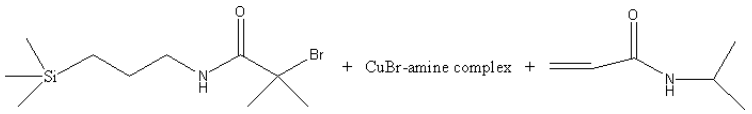


Figure 5.4: ATRP reactants

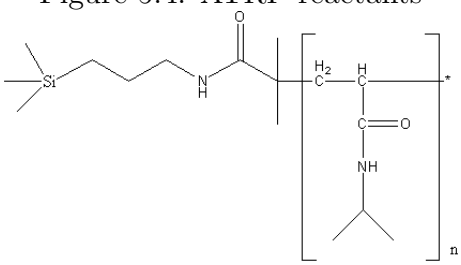


Figure 5.5: PNIPAAm grafted silicon thin film product

methylpropionate. The initiator modified surface is then placed in solution with the NIPAAm monomer and an aromatic amine catalyst, which promotes radical transfer. This is shown in Figure 5.4. The bromine leaves to form a short lived radical on the initiated surface that reacts with the NIPAAm monomer. The bromine will return to the radical and wait for the next short lived radical transfer. After many of these short lived radical transfer events the end result is a surface grown PNIPAAm film shown in Figure 5.5. The number of repeat polymer units, n, is propotional to the duration of the polymerization reaction.

The useful application of PNIPAAm is often based on PNIPAAm grafted surfaces. Surface characterization of grafted surfaces is important for understanding and controlling PNIPAAm properties. Neutron reflectivity was used to study grafted PNIPAAm LCST characteristics [105, 106]. Atomic force microscopy (AFM) was used to confirm the LCST of plasma deposited PNIPAAm [102]. Ellipsometry and

XPS are the standard techniques used to characterize PNIPAAm modified surfaces for grafted polymer height and chemical identification, respectively. Contact angle goniometry can be used to confirm the change in relative hydrophobicity, implying a change in molecular conformation of the PNIPAAm surface.

ATRP has many variables that can be manipulated to yield a thermally responsive PNIPAAm surface. The goal of this chapter is to understand the variables of the ATRP raction and characterize the resulting thermally responsive PNIPAAm polymer brushes. The methods and materials studied in this chapter will be the foundation for creating reproducable surfaces for experimention on in a later chapter.

5.2 Materials and Methods

N-isopropylacrylamide (NIPAAm) 97%, 2-bromo-2-methyl-propionyl bromide 98%, (3-amino-propyl)triethoxysilane 98%, triethylamine 99%, Cu(I)Br 99.999%, *N,N,N,N,N*-pentamethyldiethylenetriamine (PMDETA), were purchased from Sigma-Aldrich. Nanopure was produced in house and deoxygenated by bubbling nitrogen for a minimum of 2 hours per 500 mL.

Initiator Synthesis ATRP initiator, 3-(trimethoxysilypropyl)-2-bromo-2-methyl-propionate was purchased from Gelest, or 2-bromo-2-methyl-*N*-(3-triethoxysilyl-propyl)propionamide was synthesized in-house following the procedure by Mulvihill [118]. 1.50 mL (2.79 g, 12.1 mmol) 2-bromo-2-methyl-propionyl bromide was added drop wise to a solution of 2.00 mL (1.89 g, 8.55 mmol) (3-amino-propyl)triethoxysilane and 1.80 mL (1.31 g, 12.9 mmol) triethylamine in 50 mL dry dichloromethane. The solution was stirred for 14 hours and the precipitate filtered off. The solution was washed twice with dilute HCl and once with deionized water and dried with magnesium sulfate. After filtration the solvent was removed in vacuo to yield 3.01 g

of a brownish transparent oil.

Surface Preparation Silicon wafer were cut into 1 inch squares and cleaned by a HCl:MeOH solution (1:1 by vol) for 30 minutes. The wafers were then cleaned by concentrated H_2SO_4 for 30 minutes. The surface treatment followed by rinsing with copious amounts of water and dried in a stream of nitrogen.

Initiator attachment 100 microliters of ATRP initiator was dissolved in 50 mL of toulene. Slides were placed in solution and left overnight at room temperature (22 °C). Wafers were rinsed 3 times with toulene and dried in a stream of nitrogen.

ATRP reaction A solution of 1.7 M NIPAAm (5.0 grams, 44 mmol) was created where the solvent was a 25 mL mixture of MeOH/H_2O (1:1 by vol.). Cu(I)Br (7 mg , 3 μmol) and PMDETA (30 μL, 25 mg, 140 μmol) were added to the NIPAAm solution and deoxygenated by bubbling nitrogen for 30 minutes and then sealed for transfer to a glove box. Inside a glove box the wafers were immersed in the polymerization solution. The polymerization was performed at room temperature for a prescribed time. To stop polymerization, wafers were removed from the polymerization solution and rinsed three times with methanol, removed from the glove box, rinsed with methanol and then water and dried in a stream of nitrogen. The reaction could also be performed in Schlenk glassware.

Equipment Ellipsometry was done with an M-44 ellipsometer from J.A. Woolam Co. The thickness of the polymer layer was measured at least 3 times and the average taken. Sessile drop contact angles were taken with a Ramé-Hart contact angle goniometer. Temperatures were controlled with a heating ribbon and monitored by a thermocouple. The surface was modeled as a silicon substrate with an overlaying Cauchy layer, an index of refraction of 1.4 was used. XPS scans were performed with a Kratos Axis Ultra spectrometer using an Al Kα X-ray source. An electron flood gun for charge neutralization and hemispherical analyzer with eight multichannel

photomultiplier detector was employed for analysis. Three areas per sample were analyzed with a 90 degree take-off angle (TOA), 8-10 nm depth. Area of analysis was 700 x 300 microns in size. Survey spectra (low resolution wide scan) were acquired at 80 eV pass energy for four minutes. High resolution spectra were acquired at 20 eV pass energy. Fit peaks were constrained by a full width half maxium value between 1.2 and 2 eV. The C-C peak fit was further constrained to a position of 284.9 to 285.1 eV. Another constraint was done for the C-O and C=0 peak fit, 285.56 to 285.75 and 287.81 to 288.59 eV respectively.

5.3 Results and Discussion

An AFM micrograph was taken of the resulting PNIPAAm grafted silicon surface in air, shown in Figure 5.6. The surface shows a sporatic network of polymer growth. The surface roughness is about 20% of the polymer height, which is consistent with other ATRP grown PNIPAAm surfaces examined by AFM [122, 123]. The silicon substrate was a polished wafer that had a mirror finish and when measured with ellipsometry typically deviated in height by 4 Angstroms. The AFM image shows that the surface is no longer flat. Instead the topography appears to be cylindrical in nature traveling from top right to bottom left. The bright white area in the lower right quarter of the micrograph is probably a dust particle that became trapped on the polymer surface. The top area of the micrograph is much more uniform in both height and appearance.

The resulting ATRP grown surface is not very homogenous in height. ATRP chain termination between neighboring polymer chains is a semi-random event. It is proportional to chain length in that the statistical probability of two neighboring polymer chains will terminate increases as length increases. Thus, ATRP polymerization will yeild a distribution of polymer lengths [117]. The sporatic and circular

appearance of the polymer on the surface may be due to the drying process of the polymer. Attempts to image the PNIPAAm surface in water often resulted in poor image quality. The hydrated PNIPAAm was very sticky, which would produce numerous image artifacts.

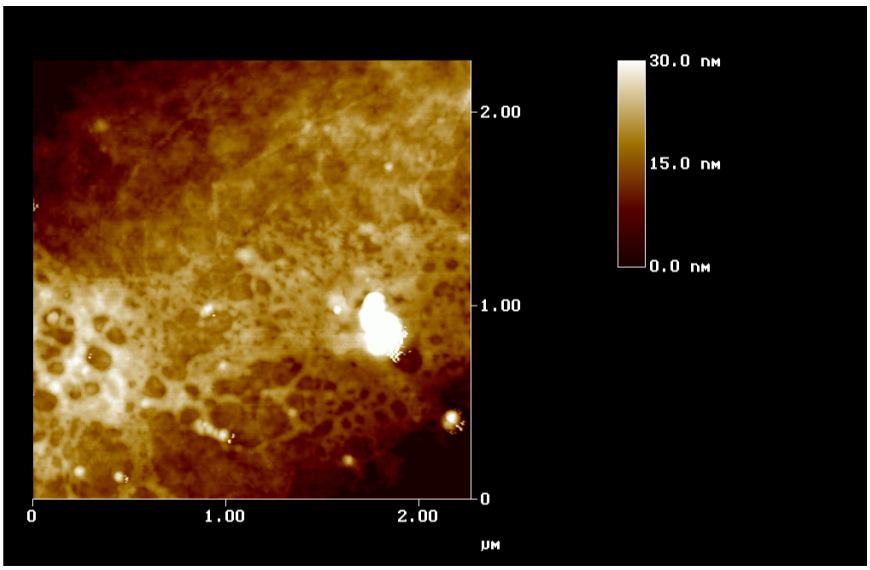


Figure 5.6: AFM micrograph in air of the ATRP grown PNIPAAm surface on a silicon wafer.

The thickness of the PNIPAAm layer, measured with ellipsometry is plotted against the polymerization time, can be seen in Figure 5.7. At time zero there is already a surface thickness which is the thickness of the initiator. The expected value is 20 Angstroms for the thickness of the initiator, in this figure the initiator thickness was 43 Angstroms. As the ATRP reaction progresses the polymer height increases, following a asymptotic curve. The model shown with the data is a kinetic model for ATRP growth [7].

As the polymer chain length increases the deviations in the measured polymer height increase. The error (calculated as the standard deviation of three measure-

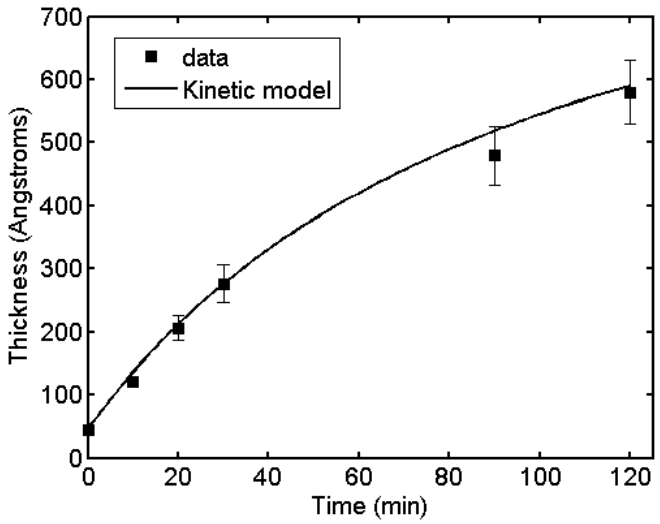


Figure 5.7: PNIPAAm thickness measured by ellipsometry as a function of polymerization time, fit is a ATRP kinetics model taken from literature [7]

ments at each time point) deviation arises from two sources, variation in polymer height and error in the fit of the ellipsometric model. The ellipsometric model produces larger deviations as the polymer thickness increases but never exceeds 10%. The index of refraction may also change as a function of polymer height leading to part of the deviation. The difference between expected initiator height and observed is the tendency of the initiator to auto-polymerize. Age of the initiator tends to be the greatest factor in both the thickness of the initial layer and later the success of the ATRP reaction. It might be that some areas of the silicon surface contain more initator molecules that others. If this is the case, the subsequent ATRP reaction will have a more patchy growth leading to areas of higher thickness than other. This hypothesis can be tested by creating a mixed SAM of silanes where the initiator surface density can be varied to observe the effect on polymer thickness.

The polymerization height data matches an ATRP surface grafting kinetics model taken from literature [7]. An assumption in the model is the reaction does not come

close to completion, and most of the reaction is stopped at low conversion by chain-chain radical termination. This is a appropriate assumption because the monomer concentration is typically a thousand fold molar excess. The extreme excess of the monomer concentration is to keep the chain-chain termination from occuring. The radical is more likely to encounter a monomer molecule by sheer quantity than a neighboring chain radical. It is important to keep in mind that the ATRP reaction has a fast backwards reaction once the radical is formed to return to the bromine terminated end group. The short lived radical is one of the reasons why ATRP reactions are more controllable than other radical polymerizations. The kinetic model is shown in Equation 5.1 [7].

$$[M]_o - [M] = \frac{[M]_o \, k_p \, [R^*]_o \, t}{1 + [R^*]_o \, k_t t} \tag{5.1}$$

Where $[M]_o$ is the initial concentration of the monomer, $[M]$ is the concentration of the intiator during the reaction, k_p is the specific rate of polymerization, k_t is the specific rate of radical termination, $[R^*]_o$ is the initial concentration of the radical, and t is the time. The change in monomer concentration, left hand side of the equation, can be directly measured as the polymerization height measured by ellipsometry. The specific reaction rates can be adjusted to fit the experimental data. The initial concentration of the radical, $[R^*]_o$, is not known but is very small for ATRP reactions. If the polymerization rate and chain termination rate are the dominant terms, fitting the data to the experiment becomes much easier. After fitting the model to the data the polymerization rate, k_p, is a hundred fold faster than the termination rate, k_t. This is because of the high concentration of monomer. It would be possible to slow down the polymer growth, by decreasing monomer concentration, at the expense of having a shorter terminal polymer length in the same amount of time. To obtain the maximum polymer chain length, the monomer concentration should be as high as possible and let the ATRP reaction continue for as long as possible.

Table 5.1: Elemental composition from XPS survey spectra of initiator surface, one sample scanned in three areas, standard deviation is less than 2%.

SAM	Si %	C %	O %	Br%
Initiator	44.1	15.7	39.7	0.5

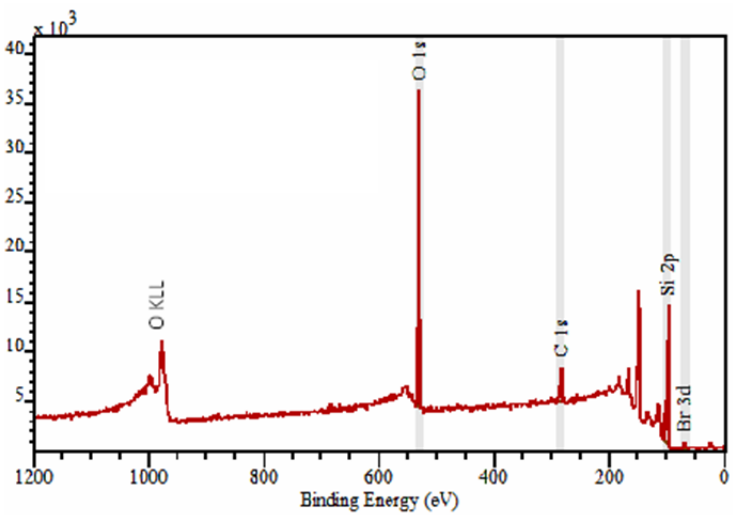


Figure 5.8: Survey XPS spectrum of the initiator self-assembled monolayer on the silicon wafer

XPS was used to confirm the chemical composition of the initator and PNIPAAm thin films. An XPS spectrum of the initiator on silica is shown in Figure 5.8. The elemental composition is given in Table 5.1. The peak at 99 eV confirms the presence of the underlying silicon substrate. The bromine 3d electrons are seen consistent in the three XPS scans at 70 eV. The carbon 1s electrons are seen at about 290 eV. A very strong oxygen 1s peak is seen at 533 eV region. The strong oxygen peak comes from the oxidized and hydroxylated silica surface. The peaks at 1000 eV come from the Auger electrons of the oxygen. This XPS spectrum is consistent with expected results, as depicted in Figure 5.3.

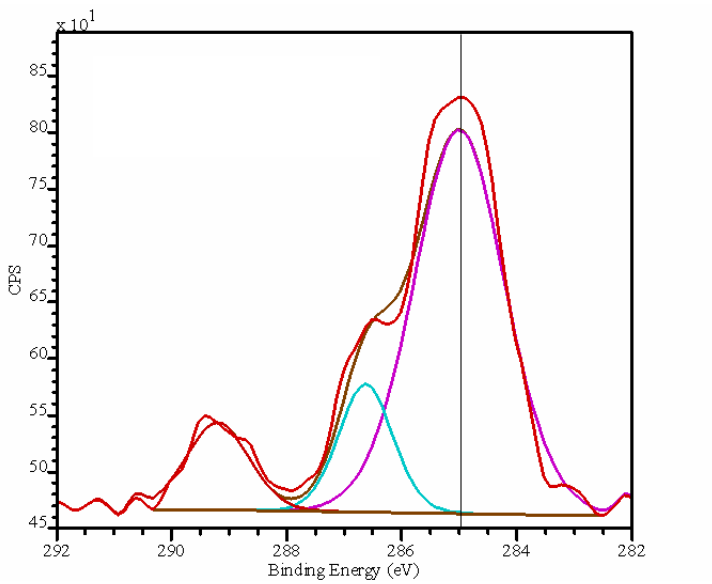


Figure 5.9: High resolution C 1s XPS spectrum of the initiator self-assembled monolayer, upper most curve. Lower curves are carbon bonding fits produced by CasaXPS analysis software.

Table 5.2: High Resolution C1s composition from XPS spectra of the initiator, one sample scanned in three areas, standard deviation is less than 2%.

Sample	C-H %	C-N %	C-Br %
PNIPAAm	73.5	16.9	9.6

A high resolution carbon 1s XPS spectrum of the initiator is seen in Figure 5.9. The composition of peaks is shown in Table 5.2. The C*-C and C*=C peaks are seen at 285.0 eV. The next peak at 286.6 eV confirms the presence of C*-N. The peak at 289.2 eV could come from the secondary carbon electrons of C*-C-O, C*-C-N, or the primary carbon electrons of C*-Br. The latter electron source is consistent with the chemical composition of the initiator. It should be noted that adventitous carbon often appears in SAMs of silica surfaces. The adventitious carbon, coming from carbon containing aerosol contamination or transfer from a carbon source, often appears in XPS spectra.

Table 5.3: Elemental composition from XPS survey spectra of initiator surface, one sample scanned in three areas, standard deviation is less than 2%.

SAM	C %	N %	O %
Initiator	75.6	12.6	11.9

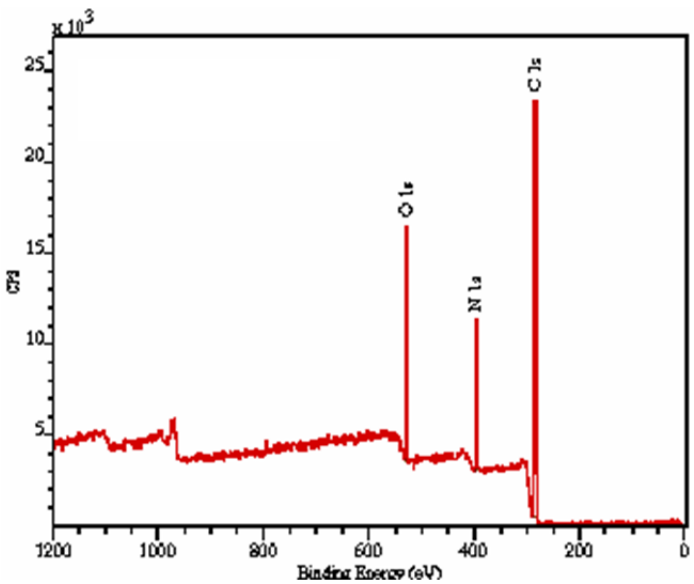


Figure 5.10: Survey XPS spectrum of PNIPAAm on the silicon wafer

The survey XPS spectrum of a PNIPAAm thin film can be seen in Figure 5.10. Elemental analysis of the XPS spectra for PNIPAAm match the predicted values of O:N:C (1:1:6) well. The elemental composition is shown in Table 5.3 with a O:N:C ratio of 1:1:6.3. The carbon, nitrogen, and oxygen 1s electrons being at 285, 398, and 531 eV, respectively.

A high resolution carbon 1s scan of the polymer surface is seen in Figure 5.11. The largest emission peak at 285 eV comes from C*-H present in the side group and the polymer backbone of PNIPAAm. The peak at 286 eV comes from the emission of the C*-N electrons, also present in PNIPAAm. The last peak at 287.8 eV comes from the N-C*=O carbon also present in PNIPAAm. If there is any halogenated carbon

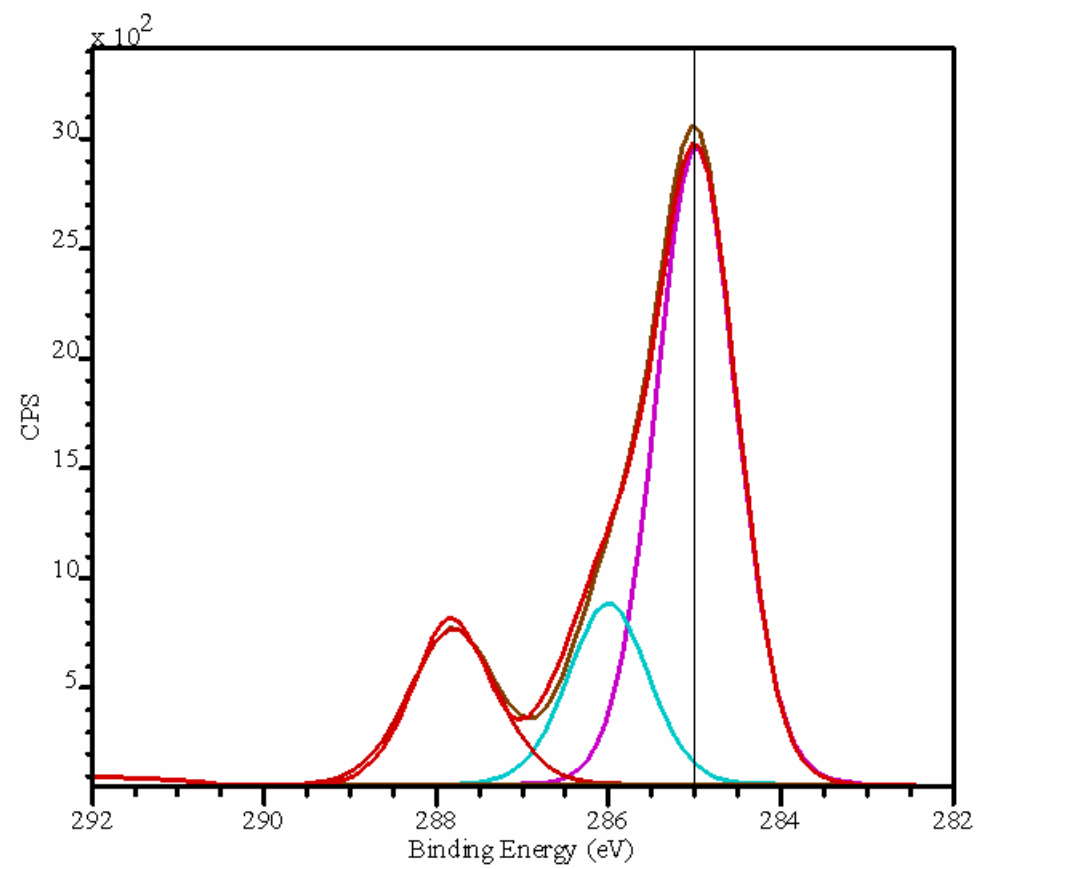


Figure 5.11: High resolution XPS spectrum of the carbon 1s peak of the ATRP grown PNIPAAm. Lower curves are carbon bonding fits produced by CasaXPS analysis software.

remaining it is not distinguishable in the spectrum. The predicted composition of the fit curves is 66.6% C-H, 16.6% C-N, 16.6% N-C=O, which differs slightly than the observed values of 63.0% C-H, 20.2% C-N, 16.8% N-C=O as shown in Table 5.4. The difference between observed and predicted is close enough to the standard deviation that it is believed to be only PNIPAAm. The sampling depth of XPS, 2 to 10 nm, is smaller than the dried polymer height of 50 nm. Thus, the chemical composition of the initiator is not observed.

Table 5.4: High Resolution C1s composition from XPS spectra of the PNIPAAm polymer, one sample scanned in three areas, standard deviation is less than 2%.

Sample	C-H %	C-N %	N-C=O %
PNIPAAm	63.0	20.2	16.8

The initiator attachment to the surface was confirmed by contact angle in addition to ellipsometric measurement. The hydroxylated silicon wafer had a contact angle averaging 15 degrees. The contact angle of the initiator SAM surface measured 80 $\pm$ 2 degrees. The static drop contact angle on a PNIPAAm film was 35° at 22 °C and varied from 60 to 80° at 40 °C depending on polymer brush thickness. The thickness values, contact angles, and thermal response are similar to those published for ATRP polymerized PNIPAAm films [5, 101, 68, 10, 103, 104, 114].

To show that the ATRP grown surface is thermally responsive, the contact angle is measured at room temperature (22 °C) and 40 °C. There are many methods of measuring contact angle: sessile or static drop, advancing and receeding angle, and captive bubble. Here the captive bubble method was used and the contact angle measurements are shown in Figure 5.12. To observe a thermally responsive surface, the absolute value of the difference of contact angle at high and low temperature was found. In the data a zero value respresents no change in the surface, signifying no thermal response. A value greater than zero implies a thermally responsive surface. The data shown in Figure 5.13, shows a thermal response for dry polymer thickness of 20 nm or greater. It should also be noted that each point on the graph was a new sample, with wafer, ATRP reaction and measurement. Zhu et al. posit that there is a critical polymer segment length necessary for PNIPAAm to give rise to favorable intermolecular interactions that give rise to an LCST [103].

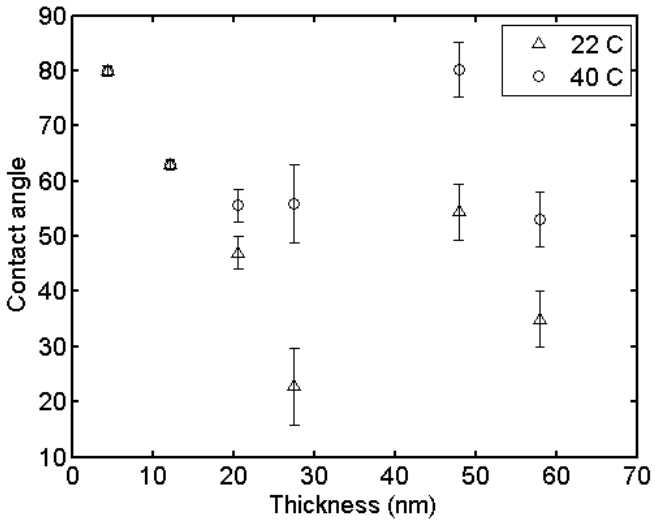


Figure 5.12: Contact angles for PNIPAAm at 22 and 40 °C measured by captive bubble goniometry.

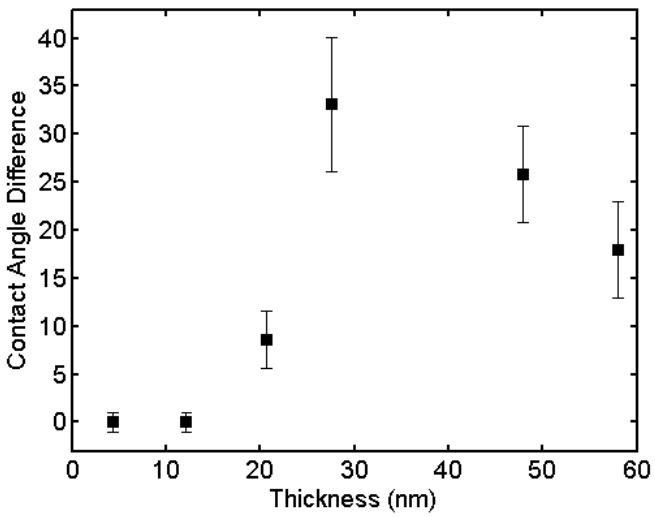


Figure 5.13: Difference in contact angle between 40 °C and 22 °C measured by captive bubble goniometry.

5.4 Conclusion

PNIPAAm was sucessfully grown from silicon wafers by ATRP. The attachment of a surface initiator was characterized by XPS, ellipsometry, and contact angle goniometry. The resulting polymer thin films were characterized by AFM, XPS, contact angle goniometry and ellipsometry. All the results were consistant with values present in the literature. The polymer brushes were shown to be thermally responsive by the change in contact angle at different temperatures. The growth rate of PNIPAAm by ATRP matched an ATRP growth model from literature. The parameters from the model were explained in order to optimize polymer growth. PNIPAAm thin films exhibit a thermal response only above a certain polymer chain length.

Chapter 6

Force Interactions with Poly(*N*-isopropylacrylamide) Thin Films

6.1 Introduction

From the literature (see review in the previous chapter) it is known that poly(*N*-isopropylacrylamide) (PNIPAAm) exhibits reversible bioadhesion. Different methods of attaching PNIPAAm to a surface give rise to different surface properties. This chapter examines the behavior and mechanical properties of PNIPAAm brushes by atomic force microscopy (AFM). AFM is a valuable tool in molecular force spectroscopy [64], surface chemistry [65, 90, 66], mechanical properties of polymeric surfaces [114, 124, 125, 126], and imaging. We hypothesized that the LCST temperature, surface stiffness, and surface free energy can be found by examination of force-distance curves obtained by AFM. To our knowledge no articles or books have been published on the mechanical properties of ATRP grown PNIPAAm thin films

via AFM.

As stated in the prior chapter, ATRP grafted PNIPAAm exhibits a LCST similar to that of bulk phase PNIPAAm. As the PNIPAAm polymer brushes collapses, it dehydrates, losing water molecules that keep the polymer brush soft and elongated. The collapsed polymer brush is then stiffer when compressed. The Young's modulus of the surface, a measure of the stiffness, can be measured before and after the LCST. The Hertz model is the most widely used model for calculating the Young's modulus by AFM [114, 124, 125]. The Young's modulus is also known as modulus of elasticity, and elastic modulus. The Hertz model is:

$$\delta = \sqrt{\frac{2}{\pi}\frac{(1-\nu^2)}{E}\frac{f_{cone}}{tan\alpha}} \tag{6.1}$$

where δ is the indentation into the surface, ν is the Poisson ratio (assumed to be 0.5), E is the Young's modulus, f_{cone} is the force of the conical AFM cantilever on the surface, α is the half angle of the cantilever.

The AFM cantilever used in the experiment is a square pyramidal cantilever. It is assumed the geometric difference between the square pyramidal tip and conical model is neglegible in this case. Estimating the Young's modulus in incremental temperature steps through the LCST will examine how the PNIPAAm polymer brush stiffness changes.

There are many methods for examining the fundamental property of free energy. Many can be done with contact angle goniometry such as those discussed in chapter 4. The methods presented in chapter 4 obtain bulk values of the surface free energy and are not very sensitive. The surface free energy can be obtained by AFM using adhesion data [39]. The adhesion data can be transformed to surface free energy via several models: the Hertz model, the Johnson-Kendall-Roberts (JKR) model [70], and the Derjaguin-Muller-Toporov (DMT) model [127], and the Maugis model

[128]. The models find an adjusted adhesion value when the surface is deformed by a spherical body. Yet, the reason PNIPAAm was choosen was because it should be a non-adhesive surface below its LCST. Thus, the above models for calculating the surface free energy from adhesion may not be applicable to PNIPAAm below its LCST. To ensure data can be obtained to calculate the surface free energy it was decided to use steric force measurements which can be easily obtained irregardless of the condition of the PNIPAAm polymer.

In addition, the use of steric force measurements can examine how the fundamental properties of the PNIPAAm surface change during the LCST. Steric forces are forces present when a molecule is compressed, like between an AFM cantilever and hard substrate. The steric forces of compression of a polymer surface have been modeled in several ways. Kaholek et al. used an inverse exponential function, including the ionic double layer decay length, in combination with the Derjaguin approximation to obtain the free energy profile [129]. Self-consistent field theory was used to model polymer compression and an exact analytical solution for weak volume exclusion was given [130, 131]. Another steric compression model is the wormlike chain model, also known as the Porod-Krakty model [132]. The problem is that many of these models are complex and require computational calculation. A simplier model that relates thermodynamics and steric forces is needed.

Butt et al. proposed a model that reduced to an exponential with prefactor for a dense polymer brush [132, 133]:

$$f \approx 50 k_B T \Gamma^{3/2} exp\left[2\pi Z/L_o\right] \qquad 0.2 \leq Z/L_o \geq 0.9 \tag{6.2}$$

where f is force, k_B is the Boltzmann constant, T is the absolute temperature, Γ is the grafting density, Z is the distance between the two surfaces, L_o is the equilibrium length of the polymer brush. This emperical fit was designed for AFM measurements performed with a conical cantilever and a polymer surface. It is quite powerful in

that it allows the polymer thickness, and surface grafting density to be extracted. It is limited in usage in that it is only valid for a specific region of polymer compression and it does not relate to any thermodynamic or molecular model.

The most heavily utilized model for steric compression is the Alexander-de Gennes model [134, 135, 136]. The Alexander-de Gennes model is valid for any polymer-polymer steric interaction, it is also simple to calculate. The polymer surface is approximated by circular 'blobs.' When two polymer surfaces are pressed together the blobs undergo compression which changes their interaction energy. The model then relates the Helmholtz free energy to the interaction distance. The Alexander-de Gennes scaling theory is,

$$F(Z) = K_a \rho_a \left[\left(\frac{L_o}{Z} \right)^{(9/4)} - \left(\frac{Z}{L_o} \right)^{(3/4)} \right] \tag{6.3}$$

K_a is often left as a prefactor for fitting to experimental data, although it can be expanded to

$$K_a = \frac{16 k_B T \pi L_o}{35} \tag{6.4}$$

k_B is Boltzman's constant, T absolute temperature, ρ_a is the number of chains per surface area or polymer graft density, L_o the unperturbed polymer brush length, Z is the distance between the two surfaces. The first term within the brackets of Equation 6.3 comes from the osmotic pressure, which increases as the two surfaces approach each other. The second term accounts for the decrease in elastic energy as the chains are compressed.

The data from a very important steric force experiment performed by surface forces apparatus (SFA) is shown in Figure 6.1. The data shows that regardless of polymer size the force-distance curve of the two polymers in compression will have a similar shape when plotted in a log-linear format. It should follow that any

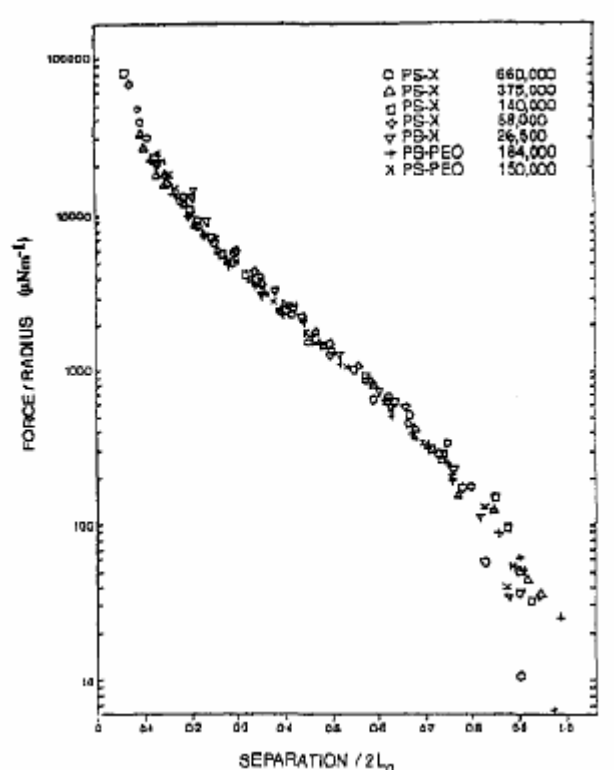


Figure 6.1: Force-distance plot of polymer surfaces of various lengths taken with SFA, taken from [8].

theoretical model for polymer compression of two flat surfaces should match the data in Figure 6.1. Figure 6.2 shows a close match between their force-distance data and the theory of Alexander-de Gennes. The close fit between model and data has set the Alexander-de Gennes model as the benchmark model for steric polymer compression.

The Alexander-de Gennes theory is applicable for two flat plates both covered with polymer. In order to apply the Alexander-de Gennes theory, a modification must be made to the geometry of the AFM cantilever. The modification is,

$$F_{\Delta}(Z) = 8L_o^2 tan\theta \int_Z^{\inf} (Z - Z_{TS})F(Z)dZ \tag{6.5}$$

where F_{Δ} is the force of the pyramidal cantilever on the flat surface, L_o is the

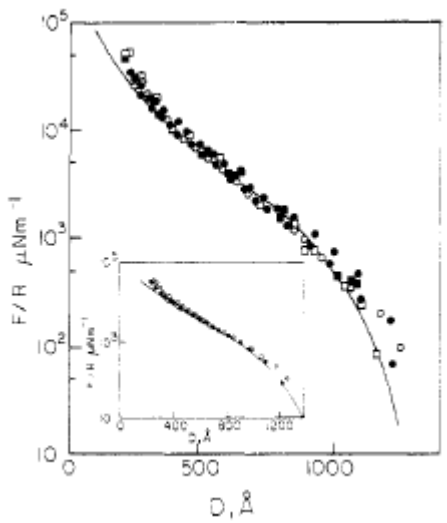


Figure 6.2: Force-distance plot of the various polymer lengths shown with the model of Alexander-de Gennes, taken from [8].

unperturbed polymer length, θ is the half angle of the pyramidal cantilever, Z is the distance, Z_{TS} is the tip-sample distance, F is the force measured by the AFM [9]. With this modification the data from AFM can be compared to the Alexander-de Gennes model. How the Alexander-de Gennes model can be used to obtain fundamental properties is later in this chapter.

Density functional theory (DFT), was used by Mendez et al. to examine the steric interaction between a hard wall and a model PNIPAAm brush [137]. In DFT another parameter, L the perturbed polymer length, is introduced. McCoy and Curro used density functional theory to show that L and L_o are not the same [138]. As Z approaches L_o it perturbs the polymer chain length, therefore it is more accurate to use L in calculations. Under sufficient force Z and L are nearly indistiguishable, the force at which the two variables can be approximated as one is not known. A schematic illustration of the variables used in density functional theory and the AFM setup is shown in Figure 6.3.

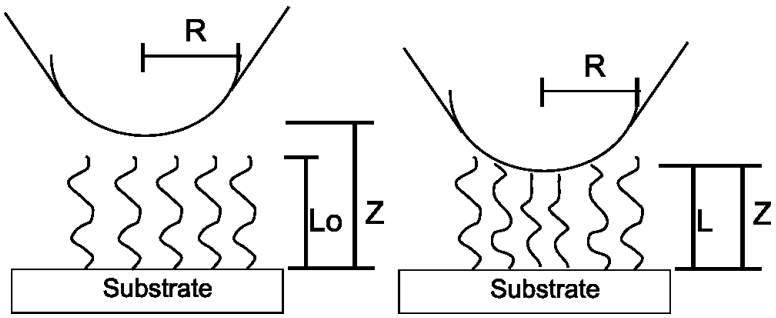


Figure 6.3: Illustration of the variables and conditions in the force-distance experiment

McCoy and Curro compared DFT to the model of Alexander-de Gennes and found very close agreement [138]. They developed a transformation so that the two models could be related. Equation 6.6 is an empirical transformation of the L_o of Alexnader-de Gennes model into the L of density functional theory.

$$\frac{L}{L_o} = tanh\left(Z/L_o\right)\left\{1 + 0.60\left(\frac{Z}{L_o}\right)^4 exp\left[-1.5\left(\frac{Z}{L_o}\right)^2\right]\right\} \tag{6.6}$$

An important factor for PNIPAAm chain conformation is solvent condition. It is possible to relate DFT to the solvent condition. Intermolecular interactions between polymer chain segments and surrounding solvent molecules have an associated energy of interaction which can be positive or negative. For a good solvent, interactions between polymer segments and solvent molecules are energetically favorable, and will cause polymer coils to expand. For a poor solvent, polymer-polymer interactions are preferred, and the polymer coils will contract. The quality of the solvent depends on both the chemical compositions of the polymer and solvent molecules and the solution temperature. ν is defined as the condition of the solvent. For a good solvent, interactions between the solvent and polymer are energetically favorable causing the polymer to extend. For a poor solvent, intermolecular self-interactions are favorable causing the polymer to collapse in on itself. A theta solvent is a condition in between the two. For a good solvent ν is 3/5, for a theta solvent, 1/2, and 1/3 for a poor

solvent [139]. The resulting Alexander-de Gennes model, after insertion of the good solvent condition and geometric transformation for square pyramidal cantilever is,

$$F_{\Delta} = -8L_o^2 tan\theta K_a \rho_a \left[\frac{4}{5}\left(\frac{L_o}{Z_{TS}}\right)^{(5/4)} + \left(\frac{Z_{TS}}{L_o}\right)^{(7/4)}\right] \tag{6.7}$$

The same procedure is done with the theta solvent condition for the Alexander-de Gennes model,

$$F_{\Delta} = -8L_o^2 tan\theta K_a \rho_a \left[2\left(\frac{L_o}{Z_{TS}}\right) - \frac{3}{2}\left(\frac{Z_{TS}}{L_o}\right)^{3}\right] \tag{6.8}$$

the change in exponents within the brackets, which indicates a change in behavior of osmotic and elastic energies.

The AFM force-distance data can now be fit to the model. The condition of the solvent can be examined with the Alexander-de Gennes model. McCoy et al. derived the Alexander-de Gennes model in terms of the solvent condition [138],

$$\beta F = \rho_a^{3/2} K \left[\left(\frac{L_o}{Z_{TS}}\right)^{\frac{3\nu}{3\nu-1}} - \left(\frac{Z_{TS}}{L_o}\right)^{\frac{4\nu-1}{3\nu-1}}\right] \tag{6.9}$$

$$\beta = \frac{1}{k_B T} \tag{6.10}$$

Keep in mind that the surface free energy can be found by integrating the force with respect to distance resulting in,

$$\beta A = L_o \rho_a^{3/2} K \left[(3\nu - 1)\left(\frac{L_o}{Z_{TS}}\right)^{\frac{1}{3\nu-1}} - \left(\frac{3\nu-1}{4\nu-1}\right)\left(\frac{Z_{TS}}{L_o}\right)^{\frac{4\nu-1}{3\nu-1}}\right] \tag{6.11}$$

where A is the Helmholtz free energy.

The above equations are now setup such that the free energy can be obtained from force-distance data obtained by AFM. The same equations can be used to examine the solvent condition with respect to the temperature of the experiment.

6.2 Material and Methods

Materials The same materials, and methods were used to create the PNIPAAm surface as described in the previous chapter.

Atomic Force Microscopy measurements Force-distance measurements for the soft press section were carried out with a modified Veeco Nanoscope IIIa atomic force microscope on ATRP grown PNIPAAm films in a standard fluid cell filled with deionized water. Tip movements and data collection were automated with Labview software custom-written by David Keller. Spectral densities of the AFM cantilever were acquired in air before the experiment. PNIPAAm coated wafers were cut and placed on a J type scanner. An O-ring and fluid cell containing the AFM cantilever was then set on top of the sample. Degassed DI water was injected into the fluid cell and the film was allowed to equilibrate with the water for 30 minutes. The AFM cantilever was moved toward the sample surface in discrete 2 nm steps with a dwell time of 100 milliseconds per step. Cantilever deflection was recorded and averaged, 100 data acquisitions at each step, until tip-sample forces caused a deflection by 10 nanometers, after which the cantilever was withdrawn from the surface in the same manner (discrete 2 nm steps with average deflection recorded at each step). The deflection detector was calibrated by taking force curves on a bare silica surface, and the piezoelectric positioners were calibrated against known standard samples. The vertical position data was transformed to true tip-sample distance by adding the value of the vertical position to the value of the tip deflection at each point. Tip-sample force was calculated using a spring constant of the cantilever of 0.02 N/m as provided by the manufacturer.

Force-distance curves for the hard press section were performed similarly as above. A modified Veeco Nanoscope IIIa atomic force micrscope was to collect data with Veeco software version 6.1. The sample set into the fluid cell as before. A silicon

tapping mode cantilever with a spring constant of 40 N/m was used for all force distance experiments. Force distance curves were obtained with a 2000 nm sweep size, sweep rate of 0.1 Hz, and proceeded until AFM detector saturation.

6.3 Results and Discussion

A first attempt at modeling the polymer properties was made with a soft cantilever and using the AFM to press gently, no greater than five nanoNewtons. This section is called 'soft press.' Another attempt was made to obtain a full force-distance curve matching that found in literature. A stiffer cantilever was used to press until AFM detector saturation, several microNewtons, this experiment was called 'hard press.'

6.3.1 Soft press

The distance coordinate measured with AFM is cantilever deflection and not the distance between the cantilever and the surface at the base of the PNIPAAm film. The separation distance can not be measured directly because the AFM cantilever can not be pressed into the underlying solid surface to find the zero distance reference point. Therefore, the fitting procedure requires that we add an offset (x_{offset}) to the x-axis AFM data (x_{afm}) resulting in, $Z = x_{afm} + x_{offset}$. The force-distance data after this modification is shown in Figure 6.4. This is not the only method for calculating the x-axis. Another method will be presented in the hard press section.

The solid curve in Figure 6.5 presented with the force-distance data is Equation 6.7. To estimate the wet film thickness at 20 °C, we plotted the AFM data and then adjusted three parameters until we obtained agreement with the model of Alexander-de Gennes. The semi-log plot of the AFM data shows a sharp drop at large distances which we suspect might be due to slight attractive interactions between the bare AFM

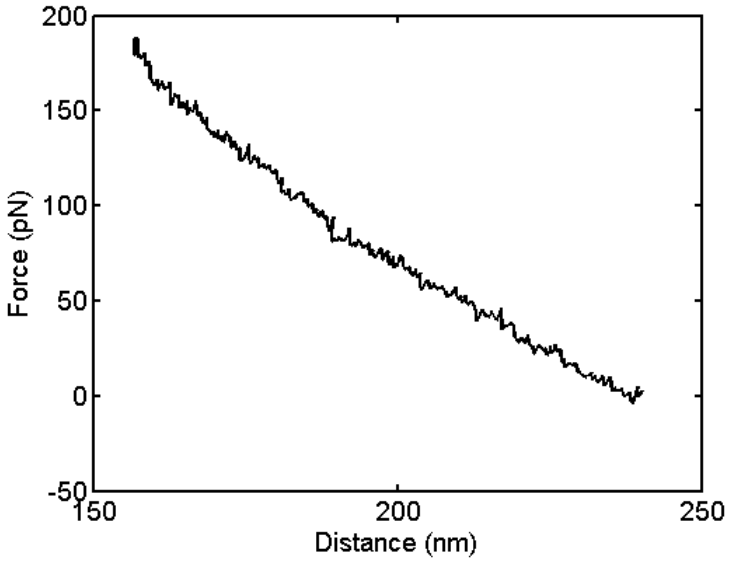


Figure 6.4: AFM data showing the compression of the PNIPAAm film after modification of the x-axis to show Z

tip and the tethered PNIPAAm chains encountered during approach of the tip. Recall that neither DFT nor the Alexander-de Gennes model account for attractive forces. Since we want to plot the force as a function of Z/Lo, we must adjust L_o to shrink or expand the range, and we must also multiply the AFM force data by a constant, K_a, as was done by Taunton et al. [8]. Thus, the three adjustable parameters are x_{offset}, L_o and K_a, which we found, through trial and error, to be 250 nm, 257 nm and 0.002 respectively. To obtain a more reliable fit, a statistical algorithm could be implemented to find these three parameters by minimization of the errors. Thus, the wet film thickness is estimated to be 257 nm. For this PNIPAAm film, the dry thickness was measured with ellipsometry to be 48 $\pm$ 4 nm, making the dry to wet thickness swell ratio (1:5.3) for our polymer brushes. Tu et al., who synthesized terminally anchored PNIPAAm films in a manner similar to us, used environmental ellipsometry to find the dry to wet swell ratio of (1:4) [123]. Kaholek et al. using AFM and fitting to a height model found the swell ratio to be (1:2.6) for ATRP

grown PNIPAAm films from SAMs [129]. Although our films and those of Tu et al. and Kaholek et al. have some similarity in the synthesis scheme, more than likely there are considerable differences in the polymer molecular weight, intermolecular crosslinking and surface coverage of the films. Since the swell ratio depends on these two parameters, we don't expect quantitative agreement.

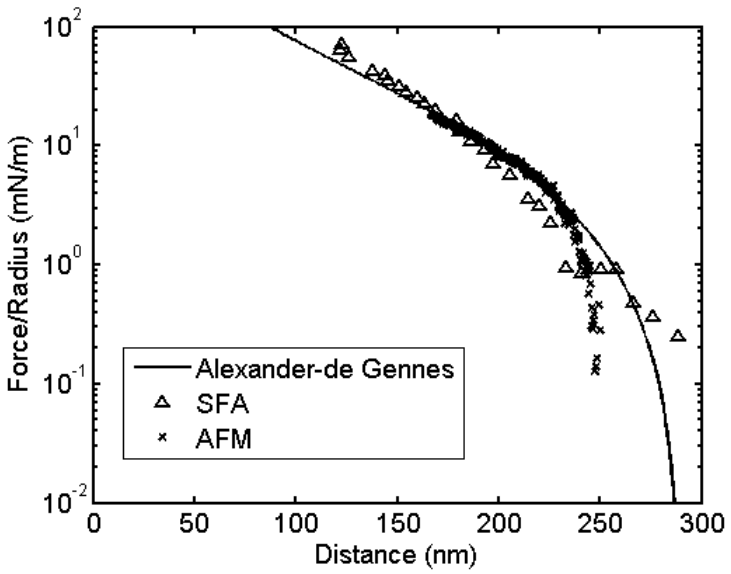


Figure 6.5: Force-distance curves at room temperature for AFM, x, SFA, triangle, and de Gennes theory, solid line [9, 10].

As a further test of this method to estimate the wet film thickness using Alexander-de Gennes model, we analyze the surface force apparatus (SFA) data reported by Plunkett et al. for similar ATRP grown brushes [10]. Unlike in AFM, SFA uses an optical interference method which can be used to obtain the separation distance, Z, therefore, we do not need to fit for x_{offset}. This leaves us to fit for L_o and K_a which we found to be 235 nm and 0.013. The value of L_o Plunkett et al. found by fitting with Equation 6.3 was $L_o = 274$ nm and the experimentally measured L_o was 269 nm. The discrepancy between the two values of L_o might be attributed to fact that we plotted force versus Z/Lo (while they used Z) and because the criteria for fitting

the data is somewhat arbitrary.

The model curves are very similar to the force-distance data presented. It is at larger separations of the surfaces that the models do not agree well and have dissimilarities, since at larger distances attractive forces substract from the models accuracy. The AFM cantilever is more sensitive to attractive forces than the crossed-cylinders used in SFA. Thus deviation from SFA force-distance data and models at larger separation is expected.

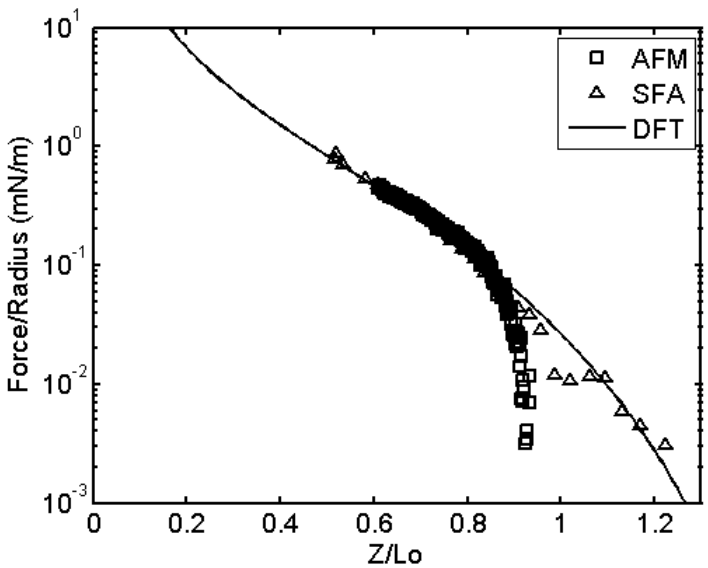


Figure 6.6: Force-distance curves at room temperature for AFM, square, SFA, triangle, and density function theory, solid line [9, 10].

In order to confirm that the polymer brushes were thermally responsive, a measure of the surface stiffness is needed. The force-distance curves for temperatures above and below the LCST on the PNIPAAm brushes are shown in Figure 6.7. Zero distance was set in the force-distance data to initial contact with the polymer brushes. As the temperature increases so does the slope of the force-distance curves. This is as expected, as the polymer collapses and becomes stiffer the slope of the force-distance curve increases.

To further examine the thermal response fo the polymer brushes, each of the PNIPAAm force curves was fit to a polynomial and then the derivative of the polynomial was evaluated at a force of 150 pN, selected arbitrarily. The derivative of the force curve reflects the polymer stiffness of the PNIPAAm brushes. The average derivative is plotted against temperature in Figure 6.8. The error in the graph is the standard deviation of multiple force curves. The minimum number of force curves at each temperature was 5 and maximum was 10. Not every force curve was considered, only force curves with continous curves, and had a single peak value were considered for data processing. The maximum force used was 5 nN. Another method for examining surface stiffness will be discussed in the hard press section.

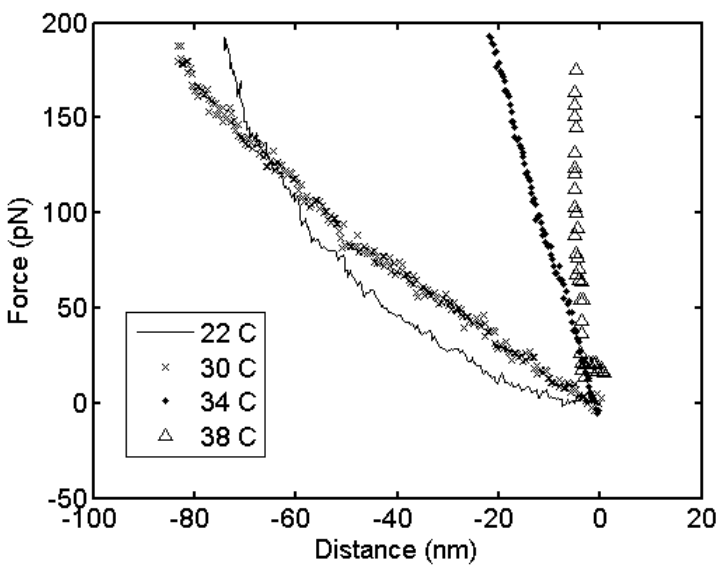


Figure 6.7: Force-distance curves on the PNIPAAm brushes at various temperatures. Force-distance curves at 26, 32, and 36 °C have been omitted for clarity.

The slope of the force-distance curves only fluctuates within error from 22 to 32 °C. There is a very noticable change in the polymer stiffness at 32 to 34 °C. This coincides with the LCST of surface grafted and bulk PNIPAAm[91, 92, 93, 94, 95, 114, 10]. It also agrees with conceptual knowledge that a collapsed dehydrated

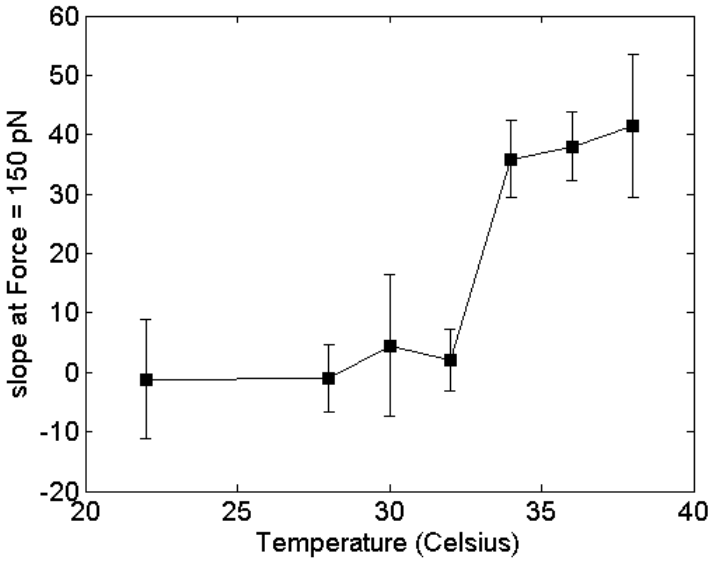


Figure 6.8: Slope of the force distance curve at 150 pN as a function of temperature measured by AFM soft cantilever

polymer layer is going to be stiffer than an extended hydrated polymer layer. Above 34 °C the polymer stiffness continues to increase slightly. It is possible that not every polymer brush exhibits a LCST at 32 to 34 °C, but brushes continue to collapse and dehydrate as temperature continue to increase.

6.3.2 Hard press

In order to better examine the force-distance curves the data must be corrected for the true tip-sample distance. The recorded values from the AFM are the piezoelectric z-distance and z-distance deflection of the cantilever. What is desired is the true tip-sample distance. The data given by the AFM can be transformed by the following relation,

$$Z_{TS} + L = Z_{AFM} + Z_C \tag{6.12}$$

where Z_{TS} is the tip-sample distance, L is the thickness of the polymer layer, Z_{AFM} is distance traveled by the piezo stepper, Z_C is the cantilever deflection. Figure 6.9 shows a schematic of the experimental system with notation. θ is the angle between the faces of the square pyramidal cantilever.

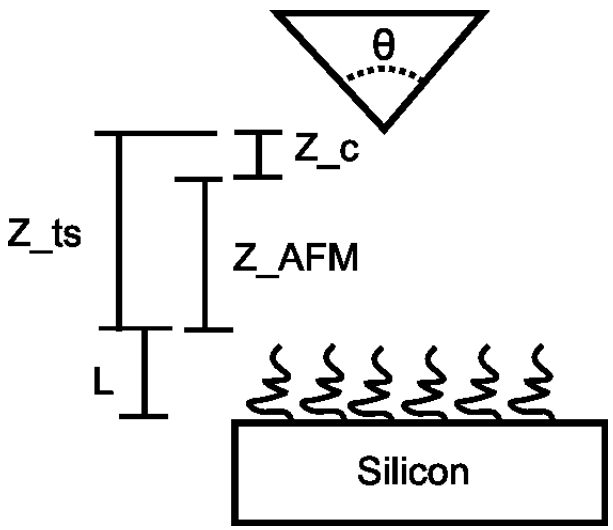


Figure 6.9: Schematic showing the notation of the force distance experiments on PNIPAAm

PNIPAAm Young's Modulus

In order to confirm that the PNIPAAm was still exhibiting a LCST, the Young's modulus of the surface was examined. A force distance curve was obtained on a silicon control sample along with the force-distance curves at the various temperatures above and below the LCST. The difference between the control surface and PNIPAAm surfaces above and below the LCST is plotted in Figure 6.10.

The force-distance data plotted in Figure 6.10 has been corrected for tip-sample distance with Equation 6.12. The force-distance curves were aligned to zero distance at first contact with the surface. The indentation of the PNIPAAm surface was calculated from the difference between the hard glass surface and the PNIPAAm surfaces at the various temperatures. The cantilever deflection is greatest for the

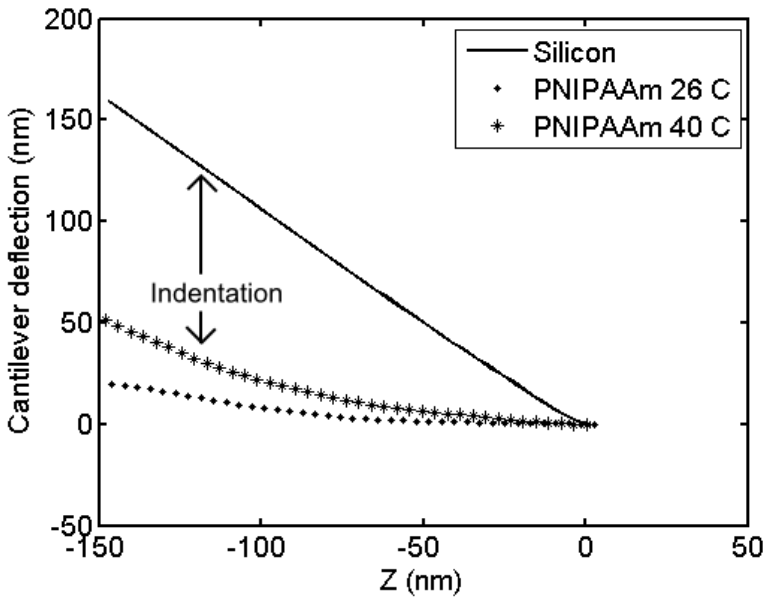


Figure 6.10: Force distance curves showing indentation into the PNIPAAm surface

stiffest surface. The collapsed PNIPAAm polymer at 40 °C presented a greater cantilever deflection implying a stiffer polymer brush than the extended polymer brush at 26 °C.

The indentation into the polymer surface can be calculated from the data in Figure 6.10 by subtracting the cantilever deflection of the polymer from the cantilever deflection of the hard surface. With the indentation data, the Hertz model can be applied and the Young's modulus of the surface can be calculated. The resulting fit of the Hertz model to the AFM force-distance curves at 40 °C and 26 °C are shown in Figure 6.11.

The Young's modulus was obtained by the best fit of the data to the model. The Poisson ratio was assumed to be 0.5. The fit of the model to the force-distance curves is quite good. There is deviation from the model as the force increases. This is likely due to the displacement of the polymer brushes by the AFM cantilever. The Hertz

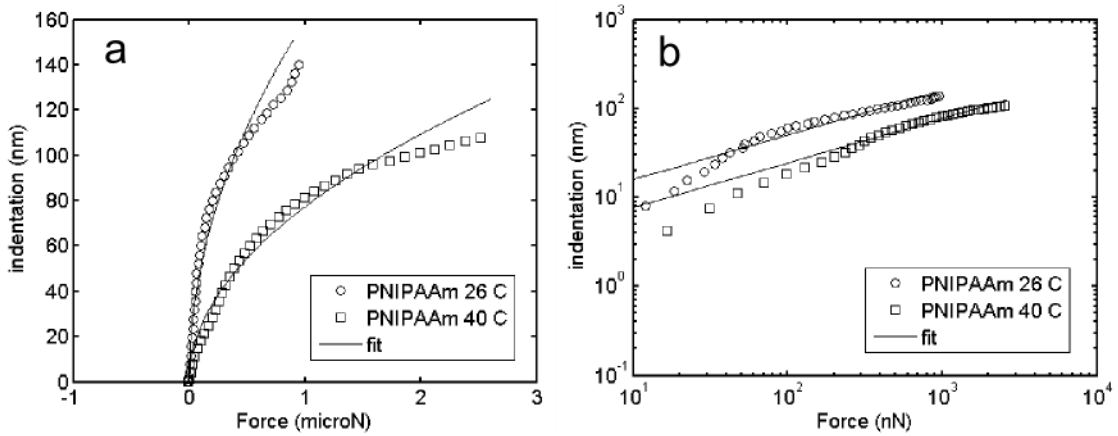


Figure 6.11: a) Fit of the Hertz model to the force-distance data to evaluate the Young's Modulus of the PNIPAAm brush. For easier comparison the data in Figure 6.11a) plotted log-log in b).

model assumes the surface continues to compress under force without displacement.

The Young's modulus of the PNIPAAm polymer brushes was calculated for all the force-distance curves at the various temperatures. The data is plotted in Figure 6.12. The Young's modulus of the PNIPAAm surface is about 80 MPa at 26 °C. The Young's modulus of the surface does not change until 35 °C were the modulus changes to a little more than 350 MPa. The change in Young's modulus confirms the surface is thermally responsive. The error present in the data comes from the many steps in processing the data. The largest source of error is the unknown value of the spring constant of the AFM cantilever, which is 30%. The other sources of error, typically 1 to 2 % are: the voltage to distance conversion, curve alignment on both x and y axis, and curve to curve deviation. It has been shown that the modulus of bulk PNIPAAm can change by a factor of 10 or more above and below the LCST [92]. This is far from the change of a factor of 100 reported by Matzelle et al., who reported a Young's modulus of a free standing PNIPAAm gel at 0.00283 MPa swollen and 0.183 MPa above the LCST [124]. Plasma deposited PNIPAAm on

a silicon wafer has a much larger modulus of 0.185 MPa and 1.592 MPa below and above the LCST [114]. The Young's modulus differs depending on PNIPAAm thin film deposition method. Polystyrene brushes grafted to a silicon surface, examined by dynamic AFM measurements in water, gave a dynamic modulus similar to my results, 150 MPa [11]. For ease of comparision these values, along with other relevant values, are shown in Table 6.1.

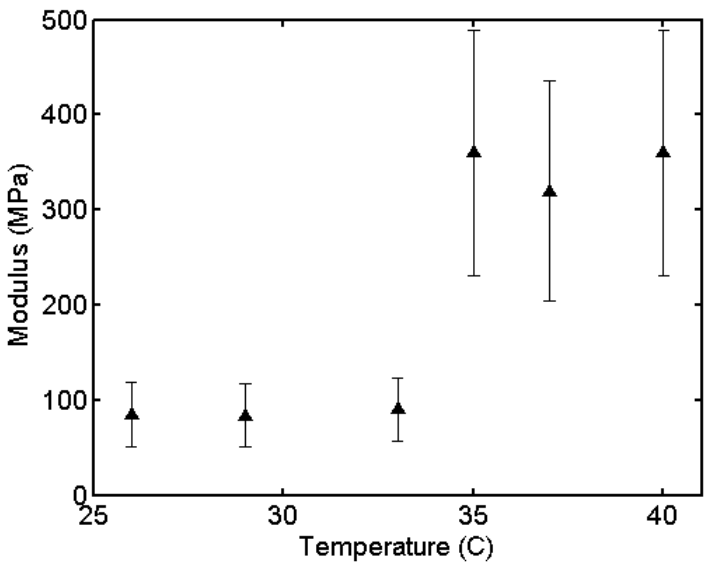


Figure 6.12: PNIPAAm Young's modulus calculated from the Hertz model as a function of temperature. Error bars are the sumation of error in all the data processing steps.

The Young's modulus is a measure of the elasticity of the surface. Cross linked polymers would have a larger modulus than that of polymer brushes. ATRP grown PNIPAAm does not result in much polymer crosslinking, thus a lower modulus would be expected. There is another factor which influences the Young's modulus and that is polymer brush displacement. ATRP grown polymer brushes would only be cross-linked at the polymer terminus, from chain-to-chain radical termination. The resulting polymer brush is much more easily displaced by external forces. The

Table 6.1: Values of Young's Modulus relevant to PNIPAAm thin films

Material	Young's Modulus (MPa)	Source
Silicon	150,000	[140]
Glass	65,000	[140]
polystyrene brushes in water	1,500*	[11]
dry polymer brushes	1,000	[141, 142]
ATRP grown collapsed PNIPAAm brushes	350	experiment
polystyrene brushes in toulene	150*	[11]
ATRP grown extended PNIPAAm brushes	80	experiment
plasma PNIPAAm collapsed	1	[114]
plasma PNIPAAm extended	0.2	[114]
collapsed PNIPAAm gel	0.2	[124]
hydrated PNIPAAm gel	0.003	[124]

* is the dynamic modulus
found by oscillating AFM measurements

modulus of the polymer brushes is less than expected because the brushes displace under the force of the AFM cantilever. As the AFM cantilever continues to press into the polymer brushes, it encounters higher resistance forces as the polymer anchors and surface resist conpression. This description of brush displacement is shown in Figure 6.13, which shows AFM modulus data of a polystyrene brush in a good solvent, toluene. The same figure also shows that the dynamic modulus of a polymer brush in a good solvent is a function of force, or distance compressed into the polymer brush. As the AFM cantilever presses harder into the surface the dynamic modulus continues to change until a terminal value of 3,000 MPa. Thus, a hard press into the polymer will displace polymer brushes resulting in a Young's modulus closer in value to the modulus of the substrate than a free standing polymer gel.

Examining the force-distance curves in a log-linear scale presents an interesting phenomenon. A single force for each temperature below the LCST is plotted log-linear in Figure 6.14. On the y-axis the force is divided by the radius of the cantilever,

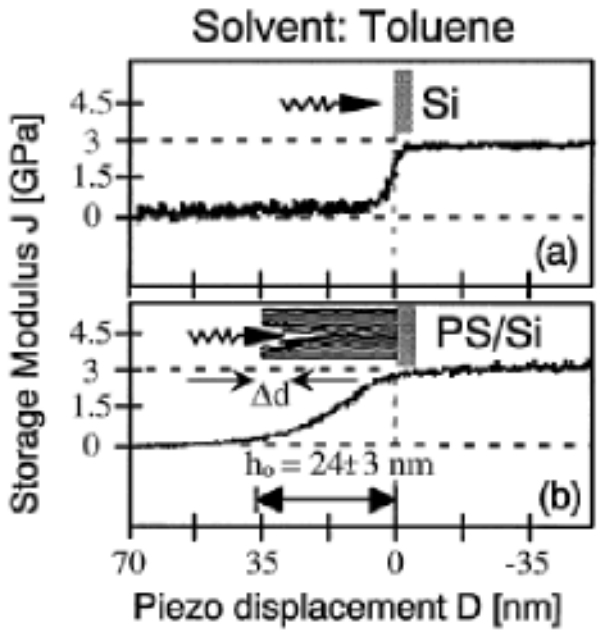


Figure 6.13: Schematic and modulus of polystyrene brushes in a good solvent taken by oscillating AFM force measurements taken from Overney et al. [11].

10 nm, doing this presents the force in units similar to surface energy. This is a standard way to normalize a force curve [10, 103, 114, 124, 125, 126, 8]. Most of the curves appear to have the same shape. At large distances the curves drop to zero force, which agrees with logic of tip-sample separation. The distance at the asymptotic force limit can be taken as the unperturbed polymer brush length, L. The unperturbed brush length is different for each curve because the force-distance measurement was not taken in the same place twice. From chapter 5 it is known that the polymer surface deviates in height across the silicon surface. Therefore the distance at the asymptotic force limit will deviate. The slope of the force-distance curve is very similar between the various curves below the LCST. As the force increases all the force-distance curves go to a steep slope at very small distances.

The force-distance curves above the LCST, 35 °C in this case have a different shape than those at temperatures below the LCST. The force-distance curves are

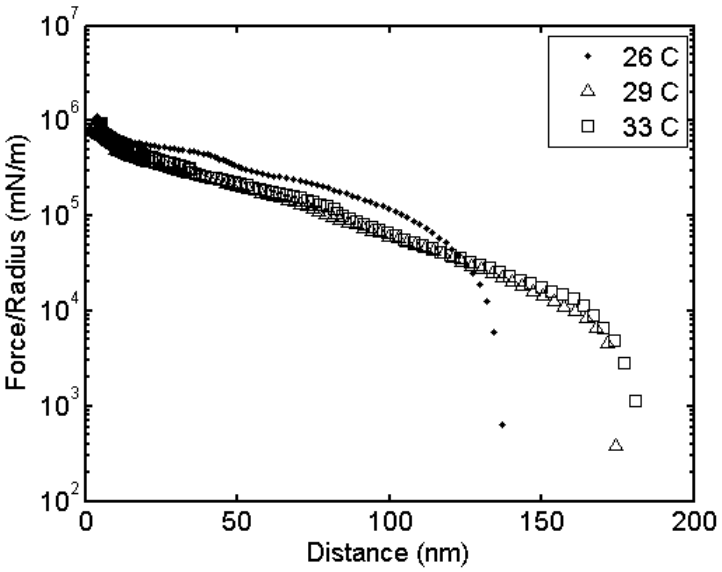


Figure 6.14: PNIPAAm force-distance curves for temperatures below the LCST.

shown in Figure 6.15. Again the force is divided by the cantilever radius. At large distances the force goes to zero. There is a distance where an asymptotic line exists where the force becomes non-zero. It is not fully understood as to why the force has an asymptotic force profile at that distance. A more gradual transition is expected as the polymer compresses. The slopes of the force-distance curves are very similar indicating a similar yield of the polymeric surface beneath the cantilever. At larger separation distances there is a interesting behavior to the curve, this will be explained when compared to a model. This is the first time force-distance curves have been examined using a log-linear plot to confirm the LCST of PNIPAAm.

To assertain the condition of the solvent for the PNIPAAm polymer brushes, the data is presented with the Alexander-de Gennes model with the good solvent condition, Equation 6.7, shown in Figure 6.16. The model curve provides a good fit to the experimental data. The data were fit by adjusting the variables K_a, and L_o. The two slopes of the curves are very similar, implying the behavior of the

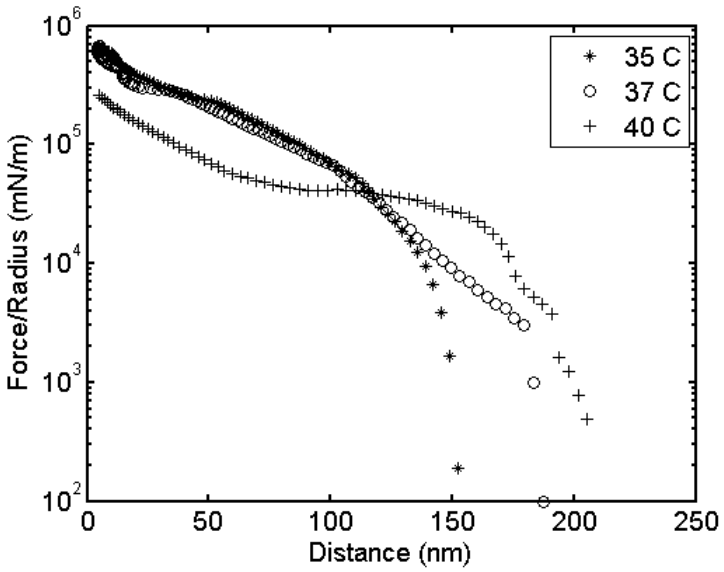


Figure 6.15: PNIPAAm force-distance curves for temperatures above the LCST.

compressing PNIPAAm polymer brush is predicted by the Alexander-de Gennes model with the condition of a good solvent. The good solvent implies the polymer brushes are extended, which is consistent with has been observed for PNIPAAm polymer brushes when hydrated [105, 137, 98]. The deviation at very small distances is believed to arise from displacment of the polymer brushes by the AFM cantilever rather than compressing them ideally.

One of the conditions of the Alexander-de Gennes model is that both surfaces are covered with polymer. This is not the case when the AFM cantilever is first placed in the fluid cell. It is believed that the AFM cantilever becomes coated with polymer after the first force-distance curves. The maximum force exerted by the AFM is enough the break the polymer bonds and leave some polymer physically adsorbed onto the AFM cantilever. Thus, for the second force-distance curve in a new location the PNIPAAm brush will encounter an AFM cantilever with physically adsorbed polymer on the surface. The physically adsorbed polymer behaving similarly to that

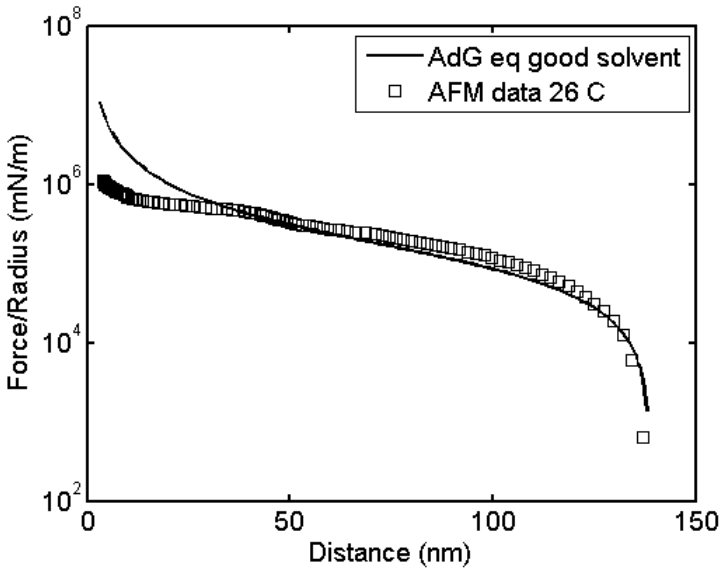


Figure 6.16: PNIPAAm force-distance curve at 26 °C shown with the Alexander-de Gennes model with good solvent condition.

of the ATRP grown brush.

The Alexander-de Gennes model with the theta solvent condition, Equation 6.8 was plotted against the AFM force-distance data for a temperature above the LCST, shown in Figure 6.17. The data and model show some similarities including: curve slope, polymer brush length, and response at small distances. Again it is believed that the experimental data at very small distances is not behaving according to the ideal compression predicted by the Alexander-de Gennes model. It is not fully understood as to the nature of the force-distance curve at large distances. It is hypothesized that the solvent condition may be a value between that of a good and theta solvent. It may also be that the polymer brushes may be exhibiting both solvent conditions. At the end of the polymer brush, the solvent condition resembles the good solvent. Conversely, while at the base of the polymer brushes, the solvent condition is more like the theta solvent condition. It is still believed that the examination of the force-distance data using a log-linear plot, allows the factor of solvent condition

to be examined as it is a contributing factor to the overall problem of bioadhesion to stimuli responsive surfaces.

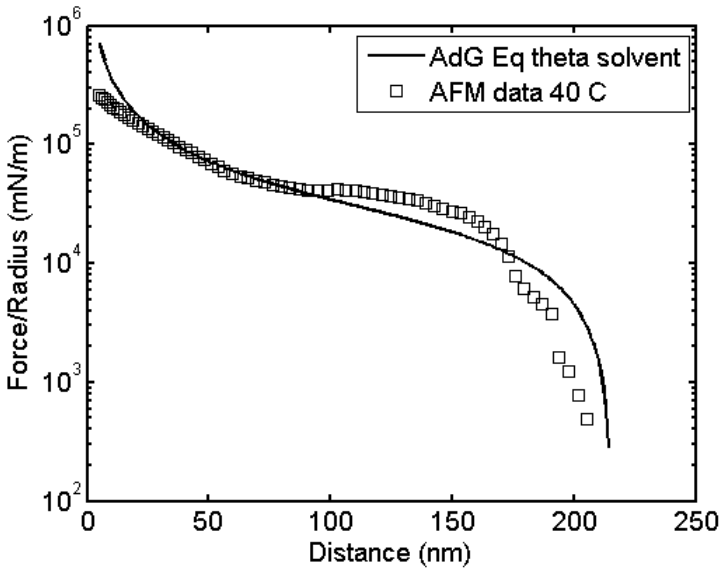


Figure 6.17: PNIPAAm force-distance curve at 40 °C shown with the Alexander-de Gennes model with theta solvent condition.

It was first thought that the surface free energy could be obtained by using the van't Hoff equation,

$$lnK = -\frac{\Delta H}{R}\left(\frac{1}{T_1} - \frac{1}{T_2}\right) + C \tag{6.13}$$

where *ln K* is the equilibrium constant, ΔH is the change in enthalpy of the PNIPAAm layer, R is the gas constant, C is an arbitrary constant of integration. It was believed that the data from the AFM could be modified to such a form and used in the van't Hoff equation. The data from the 'hard press' was integrated with respect to distance, to yield the potential of mean force (PMF). The potential of mean force is the intermolecular potential in a liquid medium. The PMF was then used as the surface free energy, ΔG, between zero distance and distance where the

force was equal to 5 micro Newtons. Surface free energy was then plotted against the inverse of temperature to yield a plot similar to that of van't Hoff. The plot, not shown, had very high error in all the data points. If the PNIPAAm LCST is a true phase transition, then the change in Gibbs energy should be zero in value for the transition. Grinberg et al. confirmed this with microcalrimetry experiments on bulk PNIPAAm [143].

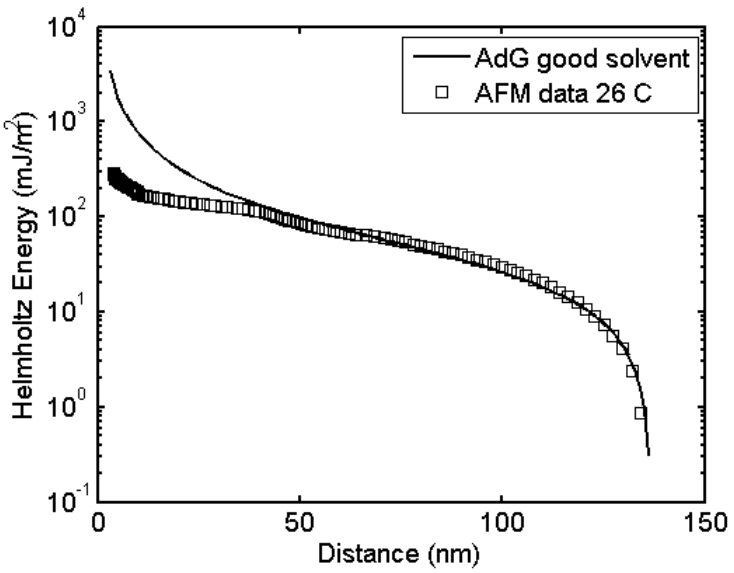


Figure 6.18: Alexander-de Gennes model for Helmholtz free energy with good solvent condition with integrated force-distance data at 26 °C

The surface free energy can be found using Equation 6.11. The various solvent conditions for Equation 6.11 are expanded in the Appendix. The force-distance data was integrated and plotted with the good solvent condition for the Alexander-de Gennes model for Helmholtz free energy and shown in Figure 6.18. The Helmholtz free energy was divided by ρ_a to put the Helmholtz free energy on a per unit basis. Because the Alexander-de Gennes model has several fit parameters, K_a, ρ_a, and L it was assumed that the surface grafting density would be that of a dense grafted polymer brush, 0.15 chains per nm^2 [139]. The two remaining variables, L_o and K_a

can then be used to match the the experimental data, their values are 9000 and 250 nm, respectively. The L_o value is very similar to the value obtain in the 'soft press' section of this chapter. The change in Helmholtz free energy is given in terms of the tip-sample distance. The reference free energy is zero in value at infinite tip-sample separation. The experimental data and model have a close fit at larger distances. The model and data tend to deviate from a smaller distance. As described previously, the deviation is believed to come from polymer brush displacement by the AFM cantilever rather than ideal compression. It would be ideal to compare the surface free energy values obtained with the Alexander-de Gennes model, with those obtained by other methods. Unfortunately, this is not possible since the surface free energy is for PNIPAAm brush-brush interactions and is not a bulk thermodynamic value. It was already shown, in the 'soft press' section, that the force-distance curves for AFM were similar to those produced by SFA. The same procedure could be applied to the SFA data to yield very similar results for surface free energy.

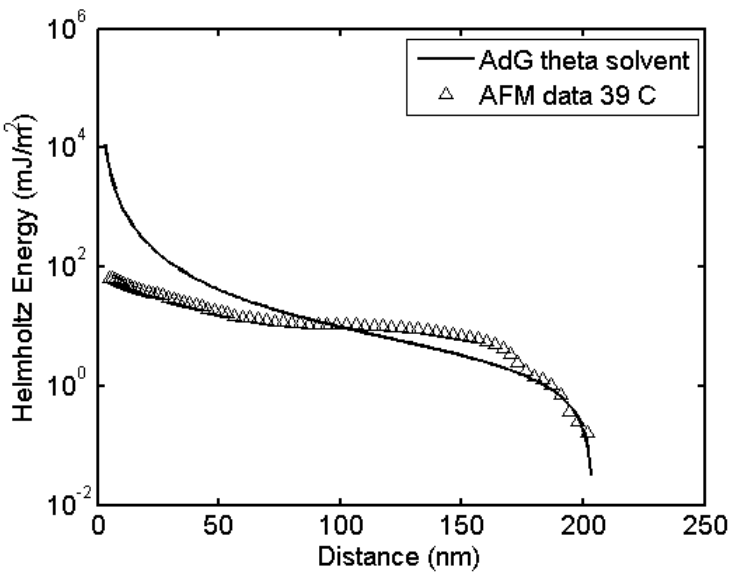


Figure 6.19: Alexander-de Gennes model for Helmholtz free energy with theta solvent condition with integrated force-distance data at 39 °C

The same procedure was done with the force-distance data at 39 °C with the theta solvent condition of the Alexander-de Gennes model resulting in Figure 6.19. The fit of the Alexander-de Gennes model of free energy with the theta solvent condition does not account for all sections of the experimental data. While there is agreement for distances in the mid-range of the data the small and large distances do not closely match the model. At small distances it is believed that the cantilever is displacing the polymer brushes rather than compressing them ideally, leading to the difference between data and model. At large tip-sample distances it is possible the polymer brushes are exhibiting a mixed kind of behavior in solvent condition. Again, the reason for the behavior at large tip-sample distances is not fully known.

The Helmholtz free energy is a generating function for the other thermodynamic values. The differential relationship between Helmholtz free energy and temperature can affect the internal energy of polymer brushes. The large deviations between model and data would question the validity of any thermodynamic values obtained. For temperatures above the LCST, the Alexander-de Gennes model only models part of the polymer brush behavior. The resulting thermodynamics values obtained would only reflect part of the polymer brush behavior and not the system as a whole. To the author's knowledge this is the first attempt at using steric-force data to examine the thermodynamics properties of the surface grown thermally responsive polymer PNIPAAm.

6.4 Conclusion

Bioadhesion to the stimuli responsive polymer brush PNIPAAm will include many chemical and physical factors. It was shown how to examine the Young's modulus of the PNIPAAm surface via force-distance data collected with AFM. The thermal response of the PNIPAAm surface was confirmed by examining the Young modulus

as a function of temperature. This is the first instance of examining the Young's modulus of ATRP grown PNIPAAm with AFM. The various models for examining the surface energy of the PNIPAAm surface were discussed. Only the models by Alexander-de Gennes and DFT were compared to the data. The two models presented a close fit to the experimental data with some deviation at small and large distances. The solvent condition of the polymer brushes was examined by fitting the force-distance data to good and theta solvent case of the Alexander-de Gennes model. The Alexander-de Gennes free energy model was used to examine the thermodynamics of the surface free energy. Utilization of the resulting free energy to generate thermodynamics values were not examined, because of the large deviations between model and force-distance data above the LCST.

Chapter 7

Creation and Utilization of Lipid Bilayer Coated Mesoporous Silica Particles

7.1 Introduction

Lipid vesicles, also called liposomes, are polymolecular aggregates of lipids that form in an aqueous solution from dispersion of bilayer forming molecules. Lipid vesicles also form from surfactants. Figure 7.1 shows an egg phosphatidylcholine (egg PC) molecule, a type of lipid. Under osmotically balanced conditions, lipid vesicles typically generate hollow spherical structures in which the hydrophobic head group of the molecule faces both the inner volume and outer volume aqueous solution. These structures are found throughout nature in eukaryotic cells and bacteria as lipid bilayers. Eukaryotes and bacteria use lipid bilayers for transporting food, cell products, and waste within their cells.

Lipid vesicles have many applications and are used for the following purposes:

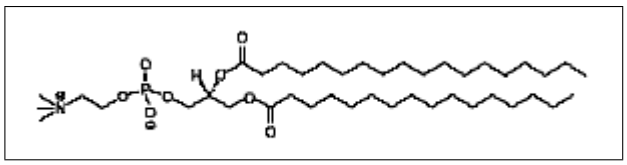


Figure 7.1: Chemical structure of egg phosphatidylcholine

to model cellular membranes [144, 145]; to encapsulate bioactive molecules for drug delivery [146]; and to study the lipid bilayer and vesicle disruption [147]. In addition, lipid vesicles are used to create lipid bilayers that are used in biosensors [148]; as biomimetic objects in biotechnology [148]; as artificial cells [149]; and for diffusion studies within lipid bilayers [150, 148].

The size of lipid vesicles can range from 20 nanometers to hundreds of microns [12]. The constuction of lipid vesicles come in a variety of different forms, including: multilamellar vesicles (MLV), large unilamellar vesicles (LUV), small unilamellar vesicles (SUV), and multivesicular vesicles (MVV). The various types of lipid vesicles can be seen in Figure 7.2.

The standard way to create lipid vesicles is by hydration [151, 152, 146, 153, 154]. Hydration of a dried lipid cake readily results in lipid vesicles although the size, type, and dispersity are not well controlled. To create lipid vesicles with better defined properties, other techniques are used in combination with hydration, including: extrusion [152], double emulsion [154], sonication [151, 153], and microfluidic devices [155]. A description of the methods of vesicle formation and properties of the resulting vesicles can be found in literature reviews [156, 12]. Each method for creating lipid vesicles will yield different vesicle types and sizes. Lipid vesicles generated by hydration will yield polydisperse multivesicular vesicles. If a monodisperse population of vesicles is desired, hydration should be followed by any of the above methods that can control vesicle properties.

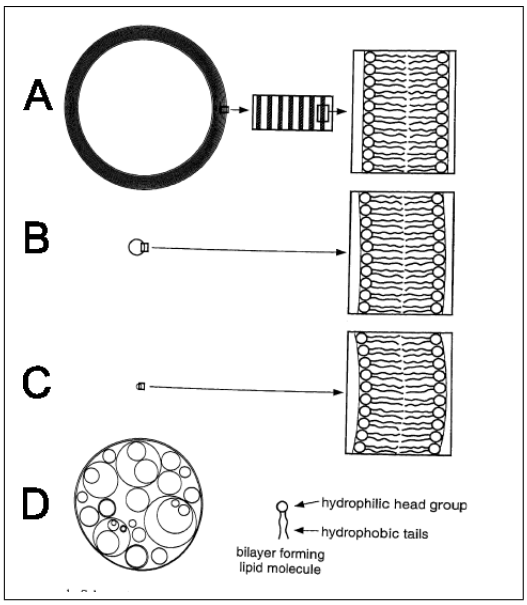


Figure 7.2: Schematic of the various lipid vesicle types, A shows a multilamellar vesicle, B a large unilamellar vesicle, C a small unilamellar vesicle, D a multivesicular vesicle, image taken from Walde and Ichikawa [12].

Lipid vesicles can be used to create lipid bilayers. The stability of the lipid bilayer can be enhanced when the lipid bilayer is coated on a spherical substrate. If the spherical substrate is porous, chemicals can be stored within the pores. Silica particles, a type of spherical substrate, can be made mesoporous by templating their structure with a self-assembling surfactant that forms micelles during particle formation. When this method is applied to a vibrating orifice aerosol generator, the resulting particles are monodisperse in size and have an ordered porous structure within each particle [157]. The mesoporous silica particles are also commercially available as high-performance liquid chromatography packing.

Mass transport has been extensively studied in mesoporous materials [158, 159, 160, 161, 162, 163]. Many of the mass transport studies in mesoporous materials involve flat surfaces [164, 165, 166]. Mass transport studies have also been performed using spherical objects, activated charcoal [167, 168], and heavy-metal remediators

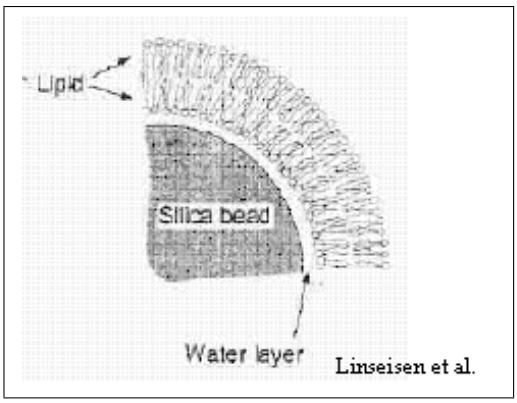


Figure 7.3: Diagram of the lipid bilayer on a particles, taken from Linseisen, et al. [13]

[169]. Linseisen et al. has studied the differences between a lipid bilayer supported on a flat surface and a lipid bilayer supported on a spherical bead [13]. They found that lipid bilayers on a spherical substrate had a higher phase transition temperature than those on a flat substrate, which they interpreted as lipid bilayers on spherical supports are more stable than those on flat surfaces. In the same work, a model of how lipid bilayers coat a spherical silica is presented. In their model, it is predicted that there is a thin water layer between the silica particle and the lipid bilayer as seen in Figure 7.3. In other words, the lipids are not in direct contact with the particle. This is unlike physisorption or chemical attachment.

Previously, our group has studied the mass transport from spherical porous particles modified with a thermally responsive polymer [170]. A similar study was performed by Tziampazis et al. examining the release kinetics of poly-alginate beads loaded with pancreas cells and covered with a lysine membrane [171]. Finally, Anderson et al. examined the release kinetics of insulin from lipid vesicles based on the amount of insulin retention over a 48 hour period [153].

In the research described below, mass transport is characterized from spherical mesoporous particles with and without a coating of a lipid bilayer. To date no one

has studied the mass transport from lipid bilayer coated mesoporous particles. We hypothesized we could control diffusion out of the construct, turning it on or off, by coating the mesoporous partices within a lipid bilayer. To test this hypothesis, mesoporous particles were loaded with a dye and the mass transport quantified by obtaining an effective diffusion coefficient. The particle was then coated with a lipid bilayer after which the mass transport from the particle was observed, this step is called encapsulation. In the last step, the lipid bilayer was disrupted and the mass transport examined.

7.2 Materials and Methods

Materials Egg phosphatidylcholine (Egg PC) was purchased from Avanti Polar Lipids. Sulforhodamine 101 acid chloride (Texas Red), and phosphate buffered saline (PBS) pH 7.0 were purchased from Sigma-Aldrich, St. Louis, MO. Polyoxyethylene Octylphenyl Ether (Triton X-100) is from EMD Chemicals, Gibbstown, NJ. Nucleosil 50-10 porous silica particles came from Machery-Nigel, Duren, Germany. Deionized water was produced in-house from a Nanopure system.

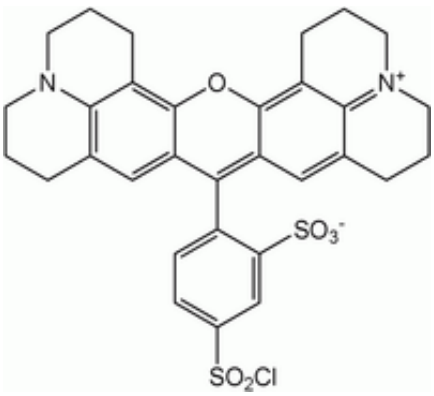


Figure 7.4: Chemical structure of sulforhodamine 101 acid chloride (Texas Red). Diameter of the molecule is approximately 1.8 nm and has no net charge at pH 7.0.

Equipment VWR Galaxy mini centrifuge, orbital shaker, and Shimadzu UV-visible spectrophotometer scanning 800 to 400 nanometers with 1 nanometer step size.

Particle Properties The manufacture of the particles provides the following information about the particles: Mean particle size is 9.74 microns; particle size distribution d_{90}/d_5 (ratio of the cumulative volume percent of 90 to 5) is 1.5; pore volume is 0.85 ml/g; surface area is 383 m^2/g; mean pore diameter is 8.9 nanometers.

Mass transport into the mesoporous particles (uptake) 240 mg of the porous particles were placed in a 4 wt % H_2O_2 and 4 wt % NH_4OH solution in a boiling water bath at 96 °C for 10 minutes. This preparation step would clean and partially hydroxylate the particles [172]. The particles were rinsed 4 times with deionized water. The particles were then separated into aliquots for later use, with a small amount of deionized water to prevent the particles from drying. The porous particles, 24 mg, were then taken and separated equally into three Eppendorf tubes. The particles were centrifuged for 30 seconds (6,000 rpm - 2,000xg) in the mini centrifuge and the water supernatant removed. 4 mL of Texas Red was dissolved in PBS with a concentration of 100 micromolar and then scanned in the UV-visible spectrophotometer. The dye was then added to the particles, a stop watch started, and particles and dye were shaken vigorously and then placed on an orbital shaker. UV-visible cuvettes, pipette tips, and Eppendorf tubes were labeled as 1, 2, and 3. At short time intervals frequent UV-visible measurements were taken of the supernatant. As time progressed, measurement frequency decreased. The Eppendorf tubes were taken from the orbital shaken and placed in the mini centrifuge for 30 seconds. 1 mL of the supernatant was removed and placed in a 1.5 mL cuvette and the spectrum scanned and the supernatant returned to the Eppendorf tube. The tube was vigorously shaken and placed on the orbital shaker. This process was repeated for every UV-visible measurement for 2 hours.

Lipid Bilayer Preparation (encapsulation) The lipids were prepared by rehydration in PBS pH 7.0 to 1 millimolar concentration and placed in an ultrasonic bath for 20 minutes at 0 °C. The surface area of the particles was calculated, the number of lipids required to cover the surface area and then multiply by 10 to give an excess of lipid. The calculated amount of lipid was added to the particles after the uptake experiment with most of the Texas Red solution removed. The particles and lipids were then placed in a VWR vortex genie for 5 minutes and shaken at the highest setting. The particles were let to set for 10 minutes. The porous particles were then rinsed with PBS 10 times. 4 mL of PBS was scanned in the UV-visible spectrophotometer to give a baseline absorbance. The 4 mL was separated equally between the 3 Eppendorf tubes, and the stop watch restarted. The Eppendorf tubes were shaken vigorously and placed on the orbital shaker. UV-visible readings were taken as described above for 2 hours.

Mass transport after lipid bilayer disruption (release) Again 4 mL of PBS was scanned and separated into the Eppendorf tubes. 10 microliters of 100 millimolar Triton X-100 was added to the Eppendorf tubes, the stop watch restarted, then vigorously shaken and placed on the orbital shaker. UV-visible readings were taken as described above for 2 hours. The absorbance of Triton X-100, used to disrupt the lipid bilayer, was subtracted from the absorbance data in the release data. All the absorption data was converted to concentration by the use of calibration curves.

7.3 Results and Discussion

The particles are characterized and a description of the mathematical fit is given. The experimental results are divided into 3 sections. The first when the particles are placed in the dye solution is called 'uptake.' Next when the particles are coated with a lipid bilayer it is called 'encapsulation.' Lastly when the lipid bilayer is disrupted

with Triton X-100 this is called 'release.'

Particle pretreatment

The nucleosil particle can be seen in Figure 7.5. The micrograph confirms the size of the particles and shows the spherical nature of the particle. The image used is typical of the particle population. A larger magnification of the particle surface can be seen in Figure 7.6. The pores can be seen in Figure 7.7. The particle surface is horizontal and the pores are perpendicular to the particle surface.



Figure 7.5: SEM micrograph of the nucleosil particle after base/peroxide wash

Before the experiment the particles are treated with a base/peroxide solution. As reported in the literature this solution changes the properties of the surface layer of the particles [172]. To remove the surfactant within the pores of the particles after creation the particles are calcined. Calcination leaves the silica slightly hydrophobic. The base/peroxide wash hydroxilates the surfaces making it more hydrophilic. Our group previously showed that this surface treatment did not effect the porous network [148]. Confocal micrographs of the particles show that dye is uniformly distributed in the particle, implying the pores transverse the entire particle. It has been observed by SEM micrograph that some particles have a silica skin layer covering the pores.

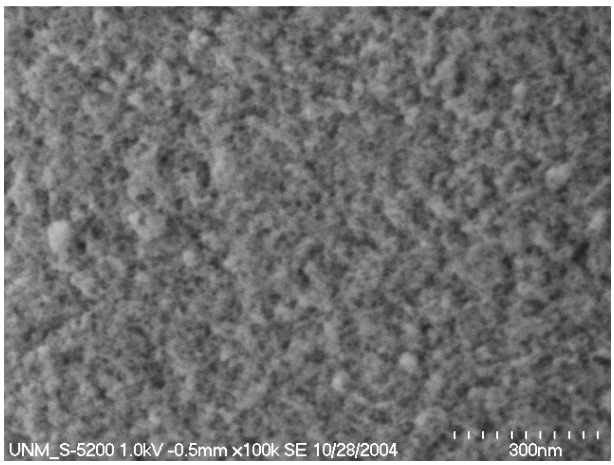


Figure 7.6: SEM micrograph of the nucleosil particle showing surface roughness

The base/peroxide solution dissolves the outer most silica skin layer and exposes the pores. In addition, our research group has discovered that the lipid vesicle forms more readily on hydrophilic particles[148]. This is because the lipid bilayer is stabilized by floating on a trapped water layer around the particle, as observed by Linseisen et al. [13].

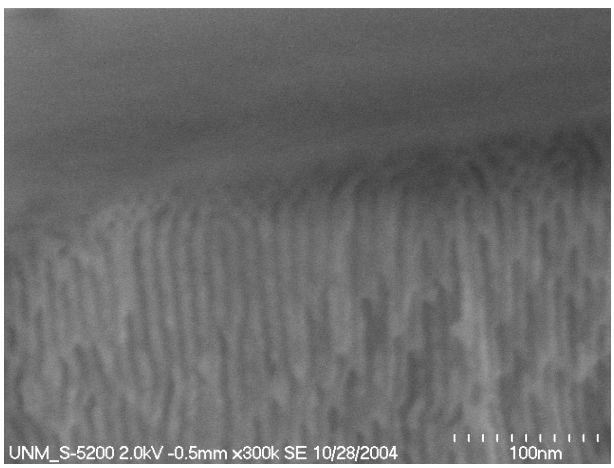


Figure 7.7: SEM micrograph of the nucleosil particle showing the pores perpendicular to the particle surface.

Mathematical fit

In order to quantify the results, a mathematical fit of the diffusion system is needed. Examining the effective diffusion coefficient for the various data sets will help show if the lipid bilayer is encapsulating the diffusing species. The system is setup to be a sphere with a chemical species diffusing into or out of the sphere with constant surface concentration. The governing differential equation,

$$\frac{\partial C}{\partial t} = D_{eff}\left(\frac{\partial^2 C}{\partial r^2} + \frac{2}{r}\frac{\partial C}{\partial r}\right) \tag{7.1}$$

making the substitution

$$U = Cr$$

the equation becomes

$$\frac{\partial U}{\partial t} = D_{eff}\frac{\partial^2 U}{\partial r^2} \tag{7.2}$$

With the boundary conditions,

$$u = 0, \quad r = 0, \quad t > 0, \tag{7.3}$$

$$u = aC_o, \quad r = a, \quad t > 0, \tag{7.4}$$

$$u = rf(r), \quad t = 0, \quad 0 < r < a \tag{7.5}$$

can be solved analytically,

$$\frac{M_t}{M_\infty} = 1 - \frac{6}{\pi}\sum_{i=1}^{\infty}\frac{1}{n^2}\exp\left(\frac{-D_{eff}n^2\pi^2 t}{a^2}\right) \tag{7.6}$$

the solution is taken from *The Mathematics of Diffusion* [173]. C is the concentration of the diffusing species, t is time, D_{eff} is the effective diffusion coefficient, r is the distance in the radial coordinate, C_o is the initial concentration, M_t is the amount of material in the bulk at time t, M_∞ is the amount of material in the bulk at infinite time, n is a counting integer, and a is the radius of the particle. In a known volume the amount of material is the concentration of a species. The solution assumes that the concentration at the surface of the particle does not change with time. We believe this is a reasonable assumption because the initial concentration used was 100 millimolar. This is quite high for a dye species. The finally concentration after uptake changed by 12%. We believe this change is not enough to invalidate a constant surface concentration. The model also assumes a infite volume surounding the particle. We also believe this is a reasonable assumption because the volume of the fluid used in the experiment is an order of magnitude greater than the volume of the sum of the particles. A more accurate mathematical model with variable surface concentration and finite volume could be used, yet the accuracy gained is not necessary due to the noisy nature of the experiments and the dependency of the effective diffusion coefficient on short time data.

When matching the slope of the concentration-time plot data at earlier times are more important than those when the diffusion is at an equilibrium between particle and solution. In this case equilibrium was reached in about 40 minutes, thus the data collected before 40 minutes determinant the effective diffusion coefficient into the particle. The data were fit by a weighted average on the data points of lower time. A factor of ten was added to first two data points when the deviation between fit and data was calculated. This was done to arbitrarily weight the early data points

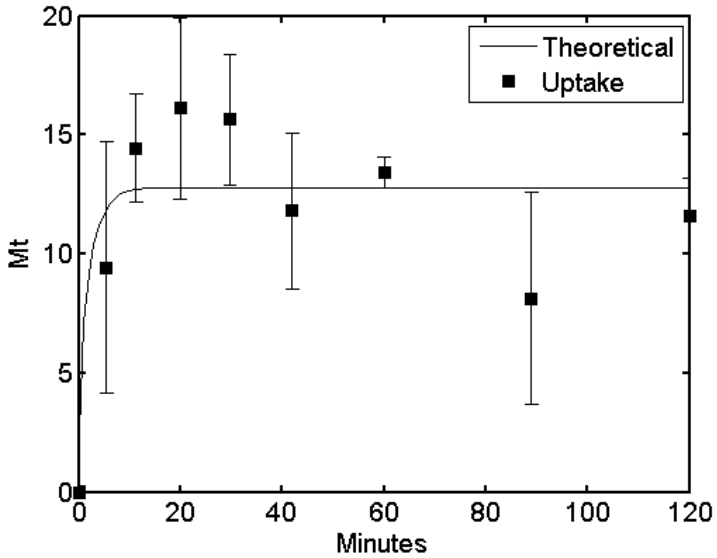


Figure 7.8: Plot of amount of dye in solution with the particle against time during uptake and theoretical solution for diffusion into a sphere. D_{eff} value is = $1*10^{-12}$ m^2/s.

more than the later data points. To obtain the best effective diffusion coefficient the sum of the deviation between the theoretical values and all the data points, including weighting, was minimized.

Uptake

The uptake experiment has dye moving from the bulk solution into the particle. The data recorded by the UV-vis spectrometer show the absorbance of light in the bulk solution. The absorbance data were transformed to concentration using calibration curves, inverted and subtracted from infinite time to match the mathematical model. The uptake of dye into the particles can be seen in Figure 7.8. The error present in the data comes from the deviation of the three sample run concurrently to get the average.

The data shows an increase in the amount of dye species within the particle, which

is consistent with logic. The data also show that most of the diffusion is done within the first twenty minutes of the experiment and then reaches equilibrium with the bulk solution. This fact is in agreement with the knowledge from the mathematical fit that the data points collected early in the experiment are more valuable than later points in quantification of the diffusion into the particles. The best D_{eff} for the uptake data is $1*10^{-12}$ m^2/s. This value is consistant with values from literature for chemical species diffusing in and out of a mesoporous material [166, 171, 160, 170].

There are several sources of error in the experiment, these include: loss of solution during transfer from Eppendorf tube to pipette to cuvette and back again, evaporation of water from each sample, small differences in the absorbance of each cuvette, and small mass differences in the mass of particles between each sample. The largest source of error being the loss of solution during transfer. The experiment could not be run in the cuvettes alone, because the cuvettes could not be centrifuged. Thus, fluid had to be transfered from a container than could be centrifuged to the cuvettes. All these factors contribute to the error present in the data. The error in the first two data points could allow one to argue that the D_{eff} could be in error by an order of magnitude or more. This fact must be remembered when examining the results from the mathematical fit. Another source of error that may or may not be influencing the D_{eff} is particle degredation. SEM micrographs after the uptake experiment showed that some of the particles were breaking. This hypothesis is only partially confirmed because a large population of the particles could not be examined under the SEM.

Encapsulation

In Figure 7.9 the diffusion is occuring in the presence of a single lipid bilayer coating the particle. The data was similarly transformed to concentration and plotted with the mathematical fit. The D_{eff} in Figure 7.9 is $0.4*10^{-12}$ m^2/s.

It was hypothesized the lipid bilayer would completely inhibit the diffusion out of

the particle resulting in a zero D_{eff}. The data in Figure 7.9 shows a diffusion process. The error on the first two data points is smaller in this case making the data more reliable than in the previous uptake experiment. The D_{eff} is an order smaller than the uptake experiment. Thus the lipid bilayer could be thought of as a diffusive barrier. In an ideal situation the lipid bilayer would cover the entire particle without flaw. In this experiment there might be holes present in the lipid bilayer or areas where the lipid bilayer did not cover the entire particle. This could be part of the reason why the lipid bilayer coated particle exhibits diffusion. Confocal micrographs taken by our group of the lipid coated particles appeared intact [148]. It could be and holes in the lipid bilayer are smaller than the resolution of the confocal microscope. Another reason may be the lipid bilayer is a permissive barrier to dye diffusion. A slightly hydrophobic dye molecule would be able loose its hydration molecules and permeate into the hydrophobic region of the lipid bilayer and rehydrate when it leaves the other side. The driving force of this process is the gain in entropy.

Release

Figure 7.10 shows the diffusion of the dye into the bulk after the lipid vesicle has been disrupted. The data was again transformed to concentration and plotted with the mathematical fit. The D_{eff} value was $0.7*10^{-12}$ m^2/s. The M_t value shown in Figure 7.10 has been adjusted by subtracting the absorbance of Triton X-100 with the calculated amount of Egg PC coating the particles in the experiment. Even with this correction the M_t values are larger than prior experiments.

D_{eff} in this experiment is smaller than the D_{eff} found in the uptake experiment. Logic follows that the value should be identical to the D_{eff} value found in the uptake experiment if the lipid bilayer is completely removed from the particles. This very well maybe the case. The error inherent in the experiment should not be forgotten. In this last experiment there is an addition error that may be contributing. The Triton X-100 molecule along with the now disrupted lipid vesicle is now present in

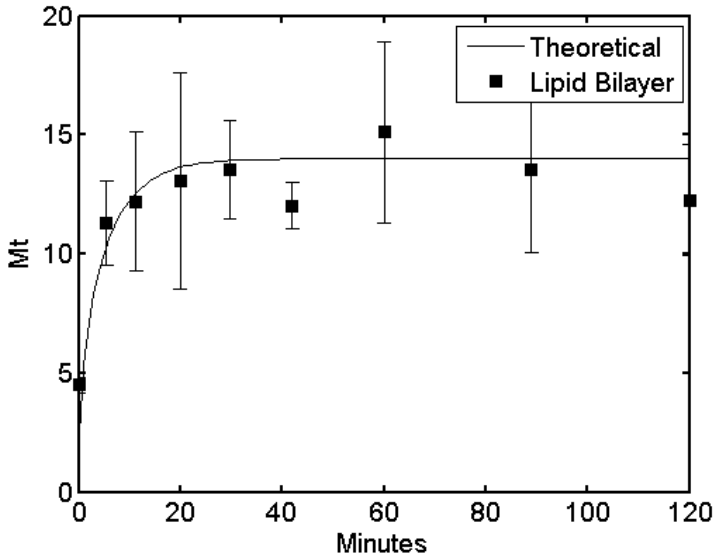


Figure 7.9: Plot of the amount of dye in solution with the particle against time during encapsulation and theoretical solution for diffusion out of a sphere. D_{eff} value is = $0.4*10^{-12}$ m^2/s.

solution. The light scattering and absorbance from both molecules decreased the light intensity detected by UV-visible spectrometer. This is another source of error. An attempt to minimize this error was done by subtracting the absorbance value of the Triton X-100 in solution from the data with dye and Triton X-100. It is still of interest to see that the D_{eff} of the release data is greater than the D_{eff} of the lipid vesicle data. This is in agreement with the hypothesis the that lipid bilayer is inhibiting the diffusion of the dye molecule.

In all the diffusion experiments above, the D_{eff} does not vary greatly between experiments. It is possible that bulk diffusion is not occuring in the pores of the particles. The pore size, which is approching molecular size, maybe the diffusion limiting factor. The dye molecules may be adhering to the pore surface and traveling via creeping diffusion. Thus, the diffusion of the dye molecules would be limited by the adsorption and desorption to the pore surface.

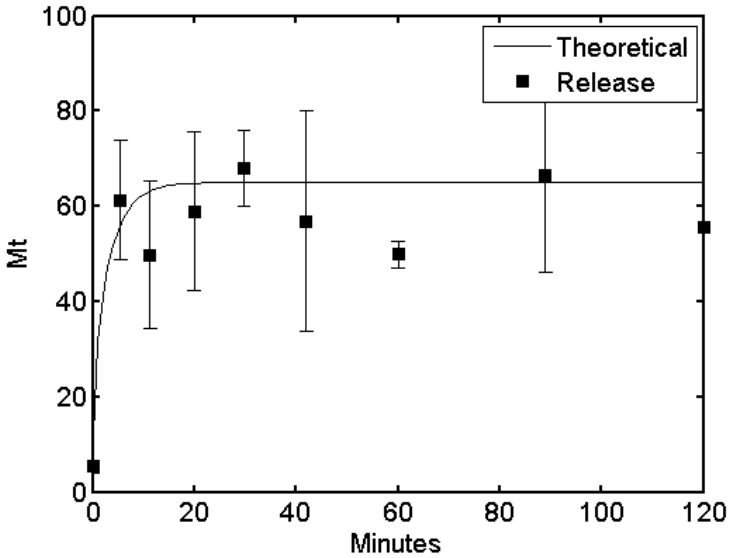


Figure 7.10: Plot of the amount of dye in solution with the particle against time during release and theoretical solution for diffusion out of a sphere. D_{eff} value is = $0.7*10^{-12}$ m^2/s.

The error present in the uptake, encapsulation, and release experiments varied from 5 to 50%. The propogated error in D_{eff} will be slightly greater than that in the experiment. Many attempts were made to try and reduce experimental error, such as using fluorimetery, single experiments with great care to not loose fluid during transfer, and five experiments in parrallel.

An important post examination of the data shows that the material balances from the data shown missing material. The reason is that during the lipid bilayer encapsulation process the particles are rinsed 10 times to remove excess lipid multilayers. During the ten rinse steps it is believed the dye is diffusing out of the particles, and is discarded with the rinse. This is one explanation for the lost material. Another hypothesis is irreversible binding of dye to particles. After the uptake experiment it is observed that the particles are stained pink. Visual observation after the experiment is done shows that the particles are still stained pink. Further observations show

that immersion of the particles for up to a month in pure water does not remove the pink color from the particles.

For future studies, adding species such as cholesterol, which has been shown to enhance lipid bilayer stability, to the lipid bilayer might increase the diffusive barrier to dye species. Other lipid species could be used that have better stability such as dipalmitoylphosphatidylcholine.

7.4 Conclusions

Mass transport from mesoporous particles was studied during an uptake phase, a lipid bilayer coating phase, and after lipid bilayer disruption. The effective diffusion coefficients are of the same order of magnitude as values reported in literature. When the particles were coated with a lipid bilayer they still exhibited diffusion, suggesting that the dye species could still diffuse through the lipid bilayer. The effective diffusion coefficient was lower in value during the encapsulation phase implying a resistive barrier to diffusion. The effective diffusion coefficient increased in value after lipid bilayer disruption. Enhancement of the lipid bilayer is necessary to further test the hypothesis. The techniques presented show promise for controlling release from mesoporous particles.

Chapter 8

Conclusions and Outlook

Bioadhesion is a complex phenomena and additional research is required to further our understanding of how bioadhesion works. It is my hope that this dissertation will be useful to those studying bioadhesion. The experimental methods, data analysis, and models discussed in each chapter are intended to provide the reader with a basic understanding of bioadhesion and stimulus responsive materials. The purpose of this chapter is to recommend additional experiments that may be performed in each field of study discussed in my dissertation.

In chapter 2, I described the characterization of a mixed $C_{11}EG_6OH/C_{11}CH_3$ SAM surface by ellipsometry, contact angle goniometry, XPS, and rat fibroblast growth. However, there is still more research that may be conducted to further characterize this type of thermally responsive surface. For example, the upper and lower limit of surface mole fraction that will yield a thermally responsive surface is not known. This can be studied by changing the surface mole fraction of $C_{11}EG_6OH$ and examining the thermal response by contact angle goniometry. Another study could be performed to confirm the molecular transition of the mixed SAM surface using infrared spectroscopy. A third area that deserves additional study is the effect

of changing the end groups of the diluent thiolate on the thermal responsive behavior of the mixed SAM. Additional research on these topics is important because it will lead to the development of a better controlled and reproducible thermally responsive surface.

In chapter 3, I examined the force of adhesion of several physically adsorbed proteins on a thermally responsive $C_{11}EG_6OH/C_{11}CH_3$ mixed SAM. I found that proteins adhere to a $C_{11}EG_6OH/C_{11}CH_3$ mixed SAM at a temperature above the molecular transition, but do not adhere at room temperature. No one is certain of protein configuration once it is on an Atomic Force Microscopy (AFM) cantilever. To study this initial protein configuration further, characterization could be performed on a protein upon adsorption to an AFM cantilever. From this examination the force of adhesion could be linked to the three dimensional protein configuration, being in a native conformation or in a denatured state. Another study could be conducted to determine which variables are the most influential when using protein labeled AFM microscopy. This could be achieved by designing a matrix of experiments to see which factors affect protein adhesion to a thermally responsive surface. An example would be to place a single protein on the AFM cantilever and then change the pH to see how the charge of the protein affects adhesion.

In chapter 4, I found the surface free energy of two mixed SAMs using the Lewis acid-base (LAB) model. The LAB model describes the electron donation component of surface free energy. To confirm the results obtained from my research, other surface free energy models, including the Wu method, Good-Garifalco method, and Equation of State method, can be used. Another method to confirm my results is to calculate the surface free energy with AFM and adhesion energy between a substrate and a cantilever.

In chapter 5, I used XPS, ellipsometry and contact angle goniometry to study chemical composition, ATRP reaction and thermal responsiveness of a PNIPAAm

surface respectively. While PNIPAAm has been extensively characterized and tested in a laboratory setting, it has not been characterized or tested in commercial and industrial applications. Therefore, the next step in PNIPAAm research should be the development of a well characterized, commercially available, reproducible, and predictable PNIPAAm surface.

In chapter 6, I used AFM force-distance measurements combined with the Alexander-de Gennes model to examine the mechanical and surface free energy properties of PNIPAAm above and below the lower critical solution temperature (LCST). To my knowledge, my research is the first to examine the surface free energy of atom-transfer radical polymerization (ATRP) grown PNIPAAm brushes. To confirm the solvent conditions and surface free energy calculated from my data, other models, including a monte carlo or molecular dynamics model, can be used. Additional research is recommended to examine the effect of polymer cross-linking, brush surface graft density, and polymer brush length on the mechanical and surface free energy by using the same methods described in Chapter 6.

In chapter 7, I studied the mass transport of a dye molecule from a mesoporous particle without, during, and after coating with a lipid bilayer. To verify my results other detection methods, such as NMR tracking and radioactive tracking, should be used to test the values I obtained using UV-visible spectrometry. In addition further research is recommended to enhance lipid vesicle stability, including the use of additive molecules, such as cholesterol, to the lipid bilayer.

Glossary

AFM	atomic force microscopy
ATRP	atom-transfer radical polymerization
CH_3	dodecane thiol
C-10	decane thiol
C-11	undecane thiol
DMEM	Dulbco's modified eagle medium
eV	electron volt
FBS	fetal bovine serum
OEG	oligo(ethylene glycol) thiol
PNIPAAm	poly(*N*-isopropylacrylamide)
ppNIPAAm	plasma polymerized poly(*N*-isopropylacrylamide)
LCST	lower critical solution temperature
MS	mass spectrometry
NMR	nuclear magnetic resonance

Glossary

SAM	self assembled monolayer
SFG	sum frequency generation spectroscopy
XPS	X-ray photoelectron spectroscopy

.1 Additional information

The Appendix contains additional information valuable to the study of bioadhesion to thermally responsive materials, but is additional in nature or too large to include in a chapter.

The Alexander-de Gennes theory for parallel plates in a good solvent,

$$\beta A = LK_a\rho_a^{3/2}\left[4/5\left(\frac{L}{Z_{TS}}\right)^{5/4} - 4/7\left(\frac{Z_{TS}}{L}\right)^{7/4}\right] \tag{.1}$$

$$\beta = \frac{1}{k_B T} \tag{.2}$$

where A is the Helmholtz energy, K_a is a fit parameter, k_B is boltzman's constant, T absolute temperature, ρ_a is the number of chains per surface area or polymer graft density,.

The Alexander-de Gennes theory for parallel plates in a theta solvent,

$$\beta A = LK_b\rho_b^{3/2}\left[2\left(\frac{L}{Z_{TS}}\right)^{2} - \frac{1}{2}\left(\frac{Z_{TS}}{L}\right)^{2}\right] \tag{.3}$$

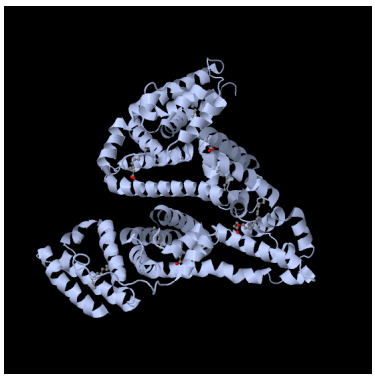
The Alexander-de Gennes theory for parallel plates in a poor solvent,

$$\beta A = LK_c\rho_c^{3/2}\left[0\left(\frac{L}{Z_{TS}}\right)^{\infty} - 0\left(\frac{Z_{TS}}{L}\right)^{\infty}\right] \tag{.4}$$

note that K_a, K_b, K_c and ρ_a, ρ_b, ρ_c are identical in nature although given different notation for different solvent cases.

Table .4 shows the advancing contact angle data from tensiometer, mixed SAM surface composition is 0.6, error std. dev. in contact angle data is $\pm$ 0.05.

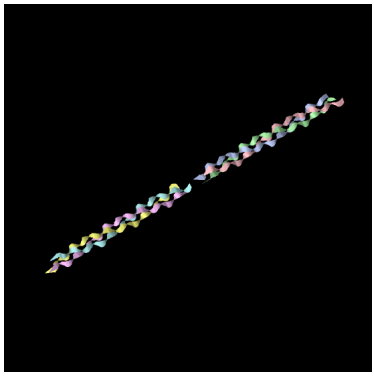
Table .1: Ribbon scructures of the proteins used in mixed $C_{11}EG_6OH/C_{11}CH_3$ SAM experiment.



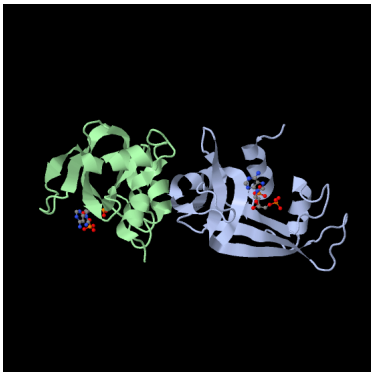
Human serum albumin
Protein ID: 1E7H



Cholera Toxin Subunit B
Protein ID: 1G8Z



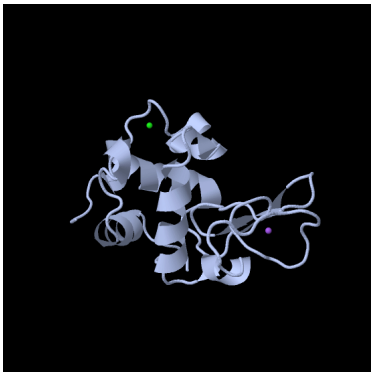
Collagen
Protein ID: 1K6F



Ribonuclease A
Protein ID: 2W5L



Pyruvate Kinase
Protein ID: 1A3W



Lysozyme
Protein ID: 193L

Table .2: List of protein sizes used the adhesion to mixed $C_{11}EG_6OH/C_{11}CH_3$ SAM experiment.

	Lysozyme	Pyruvate kinase	Bovine serum albumin	Collagen	Cholera toxin Subunit B
Height (nm)	3.2	12.0	7.7	1.9	6.0
Width (nm)	5.0	5.8	8.9	2.5	6.5
Length (nm)	2.9	5.7	6.6	18.4	6.5

Table .3: Amino acid composition of the protiens used in the mixed $C_{11}EG_6OH/C_{11}CH_3$ SAM experiments

Amino Acid	Bovine Serium Albumin	Collagen	Pyruvate Kinase	Cholera Toxin Subunit B	Ribonuclease A	Lysozyme
hydrophobic						
A	48	0	43	12	12	14
V	38	0	48	4	9	9
L	65	0	36	6	2	8
I	15	0	37	10	3	5
F	30	0	20	3	3	2
W	3	0	1	1	0	5
M	5	0	11	3	4	2
P	28	120	25	3	4	2
Sum	232	120	221	42	37	47
Hydrophilic						
D	41	0	31	4	5	8
E	58	0	28	8	5	3
G	17	60	34	3	3	11
S	32	0	27	5	15	6
T	34	0	38	10	10	5
C	35	0	7	2	8	8
Y	21	0	15	3	6	6
N	14	0	26	7	10	10
Q	21	0	10	5	7	6
K	60	0	37	9	10	5
R	26	0	24	3	4	13
H	16	0	8	3	4	2
Sum	375	60	285	62	87	83

Table .4: Surface tension values used in the calculation of surface free energy of the mixed $C_{11}EG_6OH/C_{11}CH_3$ SAMs

Substrate	Solvent	Temperature °C	Contact angle (°)
$C_{11}CH_3$	diiodomethane	23	80.29
$C_{11}CH_3$	diiodomethane	40	76.98
$C_{11}CH_3$	water	23	104.17
$C_{11}CH_3$	water	40	103.3
$C_{11}CH_3$	formamide	23	95.25
$C_{11}CH_3$	formamide	40	93.46
$C_{11}EG_6OH$	diiodomethane	23	41.46
$C_{11}EG_6OH$	diiodomethane	40	37.85
$C_{11}EG_6OH$	water	23	33.54
$C_{11}EG_6OH$	water	40	35.15
$C_{11}EG_6OH$	formamide	23	0
$C_{11}EG_6OH$	formamide	40	23.56
Mixed	diiodomethane	23	37.17
Mixed	diiodomethane	40	39.26
Mixed	water	23	36.93
Mixed	water	40	39.22
Mixed	formamide	23	19.24
Mixed	formamide	40	23.65

Table .5: 2nd Root solutions to the Lewis acid base equation

SAM and Temperature (C)	$\gamma_S^{LW}(mJm^{-2})$	$\gamma_S^{+}(mJm^{-2})$	$\gamma_S^{-}(mJm^{-2})$
OEG 22	41	2	34
OEG 40	30	1	33
mixed 22	42	3	34
mixed 40	39	2	37
CH3 22	17	0	0
CH3 40	19	0	0

References

[1] P. Harder, M. Grunze, R. Dahint, G. M. Whitesides, and P. E. Laibinis. Molecular conformation in oligo(ethylene glycol)-terminated self-assembled monolayers on gold and silver surfaces determines their ability to resist protein adsorption. *Journal of Physical Chemistry B*, 102:426–436, 1998.

[2] K. L. Prime and G. M. Whitesides. Adsorption of proteins onto surfaces containing end-attached oligo(ethylene oxide): A model system using self-assembled monolayers. *Journal of the American Chemical Society*, 115:10714–10721, 1993.

[3] S Balamurugan, LK Ista, J Yan, GP Lopez, J Fick, M Himmelhaus, and M Grunze. Reversible protein adsorption and bioadhesion on monolayers terminated with mixtures of oligo(ethylene glycol) and methyl groups. *Journal of the American Chemical Society*, 127:14548–14549, 2005.

[4] Y. Luk, M. Kato, and M. Mrksich. Self-assembled monolayers of alkanethiolates presenting mannitol groups are inert to protein adsorption and cell attachment. *Langmuir*, 16:9604–9608, 2000.

[5] E. C. Cho, Y. D. Kim, and K. Cho. Temperature-dependent intermolecular force measurement of poly(N-isopropylacrylamide) grafted surface with protein. *Journal of Colloid and Interfacial Science*, 286:479–486, 2005.

[6] K. Feldman, G. Hahner, N. D. Spencer, P. Harder, and M. Grunze. Probing resistance to protein adsorption of oligo(ethylene glycol)-terminated self assembled monolayers by scanning force microscopy. *Journal of the American Chemical Society*, 121:10134–10141, 1999.

[7] D. Xiao and M. J. Wirth. Kinetics of surface-initiated atom transfer radical polymerization of acrylamide on silica. *Macromolecules*, 35:2919–2925, 2002.

[8] H. J. Taunton, C. Toprakcioglu, L. J. Fetters, and J. Klein. Interactions between surfaces bearing end-adsorbed chains in a good solvent. *Macromolecules*, 23:571–580, 1990.

[9] S. Mendez, B. P. Andrzejewski, H. E. Canavan, D. J. Keller, J. D. McCoy, G. P. Lopez, and J. G. Curro. Understanding the force-vs-distance profiles of terminally attached poly(N-isopropyl acrylamide) thin films. *Langmuir*, 25:1062410632, 2009.

[10] K. N. Plunkett, X. Zhu, J. S. Moore, and D. E. Leckband. PNIPAM chain collapse depends on the molecular weight and grafting density. *Langmuir*, 22:4259–4266, 2006.

[11] R. M. Overney, D. P. Leta, C. F. Pictroski, M. H. Rafailovich, Y. Liu, J. Quinn, J. Sokolov, A. Eisenberg, and G. Overney. Compliance measurements fo confined polystyrene solutions by atomic force microscopy. *Physical Review Letters*, 76:1272–1275, 1996.

[12] P. Walde and S. Ichikawa. Enzymes inside lipid vesicles: preparation, reactivity and applications. *Biomolecular Engineering*, 18:143–177, 2001.

[13] F. M. Linseisen, M. Hetzer, T. Brumm, and T. M. Bayerl. Differences in the physical properties of lipid monolayers and bilayers on a spherical solid support. *Biophysical Journal*, 72:1659–1667, 1997.

[14] C. J. van Oss. *Interfacial Forces in Aqueous Media, 2nd ed.* Taylor & Francis Group, 2006.

[15] D. M. Yebra, S. Kiil, and K. Dam-Johansen. Antifouling technology - past, present and future steps towards efficient and environmentally friendly antifouling coatings. *Progress in Organic Coatings*, 50:75–104, 2004.

[16] M. E. Callow and J. A. Callow. Marine biofouling: a sticky problem. *Biologist*, 49:1–5, 2002.

[17] C. S. Gudipati, Callow J. A. Callow M. E. Finlay, J. A., and K. L. Wooley. The antifouling and fouling-release perfomance of hyperbranched fluoropolymer (hbfp)-poly(ethylene glycol) (peg) composite coatings evaluated by adsorption of biomacromolecules and the green fouling alga ulva. *Langmuir*, 21:3044–3053, 2005.

[18] L. Li, Zheng J. Chen, S., B. D. Ratner, and S. Jiang. Protein adsorption on oligo(ethylene glycol)-terminated alkanethiolate self-assembled monolayers: The molecular basis for nonfouling behavior. *Journal of Physical Chemistry B*, 109:2934–2941, 2005.

[19] E. M. Hetrick and M. H. Schoenfisch. Reducing implant-related infections: active release strategies. *Chemical Society Reviews*, 35:780789, 2006.

[20] L. K. Ista, H. Fan, O. Baca, and G. P. Lopez. Attachment of bacteria to model solid surfaces: oligo(ethylene glycol) surfaces inhibit bacterial attachment. *FEMS Microbiology Letters*, 142:59–63, 1996.

[21] M. Morra and C. Cassineli. Non-fouling properties of polysaccharide-coated surfaces. *Journal of Biomaterials Science Polymer Edition*, 10:1107–1124, 1999.

[22] G. Voskericiana, M. S. Shivea, R. S. Shawgoc, H. Recumd, J. M. Andersona, M. J. Cimac, and R. Langer. Biocompatibility and biofouling of MEMS drug delivery devices. *Biomaterials*, 24:1959–1967, 2003.

[23] Cyrus Chothia and E. Yvonne Jones. The molecular structure of cell adhesion molecules. *Annual Review Biochemistry*, 66:823–862, 1997.

[24] D. Leckband. Molecular mechanisms of cell adhesion: New perspectives from surface force measurements. *The Journal of Adhesion*, 80:409–432, 2004.

[25] A. G. Mikos, S. W. Herring, P. Ochareon, J. Elisseeff, H. H. Lu, R. Kandel, F. J. Schoen, Me. Toner, D. Mooney, A. Atala, M. E. Van Dyke, D. Kaplan, and G. Vunjak-Novakovic. Engineering comples tissues. *Tissue Engineering*, 12:3307–3339, 2006.

[26] A. Atala, S. B. Bauer, S. Soker, J. J. Yoo, and A. B. Retik. Tissue-engineered autologous bladders for patients needing cystoplasty. *Lancet*, 367:1241–1246, 2006.

[27] Y. Akiyama, A. Kikuchi, M. Yamato, and T. Okano. Ultrathin poly(N-isopropylacrylamide) grafted layer on polystyrene surfaces for cell adhesion/detachment control. *Langmuir*, 20:5506–5511, 2004.

[28] L. E. Freed, F. Guilak, X. E. Guo, M. L. Gray, R. Tranquillo, J. W. Holmes, M. Radisic, M. V. Sefton, D. Kaplan, and G. Vunjak-Novakovic. Advanced tools for tissue engineering: Scaffolds, bioreactors, and signaling. *Tissue Engineering*, 12:3285–3305, 2006.

[29] D. E. Ingber, V. C. Mow, D. Butler, L. Niklason, J. Huard, J. Mao, I. Yannas, D. Kaplan, and G. Vunjak-Novakovic. Tissue engineering and developmental biology: Going biomimetic. *Tissue Engineering*, 12:3265–3283, 2006.

[30] J. M. Harris and S. Zalipsky. *Poly Ethylene Glycol*. American Chemical Society, 1997.

[31] C. Pale-Grosdemange, E. S. Simon, K. L. Prime, and G. M. Whitesides. Formation of self-assembled monolayers by chemisorption of derivatives of oligo(ethylene glycol) of structure HS(CH2)1 OCH2CH2),OH on gold. *Journal of the American Chemical Society*, 113:12–20, 1991.

[32] K. L. Prime and G. M. Whitesides. Self-assembled organic monolayers: Model systems for studying adsorption of proteins at surfaces. *Science*, 252:1164–1167, 1991.

[33] S. Herrwerth, W. Eck, S. Reinhardt, and M. Grunze. Factors that determine the protein resistance of oligoether self-assembled monolayers - internal hydrophilicity, terminal hydrophilicity, and lateral packing density. *Journal of the American Chemical Society*, 125:9359–9366, 2003.

[34] D. Schwendel, R. Dahint, S. Herrwerth, M. Schloerholz, W. Eck, and M. Grunze. Temperature dependence of the protein resistance of poly- and oligo(ethylene glycol)-terminated alkanethiolate monolayers. *Langmuir*, 17:5717–5720, 2001.

[35] A. J. Pertsin and M. Grunze. Computer simulation of water near the surface of oligo(ethylene glycol)-terminated alkanethiol self-assembled monolayers. *Langmuir*, 16:8829–8841, 2000.

[36] R. G. Chapman, E. Ostuni, M. N. Liang, G. Meluleni, E. Kim, L. Yan, G. Pier, H. S. Warren, and G. M. Whitesides. Polymeric thin films that resist the adsorption of proteins and the adhesion of bacteria. *Langmuir*, 17:1225–1233, 2001.

[37] A. J. Pertsin, T. Hayashi, and M. Grunze. The interaction of oligo(ethylene glycol) with water: Testing an atomistic force field for transferability. *Physical Chemistry Chemical Physics*, 3:15981601, 2001.

[38] R. G. Chapman, E. Ostuni, L. Yan, and G. M. Whitesides. Preparation of mixed self-assembled monolayers (SAMs) that resist adsorption of proteins using the reaction of amines with a SAM that presents interchain carboxylic anhydride groups. *Langmuir*, 16:6927–6936, 2000.

[39] E. R. Beach, G. W. Tormoen, and J. Drelich. Pull-off forces measured between hexadecanethiol self-assembled monolayers in air using an atomic force microscope: analysis of surface free energy. *Journal of Adhesion Science and Technology*, 16:845868, 2002.

[40] J. C. Vickerman, R. Wilson, B. Ratner, D. Castner, and H. Joerg. *Surface Analysis: The Principal Techniques*. John Wiley & Sons, 1997.

[41] N. T. Flynn, T. T. Tran, M. J. Cima, and R. Langer. Long-term stability of self-assembled monolayers in biological media. *Langmuir*, 19:10909–10915, 2003.

[42] A. W. Adamson and A. P. Gast. *Physical Chemistry of Surfaces, 6th ed.* Wiley-Interscience, 1997.

[43] J.J. Bikerman. *Physical Surfaces*. Academic Press, 1970.

[44] Prochimia Homepage. http://www.prochimia.com (accessed Jul 30, 2005).

[45] F. E. Bailey and J. V. Koleske. *Poly ethylene oxide*. Academic Press, 1976.

[46] R. Valiokas, M. Ostblom, S. Svedhem, S. C. T. Svensson, and B. Liedberg. Thermal stability of self-assembled monolayers: Influence of lateral hydrogen bonding. *Journal of Physical Chemistry B*, 106:10401–10409, 2002.

[47] S. J. Stranick, A. N. Parikh, D. L. Allara, and P. S. Weiss. A new mechanism for surface diffusion: Motion of a substrate-adsorbate complex. *Journal of Physical Chemistry*, 98:11136–11142, 1994.

[48] S. J. Stranick, S. V. Atre, A. N. Parikh, M. C. Wood, D. L. Allara, N. Winograd, and P. S. Weiss. Nanometer-scale phase separation in mixed composition self-assembled monolayers. *Nanotechnology*, 7:438–442, 1996.

[49] M. Malmsten. *Protein Adsorption at the Solid-Liquid Interface*, chapter 1, pages 1–24. Marcel and Dekker, 2000.

[50] F. Fang and I. Szleifer. Effect of molecular structure on the adsorption of protein on surfaces with grafted polymers. *Langmuir*, 18:5497–5510, 2002.

[51] M. Malmsten. Formation of adsorbed protein layers. *Journal of Colloid and Interface Science*, 207:186–199, 1998.

[52] K. Ohkawa, A. Nishida, R. Honma, Y. Matsui, K. Nagaya, A. Yuasa, and H. Yamamoto. Studies on fouling by the freshwater mussel Limnoperna fortunei and the antifouling effects of low energy surfaces. *Biofouling*, 13:337–350, 1999.

[53] A. Sethuraman, M. Han, R. S. Kane, and G. Belfort. Effect of surface wettability on the adhesion of proteins. *Langmuir*, 20:7779–7788, 2004.

[54] S. Kidoaki and T. Matsuda. Adhesion forces of the blood plasma proteins on self-assembled monolayer surfaces of alkanethiolates with different functional groups measured by an atomic force microscope. *Langmuir*, 15:7639–7646, 1999.

[55] L. Xu, V. Vadillo-Rodriguez, and B. E. Logan. Residence time, loading force, pH, and ionic strength affect adhesion forces between colloids and biopolymer-coated surfaces. *Langmuir*, 21:7491–7500, 2005.

[56] G. V. Lubarsky, M. M. Browne, S. A. Mitchel, M. R. Davidson, and R. H. Bradley. The influence on electrostatic forces on protein adsorption. *Colloids and Interfaces, B, Biointerfaces*, 44:56–63, 2005.

[57] J. Israelachvili. *Intermolecular and Surface Forces*. Academic Press, 1992.

[58] Van Gool R.G.J. Reutelingsperger, C.P.M., V. Heijnen, P. Frederik, and T. Lindhout. The rotating disc as a device to study the adhesive properties of endothelial cells under differential shear stresses. *Journal of Materials Science: Materials in Medicine*, 5:361–367, 1994.

[59] J. D. Cox, M. S. Skirboll, S. K. Gourley, and D. Y. Sasaki. Surface passivation of a microfluidic device to glial cell adhesion: a comparison of hydrophobic and hydrophilic sam coatings. *Biomaterials*, 23:929–935, 2002.

[60] H. Ma, J. Hyun, P. Stiller, and A. Chilkoti. Non-fouling oligo(ethylene glycol)-functionalized polymer brushes synthesis by surface-initiated atom transfer radical polymerization. *Advanced Materials*, 16:338–341, 2004.

[61] K. A. Willets and R. P. Duyne. Localized surface plasmon resonance spectroscopy and sensing. *Annual Review of Physical Chemistry*, 58:27–297, 2007.

[62] P. Roach, D. Farrar, and C. C. Perry. Interpretation of protein adsorption: Surface-induced conformational changes. *Journal of the American Chemical Society*, 22:8168–8173, 2005.

[63] Q. Lin, D. Gourdon, C. Sun, N. Holten-Andersen, T. H. Anderson, J. H. Waite, and J. N. Israelachvili. Adhesion mechanisms of the mussel foot proteins mfp-1 and mfp-3. *Proceedings of the National Academy of Sciences of the United States of America*, 104:3782–3786, 2007.

[64] A. Noy. *Handbook of Molecular Force Spectroscopy*. Springer, 2008.

[65] A. Noy, C. D. Frisbie, F. Rozsnyai, L., M. S. Wrighton, and C. M. Lieber. Chemical force microscopy: Exploiting chemically-modified tips to quantify adhesion, friction, and functional group distributions in molecular assemblies. *Journal of the American Chemical Society*, 117:7943–7951, 1995.

[66] A. Noy, D. V. Vezenov, and C. M. Lieber. Chemical force microscopy. *Annual Review of Materials Science*, 27:381–421, 1997.

[67] M. S. Wang, L. B. Palmer, J. D. Schwartz, and A. Razatos. Evaluating protein attraction and adhesion to biomaterials with the atomic force microscope. *Langmuir*, 20:7753–7759, 2004.

[68] S. Kidoaki, S. Ohya, Y. Nakayama, and T. Matsuda. Thermoresponsive structural change of a poly(N-isopropylacrylamide) graft layer measured with an atomic force microscope. *Langmuir*, 17:2402–2407, 2001.

[69] L. Xu and C. A. Siedlecki. Effects of surface wettability and contact time on protein adhesion to biomaterial surfaces. *Biomaterials*, 28:3273–3283, 2007.

[70] K. L. Johnson, K. Kendall, and A. D. Roberts. Surface energy and the contact of elastic solids. *Proceedings of the Royal Society of London. Series A, Mathematical and Physical Sciences*, 324:301–313, 1971.

[71] J. R. Davis. *Metals Handbook Desk Edition, 2nd edition.* ASM International, 1998.

[72] G. E. Poirier, E. D. Pylant, and J. M. White. Crystalline structures of pristine and hydrated mercaptohexanol self-assembled monolayers on au(111). *Journal of Chemical Physics*, 104:7325–7328, 1996.

[73] C. Roberts, C. S. Chen, M. Mrksich, V. Martichonok, D. E. Ingber, and G. M. Whitesides. Using mixed self-assembled monolayers presenting RGD and (EG)3OH groups to characterize long-term attachment of bovine capillary endothelial cells to surfaces. *Journal of the American Chemical Society*, 120:6548–6555, 1998.

[74] S Kidoaki and T Matsuda. Mechanistic aspects of protein/material interactions probed by atomic force microscopy. *Colloids and Surfaces B*, 23:153–163, 2002.

[75] J. A. Callow, M. E. Callow, L. K. Ista, G. Lopez, and M. K. Chaudhury. The influence of surface energy on the wetting behaviour of the spore adhesive of the marine alga Ulva linza (synonym Enteromorpha linza). *Journal of the Royal Society Interface*, 2:319–325, 2005.

[76] L. K. Ista, M. E. Callow, J. A. Finlay, S. E. Coleman, A. C. Nolasco, R. H Simons, J. A. Callow, and G. P. Lopez. Effect of substratum surface chemistry and surface energy on attachment of marine bacteria and algal spores. *Applied and Environmental Microbiology*, 70:41514157, 2004.

[77] M. N. Bellon-Fontaine, J. Rault, and C. J. van Oss. Microbial adhesion to solvents: a novel method to determine the electron-donor/electron-acceptor or Lewis acid-base properties of microbial cells. *Colloids and Surfaces B: Biointerfaces*, 7:47–53, 1996.

[78] I. Pezron, A. Rochex, J. Lebeault, and D. Clausse. Determination of cellulose surface energy by imbibition experiments in relation to bacterial adhesion. *Journal of Dispersion Science and Technology*, 25:781787, 2004.

[79] P.K. Sharma and K. Hanumantha Rao. Analysis of different approaches for evaluation of surface energy of microbial cells by contact angle goniometry. *Journal of Colloid and Interfacial Science*, 98:341–463, 2002.

[80] Y. Liu, J. Strauss, and T. A. Camesano. Thermodynamic investigation of staphylococcus epidermidis interactions with protein-coated substrata. *Langmuir*, 23:7134–7142, 2007.

[81] W. A. Zisman. Influence on the constitution of adhesion. *Industrial Engineering and Chemistry*, 55:18–38, 1963.

[82] L. A Good and R. J. Garifalco. A theory for the estimation of the surface and interfacial energies. *Journal of Physical Chemistry*, 61:904–909, 1957.

[83] F. M. Fowkes. Attractive forces at interfaces. *Industrial and Engineering Chemistry*, 56:40–52, 1964.

[84] D. K. Owens and R. C. Wendt. Estimation of the free surface energy of polymers. *Journal of Applied Polymer Science*, 13:1714, 1969.

[85] S. Wu. Polar and nonpolar interactions in adhesion. *The Journal of Adhesion*, 5:39–55, 1973.

[86] C. J. van Oss, R. J. Good, and M. K. Chaudhurys. Additive and nonadditive surface tension components and the interpretation of contact angles. *Langmuir*, 4:884–891, 1988.

[87] L. Lee. Correlation between lewis acid-base surface interaction components and linear solvation energy relationship solvatochromic a and b parameters. *Langmuir*, 12:1681–1687, 1996.

[88] J. Tien, A. Terfort, and G.M. Whitesides. Microfabrication through electrostatic self-assembly. *Langmuir*, 13:5349–5355, 1997.

[89] C. D. Bain, E. B. Troughton, Y. T. Tao, J. Evall, G. M. Whitesides, and R. G. Nuzzo. Formation of monolayer filmes by the spontaneous assembly of organic thiols from solution onto gold. *Journal of the Amercian Chemical Society*, 111:321–335, 1989.

[90] S. C. Clear and P. F. Nealey. Chemical force microscopy study of adhesion and friction between surfaces functionalized with self-assembled monolayers and immersed in solvents. *Journal of Colloid and Interface Science*, 213:238–250, 1999.

[91] C. Boutris, E. G. Chatzi, and C. Kiparissides. Characterization of the lcst behaviour of aqueous poly(n-isopropylacrylamide) solutions by thermal and cloud point techniques. *Polymer*, 38:2567–2570, 1997.

[92] M. Shibayama, M. Morimoto, and S. Nomura. Phase separation induced mechanical transition of poly(n-isopropylacrylamide)/water isochore gels. *Macromolecules*, 27:5060–5066, 1994.

[93] Y. Suzuki, K. Nozaki, T. Yamamoto, K. ltoh, and I. Nishio. Quasielastic light scattering study of the formation of inhomogeneities in gels. *Journal of Chemical Physics*, 95:3808–3812, 1992.

[94] K. C. Tam, X. Y. Wu, and R. H. Pelton. Viscometry - a useful tool for studying conformational changes of poly(n-isopropylacylamide) in solutions. *Polymer*, 33:436–438, 1992.

[95] Y. Maeda, T. Higuchi, and I. Ikeda. FTIR spectroscopic and calorimetric studies of the phase transitions of N-isopropylacrylamide copolymers in water. *Langmuir*, 17:7535–7539, 2001.

[96] X. Wang, X. Qiu, and C. Wu. Comparison of the coil-to-globule and the globule-to-coil transitions of a single poly(n-isopropylacrylamide) homopolymer chain in water. *Macromolecules*, 31:2972–2976, 1998.

[97] Y. Maeda, T. Higuchi, and I. Ikeda. Change in hydration state during the coil-globule transition of aqueous solutions of poly(n-isopropylacrylamide) as evidenced by ftir spectroscopy. *Langmuir*, 16:7503–7509, 2000.

[98] T. Miyame, H. Akiyama, M. Yoshida, and N. Tamaoki. Characterization of poly(n-isopropylacrylamide)-grafted interfaces with sum-frequency generation spectroscopy. *Macromolecules*, 4601-4606:40, 2007.

[99] J. Chern, W. Lee, and M. Hsieh. Preparation and swelling characterization of poly(n-isopropylacrylamide)-based porous hydrogels. *Journal of Applied Polymer Science*, 92:3651–3658, 2004.

[100] Y. Katsumoto, T. Tanaka, H. Sato, and Y. Ozaki. Conformational change of poly(n-isopropylacrylamide) during the coil-globule transition investigated by attenuated total reflection/infrared spectroscopy and density functional theory calculation. *Journal of Physical Chemistry A*, 106:3429–3435, 2002.

[101] D. L. Huber, R. P. Manginell, and Kim B. Samara, M. A., and B. C. Bunker. Programmed adsorption and release of proteins in a microfluidic device. *Science*, 301:352–354, 2003.

[102] Y. V. Pan, R. A. Wesley, R. Luginbuhl, D. D. Denton, and B. D. Ratner. Plasma polymerized N-isopropylacrylamide: Synthesis and characterization of a smart thermally responsive coating. *Biomacromolecules*, 2:32–36, 2001.

[103] X. Zhu, C. Yan, F. M. Winnik, and D. Leckband. End-grafted low-molecular-weight PNIPAM does not collapse above the LCST. *Langmuir*, 23:162–169, 2007.

[104] N. Idota, A. Kikuchi, J. Kobayashi, Y. Akiyama, K. Sakai, and T. Okano. Thermal modulated interaction of aqueous steroids using polymer-grafted capillaries. *Langmuir*, 22:425–430, 2006.

[105] H. Yim, M. S. Kent, S. Mendez, S. S. Balamurugan, S. Balamurugan, G. P. Lopez, and S. Satija. Temperature-dependent conformational change of PNIPAM grafted chains at high surface density in water. *Macromolecules*, 37:1994–1997, 2004.

[106] H. Yim, M. S. Kent, S. Satija, S. Mendez, S. S. Balamurugan, S. Balamurugan, and G. P. Lopez. Study of the conformational change of poly(N-isopropylacrylaminde)-grafted chains in water with neutron reflection: Molecular weight dependence at high grafting density. *Journal of Polymer Science B*, 42:3302–3310, 2004.

[107] N. Yamada, T. Okano, H. Sakai, Sawasaki Y. Karikusa, F., and Y. Sakurai. Thermo-responsive polymeric surfaces; control of attachment and detachment of cultured cells. *Die Makromolekulare Chemie. Rapid Communications*, 11:571–576, 1990.

[108] T. Shimizu, M. Yamato, Y. Isoi, T. Akutsu, T. Setomaru, K. Abe, A. Kikuchi, M. Umezu, and T. Okano. Fabrication of pulsatile cardiac tissue grafts using a novel 3-dimensional cell sheet manipulation technique and temperature-responsive cell culture surfaces. *Circulation Research*, 90:e40–e48, 2002.

[109] Y. Tsuda, A. Kikuchi, M. Yamato, Y. Sakurai, M. Umezu, and T. Okano. Control of cell adhesion and detachment using temperature and thermoresponsive copolymer grafted culture surfaces. *Journal of Biomedical Materials Research part A*, 69A:70–78, 2004.

[110] H. E. Canavan, X. Cheng, D. J. Graham, B. D. Ratner, and D. G. Castner. Surface characterization of the extracellular matrix remaining after cell detachment from a thermoresponsive polymer. *Langmuir*, 21:1949–1955, 2005.

[111] L. K. Ista, V. H. Perez-Luna, and G. P. Lopez. Surface-grafted, environmentally sensitive polymers for biofilm release. *Applied and Environmental Microbiology*, 65:1603–1609, 1999.

[112] D. Cunliffe, C. de las Heras Alarcon, V. Peters, J. R. Smith, and C. Alexander. Thermoresponsive surface-grafted poly(n-isopropylacrylamide) copolymers: Effect of phase transitions on protein and bacterial attachment. *Langmuir*, 19:2888–2899, 2003.

[113] L. Liang, X. Feng, L. Peurrung, and V. Viswanathan. Temperature-sensitive membranes prepared by uv photopolymerization of n-isopropylacrylamide on a surface of porous hydrophilic polypropylene membranes. *Journal of Membrane Science*, 162:235–246, 1999.

[114] X. Cheng, H. E. Canavan, M. J. Stein, J. R Hull, S. J. Kweskin, M. S. Wagner, G. A. Somorjai, D. G. Castner, and B. D. Ratner. Surface chemical and mechanical properties of plasma-polymerized N-isopropylacrylamide. *Langmuir*, 21:7833–7841, 2005.

[115] L. K. Ista, S. Mendez, V. H. Perez-Luna, and G. P. Lopez. Synthesis of poly(n-isopropylacrylamide) on initiator-modified self-assembled monolayers. *Langmuir*, 17:2552–2555, 2001.

[116] B. Ray, Y. Isobe, K. Matsumoto, S. Habaue, Y. Okamoto, M. Kamigaito, and M. Sawamoto. Raft polymerization of n-isopropylacrylamide in the absence and presence of Y(OTf)3: Simultaneous control of molecular weight and tacticity. *Macromolecules*, 37:1702–1710, 2004.

[117] T. E. Patten and K. Matyjaszewski. Atom transfer radical polymerization and the synthesis of polymeric materials. *Advanced Materials*, 10:901–915, 1998.

[118] M. J. Mulvihill, B. L. Rupert, R. He, A. Hochbaum, J. Arnold, and P. Yang. Synthesis of bifunctional polymer nanotubes from silicon nanowire templates via atom transfer radical polymerization. *Journal of the American Chemical Society Communications*, 127:16040–16041, 2005.

[119] D. M. Jones, A. A. Brown, and W. T. S. Huck. Surface-initiated polymerizations in aqueous media: Effect of initiator density. *Langmuir*, 18:1265–1269, 2002.

[120] J. Wang and K. Matyjaszewski. Controlled "living" radical polymerization. atom transfer radical polymerization in the presence of transition-metal complexes. *Journal of the American Chemical Society*, 117:5614–5615, 1995.

[121] K. Matyjaszewski, H. Dong, W. Jakubowski, J. Pietrasik, and A. Kusumo. Grafting from surfaces for "everyone": ARGET ATRP in the presence of air. *Langmuir*, 23:4528–4531, 2007.

[122] M. Kaholek, W. Lee, S. Ahn, H. Ma, K. C. Caster, B. LaMattina, and S. Zauscher. Stimulus-responsive poly(N-isopropylacrylamide) brushes and nanopatterns prepared by surface-initiated polymerization. *Chemistry of Materials*, 16:3688–3696, 2004.

[123] H. Tu, C. E. Heitzman, and P. V. Braun. Patterned poly(n-isopropylacrylamide) brushes on silica surfaces by microcontact printing followed by surface-initiated polymerization. *Langmuir*, 20:8313–8320, 2004.

[124] T. R. Matzelle, D. A. Ivanov, D. Landwehr, L. A. Heinrich, Ch. Herkt-Bruns, R. Reichelt, and N. Kruse. Micromechanical properties of smart gels: Studies by scanning force and scanning electron microscopy of PNIPAAm. *The Journal of Physical Chemistry B*, 106:2861–2866, 2002.

[125] T. R. Matzelle, G. Geuskens, and N. Kruse. Elastic properties of poly(N-isopropylacrylamide) and poly(acrylamide) hydrogels studied by scanning force microscopy. *Macromolecules*, 36:2926–2931, 2003.

[126] D. Alamarguy, O. Schneegans, S. Noel, and L. Boyer. Correlation between the electrical and mechanical behaviours of a nanocontact with an alkane thiol monolayer. *Applied Surface Science*, 225:309–317, 2004.

[127] D. V. Derjaguin, V. M. Muller, and Y. P. Toporov. Effect of contact deformations on the adhesion of particles. *Journal of Colloid and Interface Science*, 53:314–326, 1975.

[128] D. Maugis. On the contact and adhesion of rough surfaces. *Journal of Colloid and Interface Science*, 150:243–269, 1991.

[129] M. Kaholek, W. Lee, B. LaMattina, K. C. Caster, and S. Zauscher. *Polymerization, Nanopatterning and Characterization of Surface-Confined, Stimulus-Responsive Polymer Brushes*, chapter 19, pages 381–402. Wiley-VCH, 2004.

[130] S. T. Milner, T. A. Witten, and M. E. Cates. Theory of the grafted polymer brush. *Macromolecules*, 21:2610–2619, 1988.

[131] S. C. McLean, H. Lioe, L. Meagher, V. S. J. Craig, and M. L. L. Gee. Atomic force microscopy study of the interaction between adsorbed poly(ethylene oxide) layers: Effects of surface modification and approach velocity. *Langmuir*, 21:2199–2208, 2005.

[132] H. Butt, M. Kappl, H. Mueller, and R. Raiteri. Steric forces measured with the atomic force microscope at various temperatures. *Langmuir*, 15:2559–2565, 1999.

[133] S. Cuenot, S. Gabriel, R. Jerome, C. Jerome, C. Fustin, A. Jonas, and A. Duwez. First insights into electrografted polymers by AFM-based force spectroscopy. *Macromolecules*, 39:8428–8433, 2006.

[134] S. J. Alexander. Adsorption of chain molecules with a polar head - a scaling description. *Journal de Physique*, 38:983–987, 1977.

[135] P. G. de Gennes. Polymer solutions near an interface. adsorption and depletion layers. *Macromolecules*, 14:1637–1644, 1981.

[136] P. G. de Gennes. Polymers at an interface; a simplified view. *Advances in Colloid and Interface Science*, 27:189–209, 1987.

[137] S. Mendez, J. G. Curro, J. D. McCoy, and G. P. Lopez. Computational modeling of the temperature-induced structural changes of tethered poly(n-isopropylacrylamide) with self-consistent field theory. *Macromolecules*, 38:174–181, 2005.

[138] J. D. McCoy and J. G. Curro. The colloidal force of bead-spring chains in a good solvent. *Journal of Physical Chemistry*, 122:164905–164912, 2005.

[139] P. J. Flory. *Principles of Polymer Chemistry*. Cornell University Press, 1953.

[140] New World Encyclopedia. Silicon. www.newworldencyclopedia.org.

[141] D. Julthongpiput, M. LeMieux, and V. V. Tsukruk. Micromechanical properties of glassy and rubbery polymer brush layers as probed by atomic force micrscopy. *Polymer*, 44:4557–4562, 2003.

[142] M. Lemieux, S. Minko, D. Usov, and V. V. M. Stamm, Tsukruk. Direct measurement of thermoelastic properties of glassy and rubbery polymer brush nanolayers grown by grafting from approach. *Langmuir*, 19:6126–6134, 2003.

[143] V. Y. Grinberg, A. S. Dubovik, D. V. Kuznetsov, N. V. Grinberg, A. Y. Grosberg, and T. Tanaka. Studies of the thermal volume transition of poly(N-isopropylacrylamide) hydrogels by high-sensitivity differential scanning microcalorimetry. 2. thermodynamic functions. *Macromolecules*, 33:8685–8692, 2000.

[144] S. Ohki and K. Arnold. A mechanism for ion-induced lipid vesicle fusion. *Colloid and Surfaces B: Biointerfaces*, 18:83–97, 2000.

[145] S. Ohki and K. Arnold. Experimental evidence to support a theory of lipid membrane fusion. *Colloid and Surfaces B: Biointerfaces*, 63:276–281, 2008.

[146] T. Lian and R. J. Y. Ho. Trends and developments in liposome drug delivery systems. *Journal of Pharmaceutical Science*, 90:667–680, 2001.

[147] A. Mecke, I.J. Majoros, A.K. Patri, J.R. Baker, M.M.B. Holl, and B.G. Orr. Lipid bilayer disruption by polycationic polymers: The roles of size and chemical functional group. *Langmuir*, 23:10348–10354, 2005.

[148] T. Buranda, J. Huang, G. V. Ramarao, L. K. Ista, R. S. Larson, T. L. Ward, L. A. Sklar, and G. P. Lopez. Biomimetic molecular assemblies on glass and mesoporous silica microbeads for biotechnology. *Langmuir*, 19:1654–1663, 2003.

[149] T. M. S. Chang. *Artificial Cells*. Charles C. Thomas, 1972.

[150] M.M.G. Krishna, A. Srivastava, and N. Periasamy. Rotational dynamics of surface probes in lipid vesicles. *Biophysical Chemistry*, 90:123–133, 2001.

[151] S. A. Yamanaka, D. H. Charych, D. A. Loy, and D. Y. Sasaki. Solid phase immobilization of optically responsive liposomes in sol-gel materials for chemical and biological sensing. *Langmuir*, 13:5049–5053, 1997.

[152] D. G. Hunter and B. J. Frisken. Effect of extrusion pressure and lipid properties on the size and polydispersity of lipid vesicles. *Biophysical Journal*, 76:2996–3002, 1998.

[153] M. Anderson and A. Omri. The effect of different lipid components on the in vitro stability of release kinetics of liposome formulations. *Drug Delivery*, 11:33–39, 2004.

[154] H. C. Shum, D. Lee, Kodger T. Yoon, I., and D. A. Weitz. Double emulsion templated monodisperse phospholipid vesicles. *Langmuir*, 24:7651–7653, 2008.

[155] S. Sugiura, T. Kuroiwa, T. Kagota, M. Nakajima, S. Sato, S. Mukataka, P. Walde, and S. Ichikawa. Novel method for obtaining homogeneous giant vesicles from a monodisperse water-in-oil emulsion prepared with a microfluidic device. *Langmuir*, 24:4581–4588, 2008.

[156] R. Watwe and J. Bellare. Manufacture of liposomes: A review. *Current Science*, 68:715–724, 1995.

[157] G. V. RamaRao, G. P. Lopez, J. Bravo, H. Pham, A. K. Datye, H. Xu, and T. L. Ward. Monodisperse mesoporous silica microspheres formed by evaporation-induced self-assembly of surfactant templates in aerosols. *Advanced Materials*, 14:1301–1304, 2003.

[158] J. J. Pignatello and B. Xing. Mechanisms of slow sorption of organic chemicals to natural particles. *Environmental Science and Technology*, 30:1–11, 1996.

[159] J. Karger and D. Freude. Mass transfer in micro- and mesoporous materials. *Chemical Engineering Technologies*, 25:769–778, 2002. REVIEW.

[160] E. Gedat, A. Schreiber, G.H. Findenegg, I. Shenderovich, H.-H. Limbach, and G. Buntkosky. Stray field gradient NMR reveals effects of hydrogen bonding on diffusion coefficients of pyridine in mesoporous silica. *Magnetic Resonance in Chemistry*, 39:S149–S157, 2001.

[161] J.M. Gurgel, L.S. Andrade Filho, P.H Greneir, and F. Meunier. Thermal diffusivity and adsorption kinetics of silica-gel/water. *Adsorption*, 7:211–219, 2001.

[162] W. E. Huang, C. C. Smith, D. N. Lerner, S. F. Thornton, and A. Oram. Physical modelling of solute transport in porous media: evaluation of an imaging technique using UV excited fluorescent dye. *Water Research*, 36:1843–1853, 2002.

[163] K. Nakatani and T. Sekine. Direct analysis of intraparticle mass transfer in silica gel using single-microparticle injection and microabsorption methods. *Langmuir*, 16:9256–9260, 2000.

[164] N. E. Fernandes and G. R. Gavalas. Molecular dynamics simulations of diffusion in mesoporous glass. *Industrail Engineering Chemistry Res.*, 38:723–730, 1999.

[165] J. Farrell, D. Grassian, and M. Jones. Investigation of mechanisms contributing to slow desorption of hydrophobic organic compounds from mineral solids. *Environmental Science and Technology*, 33:1237–1243, 1999.

[166] R. Netrabukkana, K. Lourvanij, and G. L. Rorrer. Diffusion of glucose and glucitol in microporous and mesoporous silicate/aluminosilicate catalysts. *Industrial Engineering Chemical Res.*, 35:458–464, 1996.

[167] G. Drazer, R. Chertco, L. Bruno, and M. Rosen. Concentration dependence of diffusion-adsorption rate in activated carbon. *Chemical Engineering Science*, 54:4285–4291, 1999.

[168] G. Drazer, R. Chertco, L. Bruno, M. Rosen, and J.P. Hulin. Tracer dispersion in packings of porous activated carbon grains. *Chemical Engineering Science*, 54:4137–4144, 1999.

[169] R. I. Nooney, M. Kalyanaraman, G. Kennedy, and E. J. Maginn. Heavy metal remediation using functionalized mesoporous silicas with controlled macrostructure. *Langmuir*, 17:528–533, 2001.

[170] Q Fu, G.V.R. Rao, L.K. Ista, Y. Wu, B.P. Andrzejewski, L.A. Sklar, T.L. Ward, and G.P. Lopez. Control of molecular transport through stimuli-responsive ordered mesoporous materials. *Advanced Materials*, 15:1262–+, 2003.

[171] E. Tziampazis and A. Sambanis. Tissue engineering of a bioartificial pancreas: Modeling the cell environment and device function. *Biotechnological Progress*, 11:115–126, 1995.

[172] J. J. Cras, C. A. Rowe-Taitt, D. A. Nivens, and F. S. Ligler. Comparison of chemical cleaning methods of glass in preparation for silanization. *Biosensors & Bioelectronics*, 14:683–688, 1999.

[173] J. Crank. *The Mathematics of Diffusion 2nd ed.* Oxford Science Publications, 1975.